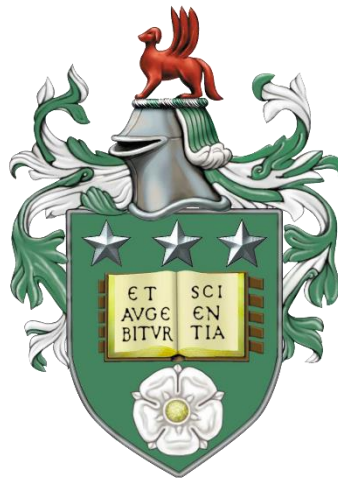# Quantum Dot Redox Sensors: Understanding Excited State Dynamics

Andrew James Harvie

Submitted in accordance with the requirements for the degree of

Doctor of Philosophy

University of Leeds

School of Physics and Astronomy

April 2018

The candidate confirms that the work submitted is his own, except where work which has formed part of jointly authored publications has been included. The contribution of the candidate and the other authors to this work has been explicitly indicated below. The candidate confirms that appropriate credit has been given within the thesis where reference has been made to the work of others.

The work discussed in chapters 3 & 4 of this thesis has appeared in publication as follows:

Harvie, A. J.; Booth, M.; Chantry, R. L.; Hondow, N.; Kepaptsoglou, D. M.; Ramasse, Q. M.; Evans, S. D.; Critchley, K. Observation of compositional domains within individual copper indium sulfide quantum dots. *Nanoscale* **2016**, *8*, 16157-16161.

AH was responsible for synthesis of particles, XPS measurements, optical spectroscopy, data analysis and writing the manuscript, and assisted with XRD, TEM and EELS experiments. The contribution of the other authors involved acquisition of TEM, XRD and EELS data, data analysis, and assisting with manuscript preparation.

Harvie, A. J.; Smith, C. T.; Ahumada-Lazo, R.; Jeuken, L. J. C.; Califano, M.; Bon, R. S.; Hardman, S. J. O.; Binks, D. J.; Critchley, K. Ultrafast Trap-State Mediated Electron Transfer for Quantum Dot Redox Sensing. *The Journal of Physical Chemistry C* **2018**. *122*, 18, 10173-10180.

AH was responsible for synthesis of QDs and organic compounds, chemical characterisation, production of conjugates, steady state PL and UV-vis spectroscopy, PL lifetime spectroscopy, TEM, cyclic voltammetry, data analysis and writing the manuscript. The contribution of the other authors involved further steady state PL and PL lifetime spectroscopy, TA spectroscopy, calculation of electron transfer timescales, further data analysis and assisting with writing the manuscript.

Cell squeezing experiments reported in chapter 5 of the thesis were led by Abiral Tamang, using chips designed and fabricated by Fern Armistead.

Other publications co-authored during the course of this studentship include:

Virzbickas, K.; Rimkute, L.; Harvie, A. J.; Critchley, K., Surfactant-dependent photoluminescence of CdTe/CdS nanocrystals. *J Exp Nanosci* **2017**, *12*, 94-103.

AH assisted with interpretation of data and manuscript preparation.

Striolo, A.; Kim, J.; Murphy, C.; Liz-Marzán, L.; Lahann, J.; Reguera, J.; Zhou, Y.; Brust, M.; Thill, A.; Scarabelli, L., Particles at Interfaces: General Discussion. *Faraday Discussions* **2016**, *191*, 407-434.

AH participated in discussions.

Acknowledgements

Firstly I would like to thank my supervisors Kevin Critchley, Robin Bon and Lars Jeuken for their constant support, advice, knowledge and enthusiasm. I have genuinely enjoyed working with them over the course of this PhD and feel they have turned me from "boy with degree" to "Scientist".

Other big thanks go to the High-content Biology team at AstraZeneca in Cambridge for providing expertise, funding and access to their excellent facilities. Similarly, the scientists at SuperSTEM, particularly Demi Kepaptsoglou, Quentin Ramasse and Ruth Chantry, were key in the work on $CuInS_2$ QDs, which turned out wonderfully. Nicole Hondow deserves huge thanks for her constant enthusiasm and helpfulness with all things electron. My gratitude also goes to Masayoshi Tanaka, Taisuke Minamide, Mina Okochi and all other members of the Okochi group for their warm welcome, hospitality and hard work during my time with them at the Tokyo Institute of Technology, whose funding I also gratefully acknowledge. David Binks, Charlie Smith and Ruben Ahumada-Lazo deserve enormous credit for letting us use their fantastic photonics labs, as well as their expertise in excited state dynamics. Also, Marco Califano has put a lot of time and effort into performing calculations for electron transfer timescales.

Abiral Tamang is inheriting a lot of my quantum dot mess, and has helped a huge amount with the cell squeezing work. Fern Armistead deserves credit for making the devices and providing her time, expertise and skill. Julia Gala provided her unmatched microscopy skills alongside indefatigable cheerfulness. I will never forget the chicken song.

Aside from academic contributions, I'd like to thank the rest of the MNP group for their constant banter, encouragement, company and friendship over the last four years. We are lucky to work in a research group where everyone likes each other and understands the collaborative spirit. I'll mention Victoria Mico by name because she'd be annoyed if I didn't (also we're mates). I also feel very privileged to have such a strong group of friends from the Boro, who now live all over the UK and beyond. Considering we're all idiots it's wonderful that we're also still top mushes.

My final thanks go to my family who are always present, supportive, encouraging and generous. Special thoughts are with the Duns clan after the events of this this year. Lastly, Jessica has been the best, and has kept me happy, warm, and full of sausages. May there be many, many more soft critters in our future.

Abstract

Semiconductor quantum dots (QDs) are a quintessential example of nanotechnology; their useful optoelectronic properties (including bright photoluminescence) that distinguish them from bulk semiconductors arise primarily due to their nanoscopic size, and the discrete, quantum mechanical nature of matter.

The "redox environment", defined as the general tendency of molecules to be reduced or oxidised in a given microenvironment, is one of the central concepts of the field of redox biology. Current methods of measuring the redox environment within living cells are unsatisfactory. To address this, a number QD-based redox sensors have been developed, however, there are still open questions about the physics of such sensors, particularly with respect to their excited-state electron dynamics.

This thesis details the excited state dynamics of QD-based redox sensors, as well as their application to biology. Chapter 1 contains an overview of the photophysics of such QD biosensors, as well as a review of the relevant literature.

Chapter 3 details electron microscopy-based studies of the internal structure of $CuInS_2$ QDs, aimed at understanding their defect-related excited state dynamics, with a view to their application as less toxic biosensors. It was concluded that the emissive transition in $CuInS_2$ QDs is associated to an electronic state that arises due to large, polydisperse defect clusters that exist within the $CuInS_2$ lattice.

Chapter 4 details ultrafast spectroscopic studies of a QD redox sensor that consists of a CdTe/CdS core/shell QD coupled with a quinone-derived electron acceptor (Q2NS), which acts as a redox-switching, photoluminescence-quenching electron acceptor. It was found that the comparatively efficient switchable quenching is due to an ultrafast trapping scheme, involving an electron energy state associated with a surface-based lattice defect. Application of the redox sensors to biological cells was then studied, particularly with respect to the mechanism by which cells internalise the QDs, and the resulting QD microenvironment. It arises that endocytosis and subsequent compartmentalisation of QDs by cells presents a significant challenge to the application of QDs as intracellular biosensors.

Table of Contents

List of Figures

List of Abbreviations

QD – Quantum dot

ROS – Reactive oxygen species

ADHD – Attention deficit hyperactivity disorder

PL – Photoluminescent/photoluminescence

PLQY – Photoluminescent quantum yield

NADH/NADPH – Nicotinamide adenine dinucleotide/Nicotinamide adenine dinucleotide phosphate

CoQ_{10} – Coenzyme Q_{10}/Ubiquinone

CB – Conduction band

VB – Valence band

CBM – Conduction band minimum

VBM – Valence band maximum

XRD – X-ray diffraction

ICDD – International Centre for Diffraction Data

XPS – X-ray photoelectron spectroscopy

UV-Vis-NIR – Ultra-violet-Visible-Near Infra-red

TA – Transient absorption

TCSPC – Time-correlated single photon counting

TEM – Transmission electron microscopy

CCD – Charge-coupled device

STEM – Scanning transmission electron microscopy

HAADF – High-angle annular dark field

EELS – Electron energy loss spectroscopy

LC-MS – Liquid column chromatography-mass spectrometry

NMR – Nuclear magnetic resonance

HPLC – High-performance liquid chromatography

CV – Cyclic voltammetry

SAM – Self-assembled monolayer

FRET – Förster resonance energy transfer

CT – Charge transfer

Alc-DH – Alcohol dehydrogenase

MBP – Maltose binding protein

TGA – Thioglycolic acid

DDT – Dodecanethiol

ODE – Octadecene

MeOH – Methanol

DMSO – Dimethyl sulfoxide

DMF - Dimethylformamide

DAP – donor-acceptor pair

HIV – Human immunodeficiency virus

EEA-1 – Early endosome antigen 1

PFA – Paraformaldehyde

DPBS – Dulbecco's phosphate-buffered saline

CPP – Cell-penetrating peptide

PEI - Polyethylenimine

1   Introduction

1.1   Motivation – Redox in disease

Redox reactions are those which involve transfer of electrons from an electron donor (a reducing agent, which is oxidised) to an acceptor (the oxidising agent, which is reduced). A "half-reaction" is the term given to oxidation or reduction alone – one cannot happen without the other. Redox reactions are present almost everywhere, from combustion of organic material (where oxygen is reduced by carbon) to the rusting of iron (where iron is oxidised). For this process, the half-reactions can be written:

$$Fe \rightarrow Fe^{2+} + 2e^-$$

$$\frac{1}{2}O_2 + H_2O + 2e^- \rightarrow 2OH^- \qquad\qquad (1)$$
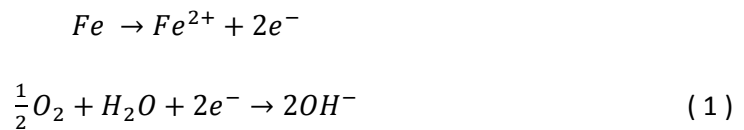
Given their ubiquity, it is not a surprise that redox reactions are also critically important in biology. The classical example of redox within biology is in aerobic respiration, where glucose is oxidised in the presence of oxygen to form carbon dioxide and water, however redox reactions are present in almost all cellular processes, from signalling during the cell cycle to anaerobic respiration.[1]

There is a large number of redox "pairs" involved in various biological processes, including the reduced and oxidised forms of nicotinamide adenine dinucleotide (NADH/NAD+), ubiquinone/ubiquinol, and nicotinamide adenine dinucleotide phosphate (NADPH/NADP+) among many others; these are biomolecules that can exist in either an oxidised or a reduced state, and tend to be cofactors in enzymatic redox reactions.[2] These pairs are often reversibly oxidised and reduced between each state, and usually act to transport electrons within biochemical processes. When discussing redox within the context of biology it is often helpful to consider the concept of the "redox environment" of the cell; this can be considered the concentration balance between the oxidised and reduced forms of these redox pairs. Redox balance was first implicated in the cell cycle in the early 1930s,[3] and it is now understood that it is involved in, or can be a reporter on a number of disease states, particularly cancer. Increasing understanding of the notion of the cellular redox environment, and its consequences in redox control and redox signalling, has led to the field of redox biology, which has relevance across the breadth of biological study.
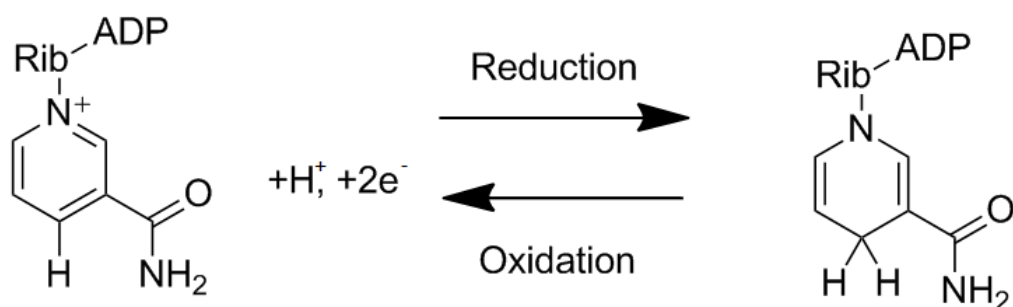
Figure 1. Redox behaviour of nicotinamide adenine dinucleotide (NAD). NAD+ (left) is reversibly reduced to form NADH (right) involving addition of one proton and two electrons. The opposite reaction is termed oxidation.

In the understanding of disease, the redox environment is often an important factor. Oxidative stress is an increase in the presence of reactive oxygen species (ROSs), or a decrease in the effectiveness in antioxidants used to cope with them, and is implicated in the development of a broad gamut of diseases,[4] including cancer,[5, 6] atherosclerosis, neurodegenerative diseases such as Parkinson's disease and Alzheimer's disease,[7, 8] developmental disorders such as Asperger syndrome,[9] and mental disorders such as ADHD.[10, 11]

The Warburg effect is the observation that cancer cells tend to produce large amounts of lactate through glycolysis, even with an ample supply of oxygen, sometimes termed "aerobic glycolysis". Glycolysis is an alternative metabolic pathway used for energy production which does not require oxygen. In healthy cells, glycolysis is usually minimised when there is abundant oxygen, in favour of aerobic respiration. The cause of the Warburg effect was initially assigned to dysfunction of mitochondria in diseased cells, however current hypotheses differ.[12] In any case, the result of the Warburg effect in combination with other factors means that cancer triggers dysregulation in the cellular redox environment.[13] It has also been shown that an increase in glycolysis is necessary for the proliferation of cancer.[14] Glycolytic inhibitors, which are drugs or drug candidates that inhibit glycolysis, are therefore under investigation as possible future cancer treatments; their discovery might depend on assessing their effects on the redox environment as it is dysregulated by the Warburg effect.

For the reasons outlined above, for the study of disease it is useful to have techniques for measurement of the redox environment within model cell lines. In the modern lab

fluorescence techniques are ubiquitous, and so this provides an ideal platform for the development of new redox sensing technologies. An ideal redox sensor will allow long term, time-resolved measurement of the redox potential, with minimal setup and high accuracy, and preferably will not affect the chemistry of the cell itself. There are a number of commercially available redox probes based on fluorescence of transfected small molecules (including Thermo Scientific CellROX™ range), or genetically encoded fluorescent proteins (Premo™). In either case, the reliance on photo-bleachable fluorophores severely limits the maximum timescale of any single experiment. For the case of the genetically encoded redox probes, there are also concerns of reproducibility between cell lines, as well as the long and complex experimental setup. The separate technique of measurement of NADH fluorescence allows quantification of the amount of NADH within a cell, however it is difficult to derive information about general redox balance from this.

New sensing strategies must therefore be developed to avoid the limitations of current redox probes. The potential of photoluminescent quantum dots in bioimaging and biosensing has been recognised since the late 1990s,[15-17] and therefore it is no surprise that their application as potential redox probes is now widely researched and discussed in the literature; the work discussed in this thesis involves design and optimisation of such QD-based redox sensors.

1.2   Quantum dots

Semiconductor quantum dots (QDs) are nanocrystalline semiconductors with diameter close to or below the exciton Bohr radius (typically <10 nm). Amongst their other interesting properties, and depending on the composition of the QD, this leads to a tuneable photoluminescence (PL), similar to fluorescence observed in molecular fluorophores. However, the useful physical properties of QDs are not limited to photoluminescence. The broad optical excitation spectrum of QDs makes them excellent candidates for absorbing material in photovoltaic applications,[18-20] and their robust and controllable emission has seen them applied in fields ranging from bioimaging[21] to display technology.[22] Recently, high-spec televisions with displays based on quantum dot technology have become available to consumers.[23, 24] For information technology, semiconductor QDs are one of the possible materials being explored for potential application to store qubits, the unit of quantum computing.[25]

In bioimaging and biosensing, quantum dots are rapidly developing from a nascent technology into a flexible platform for primarily fluorimetric analysis of biological systems.

Compared to traditional molecular fluorophores, quantum dots have a number of advantages: they exhibit high photoluminescent quantum yield (PLQY), are resistant to photobleaching, and provide a surface which allows for facile and possibly multiplexed functionalisation. They can exhibit sharp, accurately tuneable emission that can span from the UV to near infra-red. Their large Stokes shift, coupled with broad absorption also allow for single-excitation multiplexing of quantum dots for use in complex imaging and assaying techniques.

It is due to these useful properties that QDs are increasingly being applied in bioimaging and biosensing, including sensing of redox environment within cells. [21, 26-29] This thesis focusses on the development and understanding of such redox sensors, and their application to biology.

1.3   Photophysics of quantum dot sensors

This section discusses the properties of colloidal semiconductor quantum dots, and how these properties can be exploited to create redox-sensitive photoluminescent probes.

1.3.1   Introduction to semiconductors

Every solid material contains a large number of electrons. For bulk crystalline solids, we can consider a lattice made up of an arbitrarily large number of atoms, where the electron orbitals associated with these constituent atoms have broadened into continuous energy bands. Depending on the interaction of the wavelike electrons with the atomic cores of the crystal, there will be "forbidden" regions between bands in momentum space where there are no available states. It is the scheme by which electrons are distributed between bands, as well as the magnitude of the gaps between bands that determines whether a given crystalline material is classified as an insulator, a metal, or a semiconductor.

Electrons, as fermions, obey the Pauli Exclusion Principle, which states that no two fermions can occupy the same quantum state. As such, a collection of fermions at temperature T will have energies described by the Fermi-Dirac distribution:

$$f(E) = \frac{1}{e^{\frac{E-E_f}{k_B T}} + 1} \qquad (2)$$

Here, $f(E)$ is the probability that an electron will have energy E, and k_B is the Boltzmann constant. E_F is known as the Fermi level, and describes the limiting energy for fermions at absolute zero. At finite temperatures, the Fermi level describes the energy for which the occupation probability $f(E_F) = 0.5$.

For a metal at absolute zero, electrons fill states up to the Fermi energy, which exists outside of a forbidden region. The consequence of this is that the material is capable of conducting, as there is no lower bound on the energy required to reach the next available state; even the smallest "ripple" on the surface of the "Fermi sea" results in conduction.
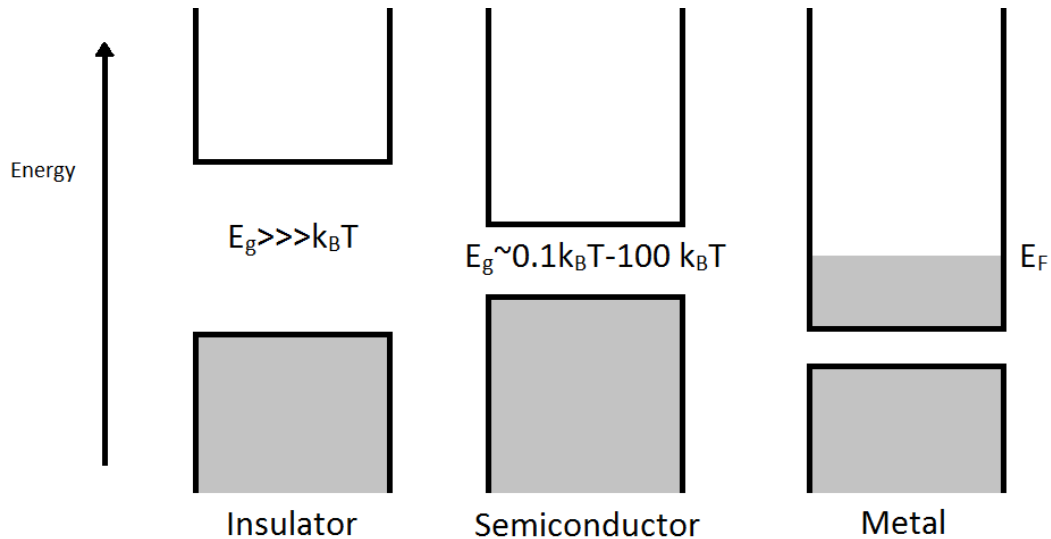
Figure 2. Schematic of filling of energy bands at 0 K for typical insulator, semiconductor and metal. Grey areas represent filled states. The "band gap" energy E_g is small enough in semiconductors such that a proportion of electrons can inhabit the conduction band at finite temperatures.

For the case of both insulators and semiconductors at 0 K, an energy gap of forbidden states exists between a band that is completely filled with non-conducting electrons (known as the valence band) and another, higher energy band which will be unfilled at 0 K. For the case of insulators, the Fermi energy lies within this gap, which is wide enough that no electrons can reach the next energy band. In a semiconductor, this "band gap" is narrow enough that at finite temperatures, equation 2 would predict that carriers can be thermally excited to the higher energy band, which is unfilled and therefore capable of conduction. This energy band is known as the conduction band for the semiconductor. In an intrinsic (pure) semiconductor, the Fermi level lies exactly halfway between the conduction and valence bands.

The band gap of any given semiconductor can be characterised as being one of two types: direct or indirect. The band gap is said to be direct if the minimum energy state of the conduction band (conduction band minimum, or CBM) and the maximum energy state in the valence band (VBM) lie at the same crystal momentum in the energy-momentum relation

(or dispersion relation). This means that any transition that happens between these two energy states is achieved without imparting any momentum to the crystal, and so can involve simple absorption or emission of a photon. In an indirect band gap semiconductor, the VBM and CBM lie at different momentum states, and so any transition that occurs must also impart momentum to the lattice, which happens usually through emission or absorption of a phonon, the quant of collective vibration of the crystal lattice.
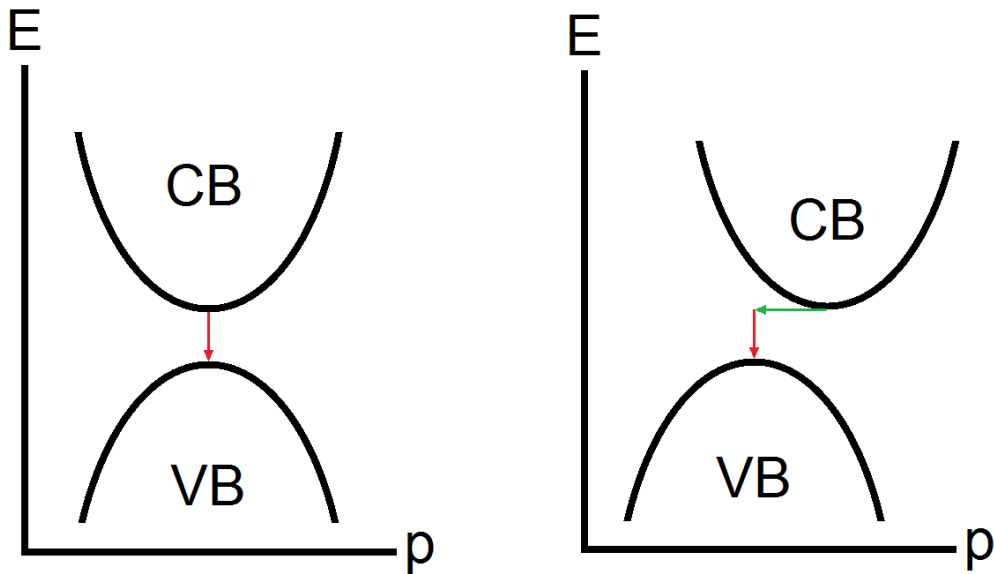
Figure 3. Schematic diagram of energy-momentum relations in direct (left) and indirect (right) band gap semiconductors. With a direct band gap, minimum energy transitions can occur vertically in E-p space, and do not impart momentum to the crystal lattice. In the indirect case, the minimum energy transition occurs via emission of a phonon (green) which provides the momentum necessary to avoid violation of conservation of momentum.

The electronic properties of a semiconductor can be modified through "doping" which involves addition of impurities of a different valence, which act as electron donors or electron acceptors within the lattice. This has a drastic effect on the carrier concentration and therefore the conductivity of the semiconductor. For example, doping silicon with boron (an acceptor) with a B:Si ratio of $1:10^5$ results in an increase in conductivity of the order of 10^3.[30] Such doping is known as "p-type" doping. In p-type doping, added electron acceptors leave empty orbitals in the valence band. This empty orbital is known as a "hole" and can be treated as a pseudoparticle with both effective mass and a charge $+e$, where $-e$ is the electron charge. Holes are charge carriers, and therefore it is the motion of these holes throughout the valence band that results in the increased conductivity of p-type

semiconductors. An n-type semiconductor works on the opposite principle; a semiconductor doped with electron donors provides charge carriers in the form of electrons to the conduction band, which carry charge as they would in a metal (albeit at a much lower concentration). This is possible as all valence band states are already filled by electrons, before considering those provided by the dopant. Doped semiconductors of both types will exhibit conductivity at 0 K for the reasons outlined above.

A bulk, stoichiometric semiconductor that is not doped is known as an intrinsic semiconductor. A deficit semiconductor is the name given to a non-stoichiometric compound semiconductor, where the excess of one constituent acts as a dopant impurity.

An electron excited to the conduction band via thermal excitation or otherwise results in the creation of a hole in the valence band. The opposite charges of the electron and hole will mean they will electrostatically attract, and unless there is a large excess in kinetic energy after excitation from a lower energy state, they will be bound to one another. This electron-hole pair is collectively termed an "exciton" and propagates with a reduced mass μ, where:

$$\frac{1}{\mu} = \frac{1}{m_e^*} + \frac{1}{m_h^*} \tag{3}$$

The masses m_e^* and m_h^* are the effective masses of the electron and hole, respectively.

1.3.2   Effects of confinement in 0-D semiconductors

When considering size dependent effects for excitons within semiconductors, it is useful to define a characteristic radius for the exciton. For the equilibrium separation of electron and hole, the following expression can be written in terms of the kinetic energy of the mutual motion and the electric potential energy:

$$\frac{1}{2}\mu v^2 = \frac{1}{4\pi\varepsilon_r\varepsilon_0}\frac{e^2}{r}. \tag{4}$$

Here, μ is the reduced mass, r is the separation, and v is the relative angular velocity of the electron-hole pair. The parameters ε_r and ε_0 are the relative permittivity of the material, and the permittivity of free space respectively.

The Bohr model describes a quantised angular momentum $L = \mu v r$ with minimum value $\hbar$. It is therefore possible to define a separation r = a_0* for this value, giving:

$$a_0^* = \frac{4\pi\varepsilon_r\varepsilon_0\hbar^2}{\mu e^2} = \varepsilon_r\frac{m_e}{\mu}a_b \qquad\qquad (5)$$

Here, a_b is the hydrogen Bohr radius, and m_e is the mass of a free electron. The length a_0^* is known as the characteristic Bohr radius for the semiconductor.

As the size of a semiconductor object is decreased towards and below the characteristic Bohr radius, any generated exciton becomes confined. One consequence of this is that the continuous energy bands described in the previous section separate into states analogous to a simple atom. The confinement energy associated with these states also results in an increase of the effective band gap of the semiconductor; the band gap is therefore heavily size dependent below the Bohr radius. Producing a useful theoretical model that describes the behaviour of confined excitons within quantum dots is difficult; for typical QD materials such as CdTe, CdSe and $CuInS_2$ the number of atoms at the size where confinement becomes important can be of the order of 10^3-10^5, and the proportion of constituent atoms that makes up the surface of the particle can become significant (up to 60%).[31] Aside from the surface effects that preclude treating the QD as a continuous material, the small number of atoms means that even in perfectly stoichiometric ensembles of QDs, individual particles are unlikely to be perfectly stoichiometric, manifesting as an intrinsic doping of the semiconductor (a deficit semiconductor). Computational approaches to simulate electronic behaviour within QDs are common. Traditionally, density functional theory (DFT) approaches have been applied, however they are often inaccurate in predicting band gap values, often requiring large ad-hoc empirical corrections.[32] More recently, developments in the application of the atomistic semiempirical pseudopotential method has allowed accurate in-silico interrogation of more complex QD systems, including simulation of Auger and ultrafast trapping processes.[33-35] For a general description of excitonic confinement within QDs, it is nevertheless instructive to consider a simplified "particle in a box" treatment, which is described here.

As before, an optically generated electron-hole pair within a semiconductor can be considered as a single "exciton" with effective mass given by equation 3. To approximate a quantum dot, we can define a spherical potential of the form

$$V(r,\varphi,\theta) = \begin{cases} 0, & r < d \\ \infty, & r \geq d \end{cases} \qquad\qquad (6)$$

Here, r, ɸ, and θ are the radial distance, azimuthal angle and polar angle respectively, and d is the radius of the dot. This potential is the spherical equivalent of the famous "particle in a

box" where the infinite potential outside the prescribed radius d precludes any nonzero value of the exciton's wavefunction, and is the simplest approximation available for a spherical system. The time-independent Schrodinger equation for this system is written:

$$\left[\frac{-\hbar^2}{2\mu}\left(\frac{\partial^2}{\partial r^2} + \frac{2}{r}\frac{\partial}{\partial r} - \frac{L^2}{\hbar^2 r^2}\right) + V(r)\right]\psi(r,\varphi,\theta) = E\psi(r,\varphi,\theta) \qquad (7)$$

We can use the time-independent Schrodinger equation as the Hamiltonian is time-independent. In this expression, $\hbar$ is the reduced Planck constant, and L^2 is the square of the angular momentum operator, with eigenvalues as follows:

$$L^2\psi(r,\varphi,\theta) = R(r)L^2A(\varphi,\theta) = R(r)l(l+1)^2\hbar^2A(\varphi,\theta) \qquad (8)$$

Here the wavefunction $\psi(r,\varphi,\theta)$ has been decomposed into radial and angular parts $R(r)$ and $A(\varphi,\theta)$ respectively; the radial wavefunction $R(r)$ commutes with L^2. The integer l is a quantum number associated with angular momentum.

Within the QD, $0 \leq r < d$, and $V(r) = 0$. Introducing the new quantum number n, the Schrodinger equation can therefore be written:

$$\frac{d^2R_{n,l}}{dr^2} + \frac{2}{r}\frac{dR_{n,l}}{dr} + \left(k^2 - \frac{l(l+1)}{r^2}\right)R_{n,l} = 0, \qquad (9)$$

where we have defined the variable k, so that

$$k^2 = \frac{2\mu E}{\hbar^2}. \qquad (10)$$

We can further define the scaled variable $a = kr$, which allows us to simplify and write the radial Helmholtz equation:

$$a^2\frac{d^2R_{n,l}}{da^2} + 2a\frac{dR_{n,l}}{da} + [a^2 - l(l+1)]R_{n,l} = 0. \qquad (11)$$

The linearly independent solutions of this expression are known as the spherical Bessel functions $j_l(a)$ and $y_l(a)$. The functions $y_l(a)$ are unphysical as they are not square integrable at $r = 0$, instead tending toward negative infinity. However, the functions $j_l(a)$ are well behaved, and are written:

$$j_l(a) = a^l\left(\frac{-1}{a}\frac{d}{da}\right)^l\left(\frac{\sin a}{a}\right) \qquad (12)$$

As the potential is infinite for radii $r \geq d$, the value of the wavefunction must disappear to zero at the boundary. To achieve this, we choose a value of k such that $a = kd$ corresponds

to a zero of $j_l(a)$. We can write the nth zero of $j_l(a)$ as $\alpha_{n,l}$, and therefore state that for positive integer values of n:

$$kd = \sqrt{\frac{2\mu E_{n,l}}{\hbar^2}}\, d = \alpha_{n,l} \tag{13}$$

The value of zeros $\alpha_{n,l}$ is an increasing function for both quantum numbers n and l. Rearranging gives the following expression for the energy levels of a particle trapped in an infinite spherical potential:

$$E_{n,l} = \frac{\alpha_{n,l}^2 \hbar^2}{2\mu d^2}. \tag{14}$$

For our quantum dot, this is the energy associated with confinement of the exciton within the interior of the dot. The lowest energy state is for quantum numbers $n = 1$, $l = 0$, with value $\alpha_{1,0} = \pi$ and corresponds to the "1s" state of the analogous atom for both electron and hole. The total energy required to obtain this first excited state in a quantum dot is the band gap energy of the quantum dot, and is given by the following expression:

$$E_{g,QD} = E_{g,bulk} + \frac{\pi^2 \hbar^2}{2\mu d^2} - \frac{1.786 e^2}{\varepsilon d}. \tag{15}$$

The final term is included as a consequence of the electrostatic attraction between the oppositely charged electron and hole.[36, 37] As it is inversely proportional to the particle radius d, it will only have large effect with respect to the confinement term for larger quantum dots, where it will serve to decrease the band gap. The important result is the inverse square size dependence of the confinement term, which predicts and explains the strong size dependence of quantum dot luminescence for small sizes.

1.3.3   Photon Absorption by Quantum Dots

In the previous section an expression was derived for the minimum energy required to promote an electron to from the valence band into the conduction band, achieving an exciton of the lowest energy state. Quantum dots are typically much smaller than the wavelength of light, so this can often reliably achieved by absorption of a photon with energy greater than the band gap: $E = \hbar\omega \geq E_{g,QD}$. In a general case, an electron will be excited from the ground state $|i\rangle$ into an excited state $|f\rangle$ by a photon of energy $E_{i,f} = \hbar\omega_{i,f}$ where $E_{i,f}$ is the difference in energy between these states.

The density of states for a material expresses the number of states per energy interval available for occupation at each energy level. Quantum dots can neither be considered a

perfect 0D nor a bulk 3D material. However, it is possible to accurately express the density of states for a QD in the form:[38]

$$N_{0D}(E) = \frac{1}{V_{QD}}\Sigma_{i,m}(2m+1)\delta(E-E_i) \qquad (16)$$

In this expression, E_i are the energy levels with degeneracy m, and V_{QD} is the geometric volume of the QD. For a real system, this volume can be obtained by averaging over a polydisperse sample. From this expression, Sun and Goldys derive the following expression of the linear optical absorption coefficient of a single quantum dot subject to incident light of angular frequency ω, which is necessarily proportional to the density of states:

$$\alpha_{QD}(E = \hbar\omega) = \frac{\pi e^2 E_p a_p}{2m_e c n_r \varepsilon_0 \omega}\frac{1}{V_{QD}}\sum_{i,m}(2m+1)\delta(\hbar\omega - E_i)$$

$$= \frac{A}{\omega V_{QD}}\Sigma_{i,m}(2m+1)\delta(\hbar\omega - E_i) \qquad (17)$$

In this expression, e is the unitary charge, a_p is the average over polarisation directions for the incident light (2/3 for unpolarised light), and n_r is the frequency dependent refractive index for the QD material. This model assumes the infinite spherical potential approximation for the QDs used in the previous section. For a sample of QDs, the size polydispersity must be taken into account; the variation in size results in a distribution of quantised energies, with widths ΔE_{im}. This can be achieved by replacing the delta function by a Gaussian distribution of energies:

$$\alpha_{QD}(E = \hbar\omega) = \frac{A}{\omega V_{QD}}\Sigma_{i,m}\frac{(2m+1)}{\sqrt{2\pi}E\Delta E_{im}}\exp\left(-\frac{(\hbar\omega - E_{im})^2}{2\Delta E_{im}^2}\right). \qquad (18)$$

For experimental measurement of a sample of colloidal QDs in solution, the molar extinction coefficient is a more useful quantity. It is defined and expressed as a function of photon energy E as follows:

$$\epsilon(E) = \frac{N_A V_{QD}\alpha_{QD}(E)}{\ln(10)}. \qquad (19)$$

In the above expression, the constant N_A is Avogadro's number.

The above treatment considers absorbance events that result in the promotion of an electron from the valence band to the conduction band. At low excitation energies, QD states are more discrete and "atom-like", however at increased energies the QD states become more "band-like" as discrete states exist closer together. This is evident in a typical

absorbance spectrum for a sample of quantum dots, an example of which is given in figure 4. At longer wavelengths, which correspond with photon energies insufficient to achieve photoexcitation of the quantum dot, absorbance is zero. As the wavelength decreases (to higher photon energies) there exists a peak which corresponds to the "1s" excitation. The width of this peak depends on the polydispersity or size variation present in the QD sample. At further decreased wavelengths the absorbance continues to increase with the number of accessible electronic states. Spectral features associated with particular electronic transitions become more difficult to resolve at increase excitation energies due to their width and energetic proximity. Some QDs made from materials such as $CuInS_2$ display characteristically broad absorption and emission features, which is often characteristic of a high size polydispersity or a defect-rich crystal structure.[39, 40]
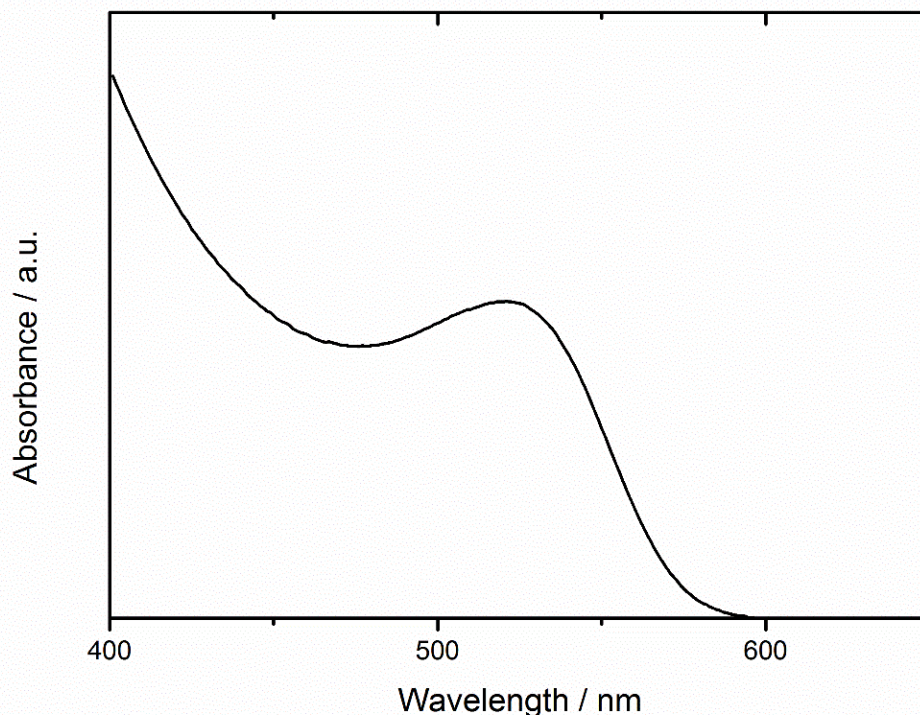
Figure 4. Typical absorption spectrum for a sample of colloidal QDs. The peak at 525 nm corresponds to the first "1s" excitation. The absorption increases at shorter wavelengths, corresponding with an increase in available states at higher energies.

1.3.4 Excited State Dynamics – Emission and Trapping

In the previous section, absorbance of photons by QDs was discussed. Each absorbance event results in a QD that is in an excited state; in almost all cases with the exciton at an energy at least that derived in section 1.3.2. In other words, the promoted electron has an

energy that lies at least above the conduction band minimum, with the hole at least below the conduction band maximum. These electrons and holes are termed "hot". In bulk semiconductors, hot carriers rapidly return to the band edge via phonon emission, in a process known as thermalisation. The continuum of energy states present in bulk semiconductors allows cooling of the electron and hole in approximately one picosecond.[41] The picture is different, however, when the carriers are confined as in quantum dots. As the size of the QD decreases, energy bands separate into discrete states, and the energy separation of these states will tend to increase with the confinement. Below a certain size for a given material, the separation between electron states will exceed the maximum phonon energy, which will disallow direct thermalisation of electrons. The phonon energy is limited; its minimum wavelength cannot be less than twice the atomic separation. For example, the distance between the two lowest energy electron states in CdSe QDs (the 1s and 1p states) can be 10 times greater than the phonon energy. This prevention of direct thermalisation is known as the phonon bottleneck.[42] In early theoretical treatments of quantum dots, the phonon bottleneck was expected to result in arbitrarily long cooling lifetimes in QDs,[43, 44] however lifetimes typically measured are of the order of a few picoseconds[42, 45, 46] suggesting the presence of other cooling processes. Auger processes describe some of these; the closer spacing of energy levels in the valence band allows holes to cool quickly via phonon emission. A hot electron can therefore transfer energy to a hole that has already cooled to the VBM.[35, 46] This process is illustrated in figure 5.
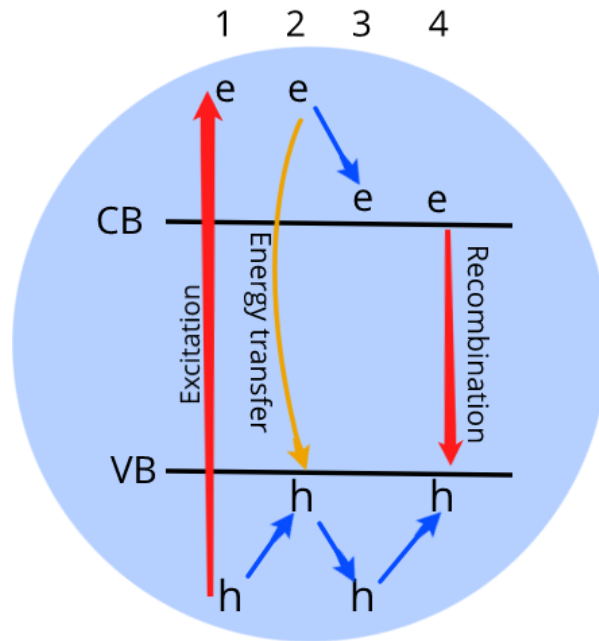
Figure 5. Avoiding the phonon bottleneck. 1) Excitation creates a hot electron-hole pair. The hole cools to the VBM via phonon emission. 2) The hot electron cools to the CBM via transfer of energy to the hole (an Auger process), which is excited again. 3) The hole cools to the band edge via phonon emission. 4) The electron and hole recombine from the band edges.

Even the largest QDs are of the order of a few nm in size; a consequence of this is that a large proportion (up to 60%) of the constituent atoms of any QD are associated with the surface.[31] In a typical sample of colloidal QDs, some of these atoms will be passivated by organic ligands, but steric limitations usually dictate that a number of atoms will be left with unsaturated "dangling bonds". It is these under-coordinated atoms in particular that can provide "trap" states for both electrons and holes, which can provide additional cooling pathways. These "shallow" surface states are also commonly associated with non-radiative recombination of the electron and hole, and therefore are associated with losses in photoluminescent quantum yield (PLQY), which is usually an undesirable property.[47, 48] "Deep" intra-gap trap states are common in defect tolerant materials such as chalcopyrites, and have been shown to be involved in efficient radiative recombination of excitons. They usually exist due to point-defects within the structure of the QD and so are not necessarily associated with the surface.[49, 50]

It is the presence of both trap-mediated and Auger-mediated cooling processes that account for the apparent lack of the phonon bottleneck; these processes are fast and usually result in cooling of electrons in a few (1-10) picoseconds.[46]

To passivate surface trap states associated with non-radiative recombination of excitons, it is common to over-coat the "core" quantum dot with a shell of a material of a different band gap. The excitonic properties of these core/shell QDs depend on the relative band structures of the core and shell material, illustrated in figure 6.
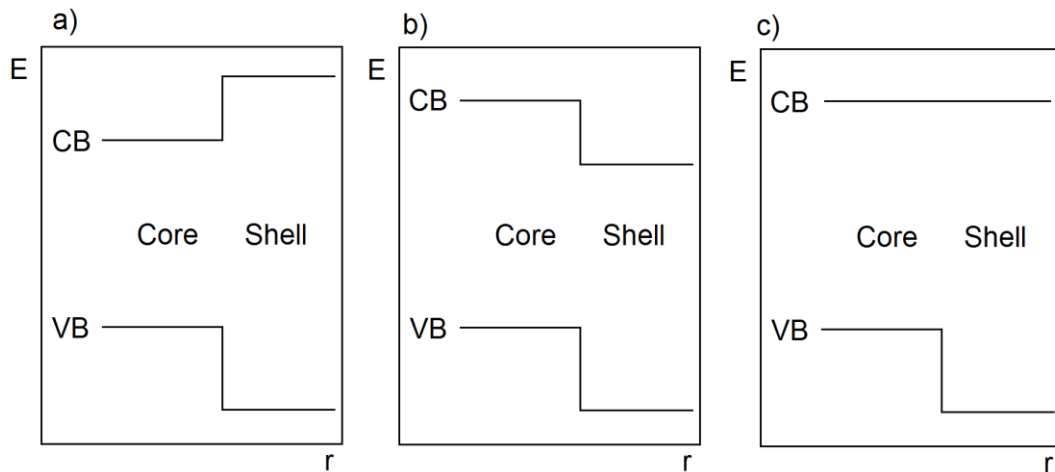
Figure 6. Schematics of various band alignment behaviours in core/shell QDs. a) Type-I behaviour: the shell has wider band gap than the core, and the electron and hole are energetically confined to the core. b) Type-II behaviour: the electron is confined to the shell and the hole to the core. c) An example of quasi-type-II behaviour: the electron is delocalised while the hole is confined to the core.

If the core is over-coated by a material of much wider band gap, type-I behaviour is typically observed. Due to the wider band gap of the shell, the exciton is confined to the core, similarly to how it would be were there no shell present. However, addition of the shell material usually serves to passivate the dangling bonds of the atoms on the core surface, and so the trap states associated with them are no longer present. The result is usually an increase in the quantum yield of the QD sample as non-radiative recombination via trap states is decreased.[51] Type-I behaviour is observed in CdSe/ZnS and $CuInS_2$/ZnS as examples.[39]

Type-II behaviour exists when the band alignment between core and shell exists such that one of the charge carriers of any given exciton is localised to the core, and the other is localised to the shell. This behaviour typically results in longer recombination lifetimes, and

the localisation of one of the charge carriers to the shell can allow for efficient charge extraction, while also typically supressing Auger recombination. CdTe/CdSe, CdSe/ZnTe and GaSb/GaAs are all examples of core/shell QDs that can exhibit type-II behaviour.[52-54]

Also illustrated in figure 6 is a quasi-type-II behaviour, where one charge carrier (either the electron or hole) is localised (usually to the core) and the other is delocalised across the whole QD. This behaviour can exist in CdTe/CdS and CdSe/CdS QDs.[55, 56]

For effective passivation of surface states, a shell material must be chosen that not only has the correct band alignment with the core, but has a lattice that can be closely matched. It is for this reason that ZnS is the most popular shell material; it has a small lattice mismatch (< 5%) with the most common QD materials, such as CdX and most chalcogenides, has a significantly wider band gap, and is more resistant to oxidation. A small lattice mismatch allows epitaxial growth of the shell on the core QD, allowing effective passivation with thin shells.[57] A large lattice mismatch, or an excessively thick shell can result in dislocations in the lattice due to strain, and these can provide "trapping" centres for non-radiative recombination.[58]

All QDs discussed in this thesis are colloidal QDs, meaning that they exist in a suspension either in organic solvents or the aqueous phase. Colloidal stability requires the presence of ligands on the surface of the QD compatible with the dispersion medium. It is also common to have other ligands in order to functionalise the QD; the roles of ligands with respect to stability and functionalisation will be discussed in sections 1.5-1.7. As mentioned before, atoms on the surface of a given QD represent a high proportion of the total, and contribute to the optical properties, particularly with respect to the excited state dynamics. Consequently, surface–bound ligands are likely have an effect on the excited state dynamics of the QD.

Electron-donating ligands are effective at passivating electron traps; as mentioned before, these traps are typically associated with "dangling" bonds on the QD surface, which in CdX QDs typically arise from under-coordinated cations (Cd^{2+}). Thiolates and amines are particular examples of highly passivating ligands, as they are capable of donating σ electrons, whose symmetry matches that of the electron accepting orbital in Cd^{2+}. Thiolates are particularly important in this regard; they often have a large binding constant for many of the most common QD materials, which makes them popular choices for use in QD functionalisation.[59] Aside from passivating electron traps, thiolates can act to introduce hole traps, thus making their effect on the excited state dynamics of the QDs complex. The S

atom present in a thiolate has three lone pairs; the first of these lone pairs serves to supply electron density to the under-coordinated cation, while the other two can act as mid-VB hole trapping states.[60, 61] Other ligands such as phosphines and carboxylic acids have also been shown to display similar hole trapping behaviour.[62, 63] In CdTe QDs, which are one of the main foci of the experiments in this thesis, thiolate ligands tend to result in an improved QY, as they do not form hole trap states energetically accessible by VBM holes.[60]
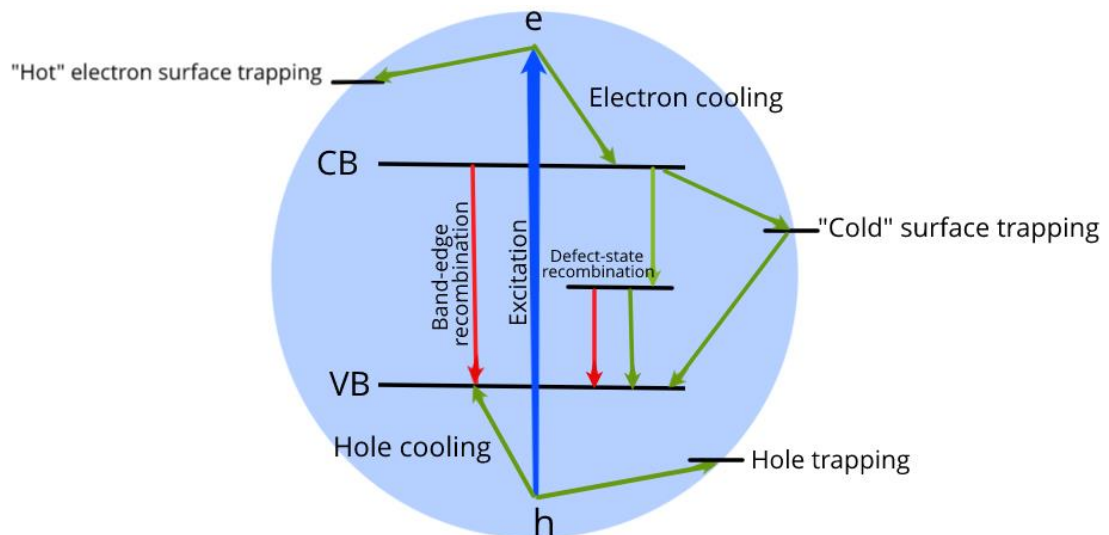
Figure 7. Scheme of possible recombination or trapping processes in colloidal QDs. Typically emissive and typically non-emissive processes are denoted with red and green lines, respectively.

1.3.5   Charge transfer from quantum dots

As discussed before, excitation of a QD results in the creation of an exciton consisting of an electron and hole, which are to some degree delocalised about the QD. If either of these charge carriers is extracted from the QD, radiative recombination will not occur. This can happen in two ways:

1) An excited electron is transferred to an external *electron acceptor*; the QD is therefore the electron *donor.*

2) An electron is externally donated to the valence band of the excited QD, non-radiatively recombining with a hole. In this case, the QD is the *electron acceptor.* Alternatively, this can be considered as a transfer of a hole to an external *hole acceptor,* where the QD is a hole *donor.*

For the discussion of electron transfer, this thesis will use the notation whereby the transfer of electrons is considered. For molecular electron donors (or acceptors) a general rule can be stated that the highest occupied molecular orbital (HOMO) of a donor quencher must lie energetically above the valence band, and the lowest unoccupied molecular orbital (LUMO) of an acceptor must lie below the conduction band.[28] Exceptions to this rule exist if the transfer involves states other than those at the CBM or VBM in the QDs, such as high-lying hot states or trap states. These transfer events, however, are rare, as the rate of electron transfer is typically slower than that associated with cooling to the minimum energy QD state.
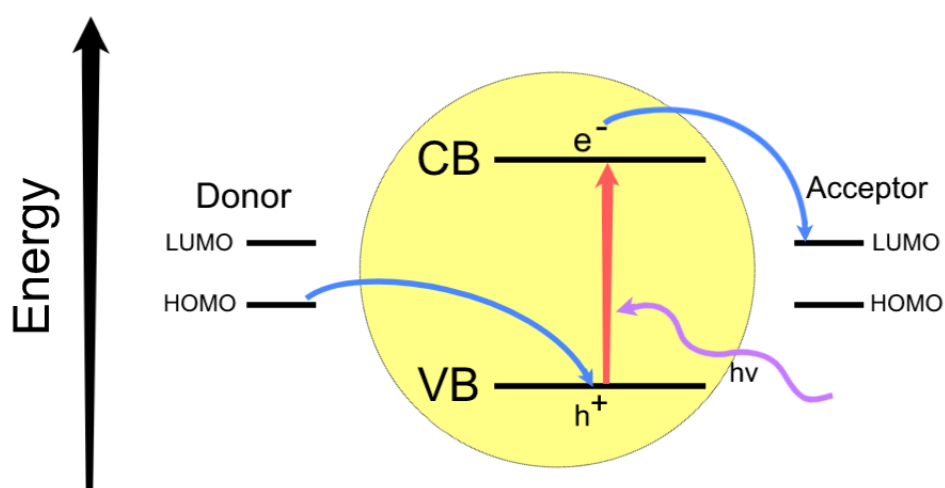
Figure 8. Simplified schematic of quenching by electron transfer in quantum dots. For quenching by charge transfer to be likely, the HOMO of a donor quencher must lie energetically above the valence band, and the LUMO of an acceptor must lie below the conduction band.

The rate of an electron transfer event is described by the following expression, as derived by Freeman and Willner:

$$K_{CT} = \frac{4\pi^2}{h}\left(T_{DA}^0\right)^2 e^{-\beta(R-R_0)}\frac{1}{\sqrt{4\pi\lambda k_b T}}e^{-\frac{(\Delta G^0 + \lambda)^2}{4\lambda k_b T}} \qquad (20)$$

In this expression, R is the distance between donor and acceptor, ΔG^0 is the free energy change associated with the transfer event, and λ is the associated reorganisation energy. IN addition to these, R_0 is the van der Waals distance, β is the electronic coupling constant, and

k_bT is the thermal energy.[28] The important result for sensors is that the rate has an exponential dependence on the distance, as well as an exponential dependence on the square of the free energy. The consequences are that the electron transfer, and therefore the quenching of luminescence by electron transfer, are strongly sensitive to and therefore can be altered by the distance between donor and acceptor. In addition to this, the free energy will depend on the chemical state of the acceptor – oxidising or reducing the acceptor in a reversible fashion will therefore reversibly change the transfer efficiency.

1.3.6   Stern-Volmer Theory

Transfer of a photo-excited electron results in quenching of PL, as radiative recombination of the exciton is no longer possible. For QDs in solution with free quenchers, the degree of quenching is described by the Stern-Volmer equation:

$$\frac{I_0}{I} = 1 + k_q\tau_0[Q] = 1 + K_D[Q] \tag{21}$$

In this expression, I_0 and I are the PL intensities without and with quenchers, respectively, τ_0 is the PL lifetime with no quenchers, [Q] is the quencher concentration, and k_q is the quenching constant; K_D is known as the Stern-Volmer quenching constant for the particular system.[64]

For free quenchers, $\frac{I_0}{I}$ will be linearly proportional to quencher concentration. However, for the case where quenchers permanently associate with QDs (such as QDs conjugated to redox sensitive acceptors) the statistical distribution of quenchers across the QD population becomes important. If the proportion of a sample of QDs with n quenchers is $P(n)$, then the total intensity of a sample can be written as follows:

$$I = I_0 \sum_{n=0}^{\infty} P(n)(1 - K_D)^n \tag{22}$$

For quenchers randomly populated around QDs to which they are permanently bound, $P(n)$ will follow a Poissonian distribution, if each quencher is responsible only for the quenching of PL of a single QD.[59, 65] This treatment considers the average effect of quenchers populating QDs; variations between QDs in a real sample (such as variations in the number of traps on each QD) will mean some QDs are more quenched than others.[45]

1.4   Synthesis of Quantum Dots

To accurately tune the emission of QDs, synthesis procedures that allow accurate control over the average size of QDs as well as the size-polydispersity of a sample must be used. For colloidal QDs suitable for use in biosensing, "bottom-up" wet chemical techniques are

universally preferred over top-down subtractive techniques used to fabricate some of the first QDs. Using wet chemistry allows QDs to be synthesised in large batches with tight control over size and polydispersity, and provides opportunities for formation of hetero-structured QDs (such as core/shell morphologies) for better optical properties.[66]

Typical synthesis techniques involve growth from solutions prepared by pyrolysis of organometallic precursors in organic solvents, or dissolution of suitable metal salts. In order for a crystal to grow from the resulting solution, an initial nucleation event must occur, the thermodynamics of which can be modelled using classical nucleation theory. The free energy change associated with this nucleation is given by:

$$\Delta G = n(\mu_C - \mu_s) + A\gamma. \tag{23}$$

In this expression, n is the number of atoms in the newly formed crystal nucleus, μ_C and μ_s are the chemical potentials of the atoms in the crystal and solution phase respectively, A is the surface area of the crystal, and γ is the surface energy associated with the crystal-solution interface. Defining the nanocrystal length scale a, the above expression can be generalised to the following:

$$\Delta G = NCa^3(\mu_C - \mu_s) + Da^2\gamma. \tag{24}$$

Here, C and D are constants that relate the crystal's size to its volume and area respectively, and N is the number of atoms per unit volume. Typically, $\mu_C - \mu_s$ will take a small negative value, and the barrier to nucleation will therefore be due to the surface energy of the new crystal. As the first, negative term is proportional to the cube of the size, above a certain critical size a_c, the change in free energy for an increase in size will be negative, and therefore above this size any crystal that is formed will be stable.

The free energy change required to obtain the critical nanocrystal size is the nucleation energy, ΔG_{nuc}, and is obtained from thermal fluctuations.[67] In order to achieve nucleation at practical temperatures, the nucleation energy can be tuned by changing solvent conditions, concentration of precursors, as well as concentrations of ligands that coordinate crystal precursor ions in solutions and modify their solubility.

Once a stable crystal has nucleated, further growth will be limited by the rate at which new constituent atoms can diffuse to the surface from the solution. At the same time, as the crystals in a solution grow larger, the concentration of precursor materials will decrease. This has a limiting effect on the size of the crystals growing in any particular solution; as the concentration of precursors in the solution decreases, the value of μ_s will decrease, and

therefore the value of a_c will be larger. The result is known as Ostwald ripening, the phenomenon that larger crystals grow at the expense of smaller crystals; the maximum size of the crystals is limited by diffusion.[68] By controlling the reactivity of the precursor materials by choosing appropriate solvents, coordination ligands and concentrations, as well as the growth temperature, this behaviour can be exploited to produce high quality, monodisperse samples of QD nanocrystals.[66] This is typically achieved by limiting the reactivity of precursors to achieve gradual nucleation of crystals. If the nucleation and initial growth step occurs too quickly, all precursor materials are instantly consumed, and growth occurs only through Ostwald ripening, resulting in a broad final size distribution.[69]
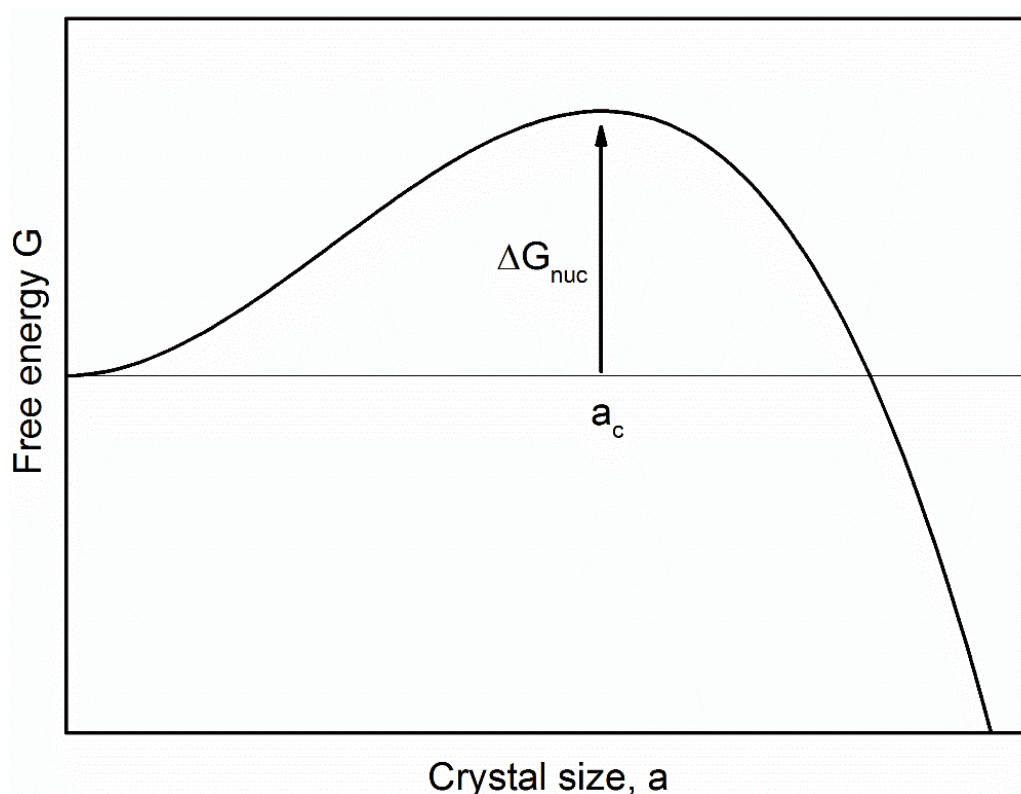
Figure 9. Free energy vs crystal size. Crystals larger than the critical size a_c are stable as an increase in their size results in a net decrease in free energy. ΔG_{nuc} is the free energy required for nucleation.

In 1993, Bawendi et al demonstrated trioctylphosphine (TOP)-directed growth of CdX (X= Te, Se, S) QDs in solution, which exhibited excellent, controlled optical and colloidal properties.[70] Since then, organic-phase synthesis routes have perhaps been the most popular; the high temperatures achievable using low-volatility long-chain organic solvents is ideal for a wide range of semiconductor materials.

To achieve water-dispersible QDs without requiring ligand exchange or other phase-transfer techniques, recent literature has shifted toward aqueous synthesis routes for a number of QD materials.

1.5   Colloidal properties of QDs

QDs for biosensing are universally colloidal QDs, meaning that they exist in some suspension, usually in the aqueous phase. This necessitates the presence of some sort of water-compatible stabilising agent on the surface of the QD. Typically, but not universally, high (>150°C) temperatures are required to synthesise the QDs, which precludes the use of aqueous synthesis routes. The result of this is that most colloidal QDs post synthesis have surfaces populated with hydrophobic ligands, which presents a challenge when transferring into the aqueous phase for application. There are a number of ways to achieve this phase transfer, however; these ligands can be replaced by careful exchange procedures, removing hydrophobic ligands while simultaneously replacing with hydrophilic ones, and transferring into the opposite phase. An advantage of this is that the overall hydrodynamic size of the particle is not greatly affected. Ligand exchange procedures, as they are called, are however notoriously finicky and highly sensitive to concentrations of reagents, as well as ambient salt conditions, pH and temperature. In a number of QD types, losses of PLQY are likely to occur due to incomplete replacement of ligands involved in passivation of surface trap states.[71-73]

Encapsulation in hydrophilic polymers represents another strategy for transferring hydrophobic QDs into the aqueous phase. Polymers can be grafted onto QDs by covalent reaction with already present ligands, or amphiphilic polymers can conceal the QD surface via hydrophobic interactions. Due to the addition of large molecular weight polymers, encapsulation techniques usually result in a greater final hydrodynamic size, however these phase transfer procedures tend to be more reproducible than ligand exchange strategies.[74-76] In a similar manner to polymer encapsulation techniques, the amphiphilic nature of lipids is often used to achieve transfer of QDs into the aqueous phase; the hydrophobic QDs are concealed within lipid micelles.[77]

More recently, aqueous-phase synthesis techniques have been developed that produce QDs with excellent optical properties. These QDs typically have small molecule surface ligands in situ that provide charge mediated colloidal stability provided by carboxyl or primary amine functional groups. A drawback of this strategy is the sensitivity of the colloidal stability to

changes in pH or high salt concentrations that act to screen the stabilising surface charges.[78]

Almost all of the above strategies for achieving transfer of hydrophobic QDs into the aqueous phase can be used for more specific modification of the QD surface chemistry. Importantly for biosensing QDs, additional functionality can be added to the QDs by addition of ligands with purposes other than achieving colloidal stability. These can include small molecules, polymers, peptide and large proteins, and can fulfil functions from targeting of certain biological structures to chemical sensing. More exotic surface modifications are also possible; QDs can be conjugated to PL-quenching metal nanoparticles, or to QDs with different emissive properties for multiplexed sensing.

1.6   Toxicity of QDs and Cell Uptake

QDs for biosensing applications are most commonly based on CdX (X= Te, Se, S) chalcogenides usually with a ZnS or CdS shell, but a gamut of materials from PbS to $CuInS_2$ chalcopyrites have been used. Other than achieving improved optical properties by passivation of trap states, as described in the previous section, the shell may be used to improve the chemical properties of the QD, particularly in relation to toxicity and resistance to oxidation. For example, "leaching" of cadmium from CdX (X= Te, Se, S) quantum dots is associated not only with short-term toxicity in in-vitro experiments, but with chronic toxic effects in vivo as well.[79-82] Addition of a ZnS shell has been shown to reduce these effects, in tandem with greatly improving their optical properties.[83] Other efforts to develop less-toxic QDs for biological application have focussed on semiconductors that do not contain cadmium, such as $CuInS_2$ and InP.[84, 85]

It is not only the constituent chemistry of the QD that dictates their biocompatibility (or, at a minimum, their toxicity). Both the chemical properties of the capping ligands, and the physical properties of the QD as a colloid can affect toxicity. It has been shown that toxicity of CdX QDs stabilised by small molecules can vary greatly depending on surface charge. Hydrodynamic size also plays a role; depending on the properties of the capping ligand, different QD sizes can result in different fates once taken up by cells, which can greatly affect toxicity.[86]

For most biosensing applications it is necessary to achieve uptake of colloidal QDs into biological cells. Many cell types are capable of naturally taking up QDs by means of endocytosis. Endocytosis describes a number of processes whereby matter exterior to the cell is taken in, and includes phagocytosis ("cell eating" or ingestion of solid matter) and

pinocytosis ("cell drinking" or ingestion of the solution exterior to the cell). Endocytosis of QDs is sensitive to both biological and physical factors, particularly the surface charge and size of the QD, as well as extraneous properties such as pH, salt concentration, and viscosity of the surrounding medium. Endocytic processes can be vectored by a number of biological processes, but can be enhanced for QDs by functionalisation with endocytosis-promoting agents, from positively charged lipids to cell penetrating peptides. For QDs intended for biosensing, the major limitation of endocytosis-mediated uptake into cells is that the QD typically resides within a vesicle (termed an endosome), and is chemically isolated from the cell cytosol.[87] QDs tend to remain aggregated within the endosomes, and their usefulness as a biosensor or label is likely to be compromised. Within the literature discussing QD biosensors, there is also unfortunately often limited discussion of the fate of the QDs within the cell, and limited evidence that QDs imaged within the cell truly are within the chemical environments in which they are purported to be.[88, 89]

Some polymeric transfection reagents, such as PEI (polyethylenimine) are proposed to allow endosomal escape by the "proton-sponge effect"; these polymers are effective buffers and can counteract the usual drop in pH experienced during endocytosis. Un-protonated amines can absorb protons as they enter the endosome, preventing the reduction in pH. To counteract this, the number of protons pumped into the endosomes is increased, which eventually results in a greatly imbalanced salt gradient (particularly with respect to Cl$^-$ ions) and subsequent osmotic lysis of the endosome.[90]

To avoid the problems posed by endocytosis for biosensing QDs, there has been a development in efforts to achieve non-endocytic uptake of QDs. Most of these technologies involve inducing the formation of holes or pores in the cell membrane (poration), allowing non-specific diffusion of functionalised QDs into the cell interior. Sonoporation and electroporation trigger poration of the membrane from cavitation of ultrasound-generated microbubbles near the cell membrane and high-frequency electric fields respectively, and typically do not have a greatly adverse effect on the viability of the cells; use on QDs is developing but these techniques are widely used for achieving non-specific uptake of small molecules.[91, 92] Microinjection, where cells are individually injected with small volumes of QD solution, allows guaranteed delivery of QDs to the cytosol at the cost of very low throughput.[89, 93]

1.7   Current QD Redox Sensors

The majority of QDs biosensors operate on a fluorimetric principle, whereby either the photoluminescent emission intensity or lifetime is altered depending on the state of a sensing moiety of some molecule close or attached to the surface. It is therefore a necessity that there is some interaction between any photogenerated exciton within the quantum dot and the sensing moiety, and that this interaction is modified (ideally reversibly switched) depending some interaction between the sensing moiety and the intended analyte. Most redox-sensing and pH-sensing QDs operate on the principle of quenching of luminescence depending on the chemical state of the sensing moiety, either by Förster resonance energy transfer (FRET) or photo-induced charge transfer, which most commonly involves transfer of the excited electron to an external acceptor.[27] A typical QD sensor will consist of a QD, the sensing moiety, and a "linker" which connects the two. This linker may be formed by the use of bioconjugate techniques, such as by exploitation of the affinity of biotin and streptavidin, or by a simple alkyl chain.

FRET is a non-emissive energy transfer process whereby an excited fluorophore (termed the donor) loses energy associated with its excitation by transfer to an acceptor, which can be fluorescent or non-fluorescent itself. This occurs over short distances when the emission spectrum of the donor has overlap with the absorption spectrum of the acceptor. The energy transfer does not involve the emission and re-absorption of a photon, but occurs via a dipole-dipole interaction between donor and acceptor.[64] The efficiency of a FRET process scales with the inverse sixth power of the separation between donor and acceptor, and therefore is often termed a "spectroscopic ruler" due to the sensitivity this affords.[94]

While FRET between QDs and molecular dyes has been understood and achieved since soon after high quality photoluminescent colloidal QDs were first synthesised, development of the first applicable   biosensors operating on this principle took until the mid-2000s. A breakthrough came in 2003, when Medintz et al reported a competitive binding assay for sugars based on QDs self-assembled with maltose binding protein. Adding β-cyclodextrin-QSY9, a dye-conjugated sugar, served to quench QD luminescence via non-emissive FRET. Addition of maltose competitively inhibited the binding of β-cyclodextrin-QSY9, resulting in the recovery of luminescence.[95] A particularly elegant early example of a FRET-based redox biosensor is that by Freeman and Willner, who developed an NADH-sensitive probe consisting of a CdSe/ZnS core shell QD conjugated with the dye Nile blue. Before addition of NADH, photoluminescence of the QDs was largely quenched due to non-emissive FRET to

the conjugated Nile blue. Upon addition of NADH to an aqueous solution of these QDs, the Nile blue was reduced along with NADH oxidation and fluorescence was seen to recover. The same QDs were then shown to be sensitive to the activity of alcohol dehydrogenase in the oxidative breakdown of ethanol.[96]

Charge-transfer (CT) based sensors are distinct from FRET-based sensors in that the depopulation of excited states involved in photoluminescence is achieved by removal of the excited electron or hole, and not by energy transfer between charge carriers. This has a number of consequences for the properties of such sensors. The dependence on distance for electron transfer between QDs and is exponential, which means acceptors must still be near the QD, however at relevant distances this dependence is not as steep as the distance dependence for FRET sensors.[28] Compared to FRET based systems, there is a wide library of useful acceptors that do not exhibit their own fluorescence. For FRET acceptors that do exhibit their own fluorescence, the signals from donor an acceptor must be deconvolved from one another to find the FRET efficiency, which is not necessary in charge transfer systems where the electron transfer is typically measured by observing the degree of quenching. Another advantage is the possibility of using QDs of different emission wavelengths with the same acceptor, as there is no requirement for matching of emission and excitation. Both of these properties allow for multiplexing of a number of different QDs which can be excited at the same wavelength. Despite the above, studies on CT-based QDs biosensors are less numerous than on FRET-based systems. This is likely due to the simplicity involved in pairing a particular QD and FRET acceptor; initially these can usually simply be chosen on the basis of spectral overlap. Furthermore, the numerous possible processes involved in any transfer event, along with sometimes conflicting results for some systems (examples being QDs with ferrocene and dopamine, discussed later) make their study more difficult.[97-99]

There are many ways of exploiting the charge transfer from an excited QD to an acceptor (or vice versa) for the purposes of sensing, however the most notable strategies are:

1) Measuring the change in transfer efficiency, and in turn the degree of quenching as the acceptor/donor undergoes a conformational change, increasing or decreasing the transfer distance.

2) Measuring association or dissociation of the acceptor/donor from the QD surface through the degree of quenching. This can involve reversible or non-reversible processes in either direction.

3) Changing the redox state of the acceptor, allowing or disallowing transfer of an electron or hole. For these QDs, the acceptor is usually attached to the surface of the QD by some sort of molecular "linker".

Since approximately 2005 the literature on charge-transfer-based QD biosensors has increased dramatically. Sandros et al published a number of studies on probes of the first type in the list above, for detection of sugars.[100, 101] These represented some of the first applicable CT probes, and involved quenching of the QDs by charge transfer from a ruthenium complex linked to the surface by maltose binding protein (MBP) which binds a number of sugars with varying affinity. A binding event of a sugar to the MBP resulted in a conformational change which increased the charge transfer distance, reducing the quenching from approximately 22% to almost zero. This PL-quenching charge transfer event was suggested to be electron transfer from the ruthenium complex to the QD valence band. A later study by the same group extended the concept for detection of low concentrations of lead in solution,[102] however this technology is not limited to conformational changes in proteins; other small molecules such as nucleic acids have also been used to achieve change in the charge transfer distance.[103]

For sensors in the second type in the above list the literature is much broader, and similar strategies have been used for both FRET and charge transfer (CT)-based probes. The simplest cases involve attaching some quencher with a "linker" that is cleavable by the desired analyte, freeing the quencher and increasing the photoluminescence. CT-based systems that use this strategy started with work by Mattoussi et al, who again used PL-quenching ruthenium complexes, this time conjugated to QDs of varying emissive properties by carefully chosen peptides. These peptides were selected as they are digestible by thrombin and chymotrypsin, enzymes involved in blood coagulation and digestion respectively. Adding these enzymes resulted in the recovery of PL from approximately 80% quenched, due to the digestion of the peptides and subsequent separation the QD and acceptor. This results in a probe that is useful for measuring enzyme velocity and reactivity, but can also be adapted for more in-depth studies of enzyme inhibition.[104] A separate ground-breaking development came with the work of Raymo et al in 2006, using the famous biotin-streptavidin binding interaction as their model system. Biotinylated cationic electron acceptors based on methyl viologen were electrostatically immobilised on the surface of the negatively-charged QD, resulting in efficient quenching of the PL. Addition of streptavidin, which binds tightly to biotin, disrupted the electrostatic attraction between QD and acceptor, and resulted in recovery in the PL as the methyl viologen dissociated.[105]

More recently, focus has been on systems of the third type in the above list, which involve changing the redox state of a bound electron or hole acceptor (or electron donor) ligand to energetically allow or disallow any particular transition. If the reduction potential of this ligand is chosen carefully, it can allow fluorimetric redox sensing in a regime useful for biology. It is these systems in particular that are the subject of this thesis.

An early study of particles of this type was from the Nadeau group, who in 2006 measured the variation in PL of dopamine-conjugated CdSe/ZnS core shell QDs within cells, as the reducing environment within the cell was changed via biological means. In this study, more oxidising conditions resulted in higher luminescence, particularly in cells expressing high levels of dopamine receptors. The quenching was attributed to hole trapping by the reduced dopamine.[99] Since then, dopamine-conjugated QDs continue to be widely studied; in 2010, Mattoussi et al reported a similar dopamine-conjugated CdSe/ZnS system which exhibited redox sensitivity in the opposite sense. In this case, reducing QD-bound dopamine disallowed transfer of an excited electron from the QD to the dopamine, and resulted in an increase in PL. The pH-dependent nature[106] of the reduction potential of dopamine was then exploited to produce a charge-transfer coupled pH sensor, which was applied for pH sensing within biological cells.[98] Dopamine is an ideal choice as a sensing moiety for these biosensors, as it has a reduction potential that is biologically relevant; it participates in redox reactions in its numerous roles in biology.[107, 108] In order to design other QD biosensors of this type, it is therefore often useful to take inspiration from other biologically-relevant redox pairs.

Nicotinamide adenine dinucleotide (NAD) is one of these compounds; it is a coenzyme found in all living cells and is involved in a number of steps in the metabolic pathway, as well as other reactions. It is principally involved in electron transfer, and therefore exists in two forms; the oxidised NAD+, and the reduced NADH. One example of a biochemical process in which NAD is involved is the conversion of alcohols into aldehydes via alcohol dehydrogenase (alc-DH) enzymes, via reduction of NAD+ into NADH. In yeasts and bacteria involved in fermentation, alc-DH enzymes operate in the opposite sense, producing alcohols and oxidising NADH into NAD+. Willner and Freeman have exploited this biological relevance to develop high quality biosensors for NADH/NAD+-dependent enzymes. In this case, NAD was conjugated to CdSe/ZnS core/shell QDs, and the PL was dependent on the redox state of the NAD in the same sense as described before; the oxidised NAD+ is an electron acceptor, and is therefore capable of quenching PL due to electron transfer from the excited QD. The resulting probes were able to follow in vitro the activity of the alc-DH in the breakdown of

ethanol. The probes were then used for the detection of the explosive RDX in a similar manner.[109]

Coenzyme Q_{10} (CoQ$_{10}$, also known as ubiquinone) is another important metabolic coenzyme, most importantly involved in aerobic cellular respiration.[110] It exists in three forms: fully oxidised, semi-reduced (an unstable intermediate), and fully reduced. These forms are known as ubiquinone, semiubiquinone, and ubiquinol repectively, and are illustrated in figure 10. This important property allows ubiquinone to act both as a single- and double electron carrier when involved in redox reactions. The Long group published a study of ubiquinone derivatives conjugated to CdTe/ZnS QDs. The QD conjugates exhibited redox-sensitive fluorescence, again due to an electron transfer from the excited QD to the oxidised ubiquinone derivatives (QnNS), resulting in quenching. This quenching was prevented by chemical reduction of the quinones. Using spectroelectrochemical measurement techniques, the dependence of the PL on the redox state of the attached quinones was investigated; it was possible to relate the redox state of the quinones as determined by cyclic voltammetry to the PL emission of the QDs. Another important result in this work was the investigation of the distance-dependence of the PL-quenching electron transfer; quinone molecules with shorter "linker" units exhibited more efficient quenching due to increased electron transfer probability. The QDs were then used to measure the concentration dependence of the oxidation of NADH to NAD+ by NADH dehydrogenase; the electrons from the oxidation of NADH are accepted by the QD-bound quinone, and the PL of the QD sensors increases as electron transfer to the quinones is disallowed. Within cells, the QD sensors were shown to be sensitive to the concentration of oxygen radicals, suggesting this technology could be used to assess the degree of damage by reactive oxygen species (ROS) in cells in various degree states.[111] In a later study, they moved to a different ubiquinone analogue, again with the intention of mimicking its behaviour within the cell, this time measuring reduction achieved by the enzyme complex I, an NADH dehydrogenase specific to ubiquinone. Within SH-SY5Y cells (a human neuroblastoma cell line) these QD probes were then shown to be reduced by complex I, switching "on" the PL, allowing visualisation of the spatial distribution of complex I within the cell.[112]
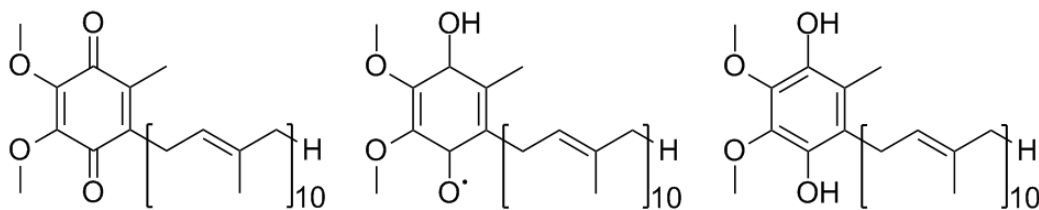
Figure 10. Ubiquinone (left) semiubiquione (centre) and ubiquinol (right). These are the fully oxidised, unstable intermediate, and fully reduced states of the electron-transporting cofactor coenzyme Q₁₀.

1.8 Scope for Further Research and Chapter Overview

The majority of research mentioned above has focussed on developing various sensing strategies, with regards to investigation of their chemical or biological function. There is still very limited literature discussing the importance of the excited state dynamics of the QD-acceptor system, and how these properties can be affected by the choice of the QD used. Most current QD-acceptor redox sensors are based on CdSe/ZnS or other type-I core/shell QDs, which do not typically offer efficient charge extraction, due to the location of the exciton within the core. There is therefore scope for further research into the mechanisms of charge transfer in QD-acceptor systems, especially for type-II, or quasi-type-II systems which may display greater charge extraction efficiency, and therefore greater sensitivity.

A general problem limiting the application of QDs in bioimaging and biosensing is their toxicity; especially for the most common or well-characterised QD types (typically Cd-based QDs). Particularly for redox sensing, where it is desirable to perform long-timescale experiments, it is desirable to have a QD that has little or no toxicity, and limited effects on biochemical processes of the cell. As mentioned above, $CuInS_2$/ZnS QDs have been posited as an excellent alternative QD due to their reduced toxicity, however, their excited state dynamics are poorly understood, and synthetic techniques that allow $CuInS_2$/ZnS in the aqueous phase without polymer encapsulation are not optimised.[49, 74, 113] A better understanding of the mechanisms of photoluminescence of these QDs is therefore required to understand and optimise charge extraction.

The experiments reported in Chapters 3, 4 and 5 of this thesis attempt to address these gaps in the literature. Chapter 3 details a study of the internal structural properties of $CuInS_2$/ZnS and $CuInS_2$ QDs and how they relate to the optical properties, with a view to improving their usefulness for biosensing.

In Chapter 4, a QD redox sensor based on quasi-type-II CdTe/CdS core/shell QDs, and the ubiquinone-derivative electron acceptor molecule Q2NS, is synthesised and characterised with a view to improve the understanding of the excited state dynamics of such a type-II QD/acceptor system. Chapter 5 discusses the application of these probes to live cell experiments.

2   Experimental Procedures

2.1   Synthesis of QDs

Two main QD types were synthesised; CdTe and CdTe/CdS core and core/shell QDs were synthesised via aqueous methods, stabilised by short charged organic thiol ligands (cysteamine, for an amine surface, and thioglycolic acid, for a carboxylic acid surface). These QDs were later used for most of the redox experiments. Also synthesised were $CuInS_2$ and $CuInS_2$/ZnS core and core/shell QDs, stabilised in hydrophobic organic solvents by dodecanethiol. These are candidates for less toxic QDs for bioimaging applications.

2.1.1   Thioglycolic acid-stabilised CdTe QDs

Zinc-blende CdTe/CdS core/shell quantum dots were synthesised via modification of literature methods.[78, 114] QDs suitable for redox sensing in live cells must be hydrophilic. In order to maximise charge transfer efficiency, the acceptor must be as close to the QD as possible, so phase transfer by polymer encapsulation is not ideal. The following synthesis procedure was chosen as it achieves stable, highly luminescent QDs that are dispersible in the aqueous phase, and does not involve a potentially difficult ligand exchange.

Typically, cadmium chlorate hexahydrate was dissolved in 50-100 ml ultra-pure water at a concentration of approximately 50 mM. Thioglycolic acid (TGA) was then added to the solution to achieve a TGA:Cd^{2+} ratio of 1.4, resulting in the formation of insoluble Cd^{2+}-thiolate complexes which cause the solution to become cloudy. The pH was then adjusted to 11.2-11.6 by careful dropwise addition of 1 M aqueous sodium hydroxide (NaOH). The increased pH serves to deprotonate the TGA so that the Cd^{2+}-TGA complexes are rendered soluble, and a clear, colourless solution is obtained. This solution was decanted into a three-necked flask, placed in a cool heating mantle, and attached to a reflux column within a fume hood. In a separate flask, lumps of aluminium telluride (Al_2Te_3 0.2-0.4 g) were added, and connected with and a supply of oxygen free N_2 gas such that the gas bubbled through the Cd^{2+}-TGA solution, as illustrated in figure 11. The aim of this step is to remove as much oxygen from the solution as possible; excess oxygen can cause oxidation of the CdTe and poor quality QDs. After an hour, around 10 ml 0.5 M degassed sulphuric acid was added to the flask containing the Al_2Te_3 lumps, resulting in the evolution of H_2Te gas, which travels with the N_2 flow into the main flask. CdTe precursor complexes are seen in the main flask as the solution turns a dark yellow/orange colour. After approximately 2 minutes, the gas flow is stopped, and the mixture is heated and stirred under reflux at 100 °C. An N_2 atmosphere at positive pressure was achieved using an oil bubbler. A disadvantage of this synthesis method is that

it is difficult to precisely control the amount of tellurium that ends up dissolved in the reaction mixture; it is expected that there is therefore an excess of cadmium precursor present, and the tellurium deficit limits the size of the QDs. This is exploited in the shell growth step, where the excess cadmium is used to grow a CdS shell.
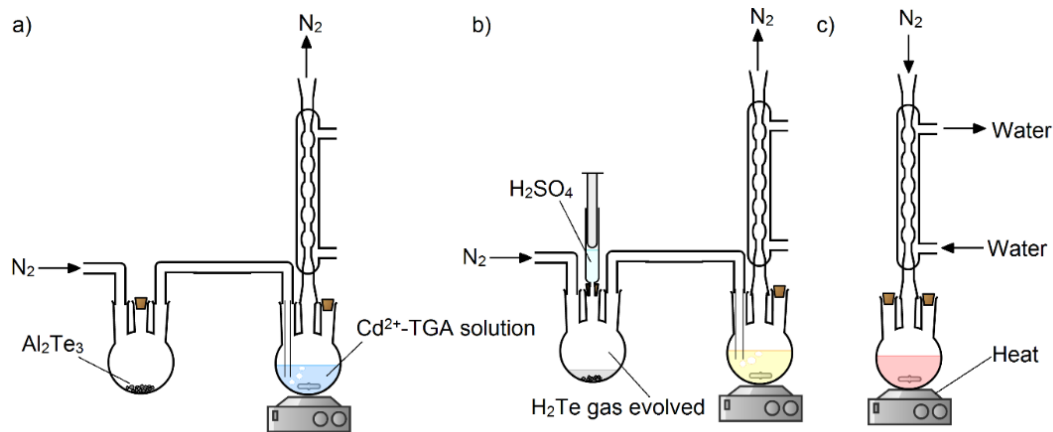
Figure 11. Schematics of equipment for synthesis of CdTe QDs. a) Apparatus during degassing of solution. Nitrogen is bubbled through the solution to remove oxygen. b) H_2SO_4 is added to the flask containing $Al_2Te_\mathsterling$ lumps, and H_2Te gas that is evolved bubbles through the Cd^{2+}-TGA solution forming coloured CdTe complexes. c) The resulting precursor solution is heated under reflux, resulting in nucleation and growth of CdTe QDs.

Once the QDs have reached the desired size, the growth is stopped by quickly cooling the reaction vessel by immersion in a room-temperature water bath. The solution turns from yellow-orange to deep red as the QDs nucleate and grow. The colour darkens with increased heating time as the QDs grow larger, and the absorption shifts further towards the red. Using this method, CdTe core QDs with emission wavelengths of approximately 520-650 nm can be achieved, with QD diameters from 1.8-6 nm, with growth times ranging from 2 minutes to 3 days.

In order to grow a CdS shell, an amount of thiourea sufficient to achieve a Cd:S ratio of between 1 and 3 was dissolved in a small amount (2-5 ml) ultra-pure water. This solution was added to the CdTe-TGA core QD solution, and the pH was readjusted to 11.2-11.6 to ensure colloidal stability. The solution was then refluxed at 100 °C for 1-2 hours, then stopped by immersion of the flask into a room-temperature water bath. This method relies on the presence of excess Cd-TGA precursor complexes in solution.
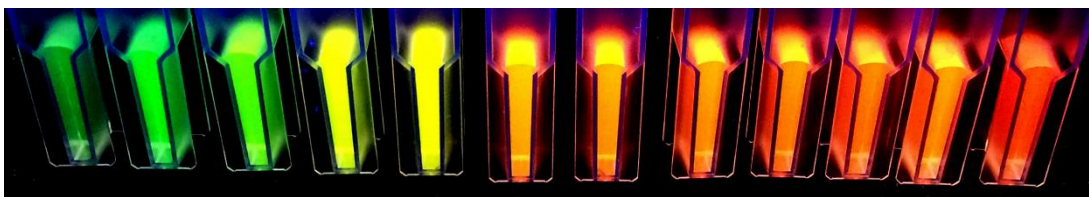
Figure 12. Size series of TGA-capped CdTe QDs, showing range of PL emission from green to red, achieved by varying the reaction time from 5 min (left, green) to 2 days (right).

2.1.2 Cysteamine-stabilised CdTe QDs

Positively charged, cysteamine-stabilised QDs were synthesised by the above method, with slight adaptations; thioglycolic acid was replaced with an equivalent amount of cysteamine hydrochloride, and the pH was instead adjusted to 5.5-5.9 to ensure colloidal stability.
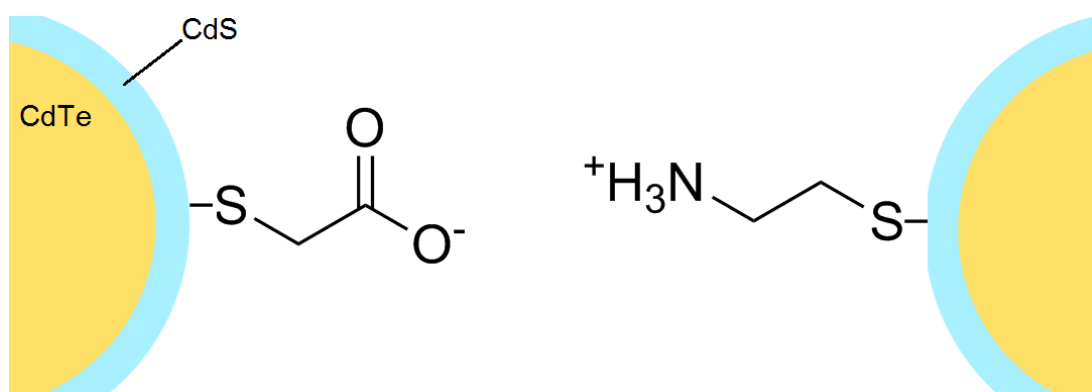
Figure 13. Scheme of surface capping strategies for CdTe/CdS QDs. TGA-capped QDs (left) have negative surface charge due to de-protonation of TGA, whereas cysteamine-capped QDs display positive charge due to protonation of the amine group in cysteamine.

2.1.3 CuInS$_2$ and CuInS$_2$/ZnS QDs

CuInS$_2$ core and CuInS$_2$/ZnS core/shell quantum dots were synthesised by a solvothermal method in octadecene (ODE).[39, 40] Typically, copper iodide (0.25 mmol) and indium acetate (0.25 mmol) were weighed into a three-necked flask, followed by 6 ml ODE and 4 ml dodecanethiol (DDT). The DDT exists in vast molar excess with respect to the copper and indium precursors, and acts both as a source of sulphur and a stabilising ligand for the resulting QDs. The mixture was then stirred under a protective argon atmosphere for 1-2 hours to remove oxygen. The temperature was then raised to 120 °C and monitored by means of a thermometer immersed in the reaction solution. The reaction mixture then changed from cloudy to a clear yellow colour as the powder metal precursors dissolve. The temperature was then raised to 180 °C, where nucleation of nanoparticles was indicated by the presence of a deep red colour. As the reaction progresses, the colour becomes darker,

and becomes nearly black after about 30 mins, indicating large nanoparticles which absorb across the visible spectrum. For the QDs discussed in this thesis, the reaction was stopped after 30 mins by rapidly cooling the flask by submerging in a room-temperature water bath. If the synthesised cores were to be used for the growth of $CuInS_2/ZnS$ core/shell QDs, the solution was cooled to approximately 100 °C to arrest growth, otherwise the solution was allowed to cool to room temperature.

The shell growth step follows a similar mechanism to the growth of the cores; the DDT acts as both a sulphur source and as a stabilising ligand for the resultant core/shell QDs. For addition of a ZnS shell to the $CuInS_2$ QDs, an amount of zinc stearate, sufficient to achieve a Cu:Zn ratio of 1:2 was added to a mixture of 1 ml ODE and 1 ml DDT. This solution was degassed under argon for 1 hour, and then heated to 100 °C and stirred, until the zinc stearate powder was seen to dissolve. This ZnS precursor solution was then added to the still-warm $CuInS_2$ core solution, which was subsequently refluxed at 180 °C for 1 hour. The growth is then stopped by quickly cooling the reaction vessel by immersion in a room-temperature water bath.
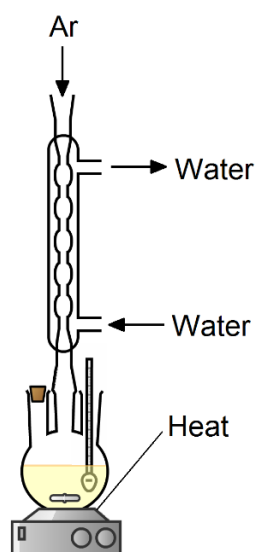
Figure 14. Apparatus for synthesis of CuInS₂ core and CuInS₂/ZnS core/shell QDs. The growth solution is heated in a temperature-controlled three-necked flask attached to a reflux condenser.

2.1.4   Cleaning of QD dispersions

After growth of the QDs has ceased, the QDs are suspended in an impure solution containing unreacted precursor materials and their by-products from pyrolysis. In the case of those QDs

synthesised in the aqueous phase, this solution will likely have a high salt concentration, incompatible with long-term stability of the QDs. The QDs were therefore purified by precipitation, then solvent extraction of impurities.

For the CdTe/CdS and CdTe QDs, the crude QD solution was diluted with a ten-fold excess of propan-2-ol at room temperature. This provides a solvent mixture in which the QDs will precipitate, but reaction by-products will still be dissolved. After 1 minute, the QDs were seen to precipitate as the solution became cloudy. The solution was then centrifuged for 10 minutes at 400 g in order to pellet the QDs. The supernatant containing impurities was discarded, and the QDs were resuspended in the minimum possible ultra-pure water (2-5 ml). The above procedure was repeated a further three times, and the QDs were suspended in ultra-pure water at a concentration of 5-10 µM for storage. Some of the QDs were then further cleaned by dialysis: the QD dispersions were decanted into regenerated cellulose membrane dialysis tubing (10 kDa) and sealed in volumes of 5-10 ml. The tubes were then dialysed in 2 l ultra-pure water for 24 hours.

Cleaning procedures were similar for the hydrophobic $CuInS_2/ZnS$ and $CuInS_2$ QDs; the crude solution was diluted ten-fold by a 10:1:1 acetone:chloroform:methanol mixture to precipitate the QDs, which were pelleted by centrifugation at 400 g. The supernatant was discarded, and the QDs were resuspended in the minimum possible volume of chloroform. Subsequent precipitation and centrifugation steps were performed by addition of enough methanol and acetone to preserve the 10:1:1 acetone:chloroform:methanol ratio. Similar dialysis procedures to those above were also followed; the same membranes were used, but chloroform was used as the dialysis medium.

2.2   Synthesis of Electron Acceptor Ligands

The quinone molecule Q2NS, initially described by Long et al, was used for the majority of the redox experiments. Q2NS consists of a quinone "head" group, which acts as the electron acceptor in charge transfer from QDs, conjugated via "click" chemistry to a disulphide "linker". Reduction of this disulphide bond allows thiolate bonds to form between the sulphur of the Q2NS and the cadmium ions on the CdS surface of the QDs.
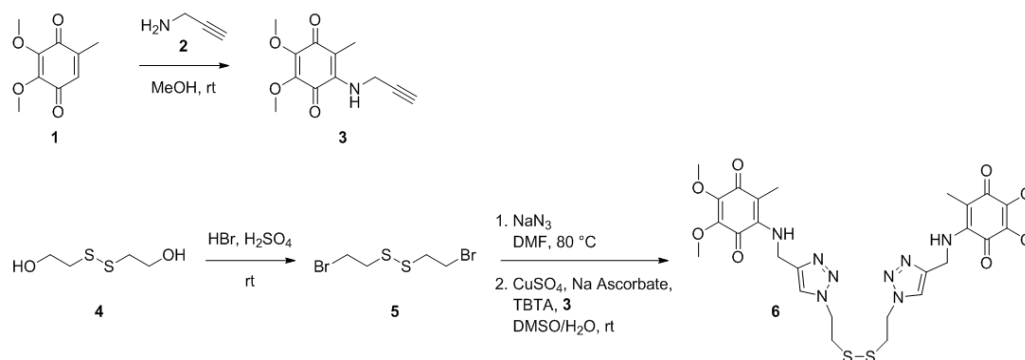
Figure 15. Synthesis route of electron acceptor Q2NS.

The synthesis method was adapted from that published by Long et al.[112] A modification was made to avoid isolation of any small azide compounds, which are potentially explosive; bis-(2-azidoethyl)-disulphide was synthesised by the method of Zhang et al.[115] The reaction involves concatenation of alkyne-terminated quinone **3** to an azide-terminated disulphide linker via azide-alkyne Huisgen cycloaddition, a highly facile, high yield, copper catalysed conjugation strategy.[116] The resultant Q2NS was characterised by nuclear magnetic resonance (NMR) and high-performance liquid column-mass spectrometry (LC-MS). Full synthesis details are provided below.

[2,3-Dimethoxy-5-methyl-6-(2-propyn-1-ylamino)-2,5-cyclohexadiene-1,4-dione] **3.** To a stirred solution of 2,3-dimethoxy-5-methyl-p-benzoquinone **1** (1.82 g, 10 mmol, 2 equiv) in methanol (MeOH) (5 ml), a solution of propargylamine 2 (0.28 g, 5 mmol, 1 equiv) in MeOH (10 ml) was added dropwise over 10 min. The resulting solution was stirred at room temperature under atmospheric conditions for three hours, then diluted with water (50 ml) and extracted with ethyl acetate (3 x 5 ml). The combined organic layers were washed with brine (20 ml) and dried over $MgSO_4$. Flash column chromatography was used to isolate **3** as a purple solid (0.49 g, 2.1 mmol, 21%). ^{1}H NMR (400 MHz, CD_3OD) δ (ppm) 4.22 (2H, s) 4.02 (3H, s) 3.83 (3H, s) 2.72 (1H, t) 1.95 (3H, s)

Q2NS **6.** Concentrated HBr (45% wt, 15 ml) was added dropwise to concentrated H_2SO_4 (10 ml) at 0°C. To this mixture, bis-(2-hydroxyethyl) disulphide **4** (0.15 g, 1 mmol) was added dropwise. The reaction mixture was stirred for 24 hours at room temperature. Then, the reaction mixture was extracted with dichloromethane (3 x 5 ml). The combined organic layers were washed with water (3 x 20 ml), brine (20 ml), and dried over $MgSO_4$. The solution was concentrated in vacuo to give bis-(2-bromoethyl) disulphide **5** as a yellow oil (0.24g, 0.87 mmol, 87%). ^{1}H NMR (400 MHz, CDCl3) δ (ppm) 3.63 (4H, t) 3.12 (4H, t)

Without further purification, this oil was dissolved in dry dimethylformamide (DMF, 5 ml) under an atmosphere of dry nitrogen, followed by addition of sodium azide (0.28 g, 4.35 mmol, 5 equiv). The reaction mixture was stirred under reflux at 80 °C for 14 hours. Then, the reaction mixture was diluted with ultrapure water (50 ml) and extracted with diethyl ether (5 x 10 ml). The combined organic layers were washed with water (5 x 50 ml) to remove DMF, then washed with brine (20 ml) and dried over $MgSO_4$. DMSO (1 ml) was added before removing the diethyl ether in vacuo; this avoids isolating the potentially explosive bis-(2-azidoethyl) disulphide, the resulting solution of which was used without further purification. This solution was combined with a solution of 2,3-Dimethoxy-5-methyl-6-(2-propyn-1-ylamino)-2,5-cyclohexadiene-1,4-dione] **3** in DMSO (0.5 ml). Separately, a solution of copper (II) sulfate (8 mg, 0.05 mmol) and tris(benzyltriazolylmethyl)amine (TBTA; 26 mg, 0.05 mmol) in DMSO (0.5ml) was prepared and added to a solution of sodium ascorbate (0.4 g, 2 mmol) in ultrapure water (1 ml). The solutions were mixed, and the reaction mixture was stirred for 1 hour at room temperature. Then, the reaction mixture was diluted with ultrapure water (30 ml) and extracted with ethyl acetate (3 x 5 ml). The combined organic layers were washed with brine (20 ml), dried over $MgSO_4$, and concentrated in vacuo. Q2NS **6** was purified from the crude reaction mixture using mass-directed high-performance liquid chromatography (HPLC) to give Q2NS **6** as a purple solid (52 mg, 0.08 mmol, 10% from 5). ^{1}H NMR (400 MHz, CD_3OD) δ (ppm) 7.91 (2H, s) 4.63 (4H, t) 4.22 (4H, s) 4.04 (6H, s) 3.86 (6H, s) 3.18 (4H, t) 2.05 (6H, s). ^{13}C NMR (100 MHz, CD_3OD) δ (ppm) 182.6 (2C) 182.2 (2C) 147.6 (2C) 142.8 (2C) 142.1 (2C) 139.7 (2C) 124.1 (2C) 109.6 (2C) 61.8 (2C) 52.3 (2C) 38.4 (2C) 38.2 (2C) 10.6 (2C).

Post-synthesis, the Q2NS was dissolved in methanol and distributed into weighed glass vials, before the solvent was evaporated, leaving aliquots of 2-10 mg of Q2NS per vial. The vials were then stored in the dark at -80 °C. Full proton NMR spectra are shown in the appendix 9.1.
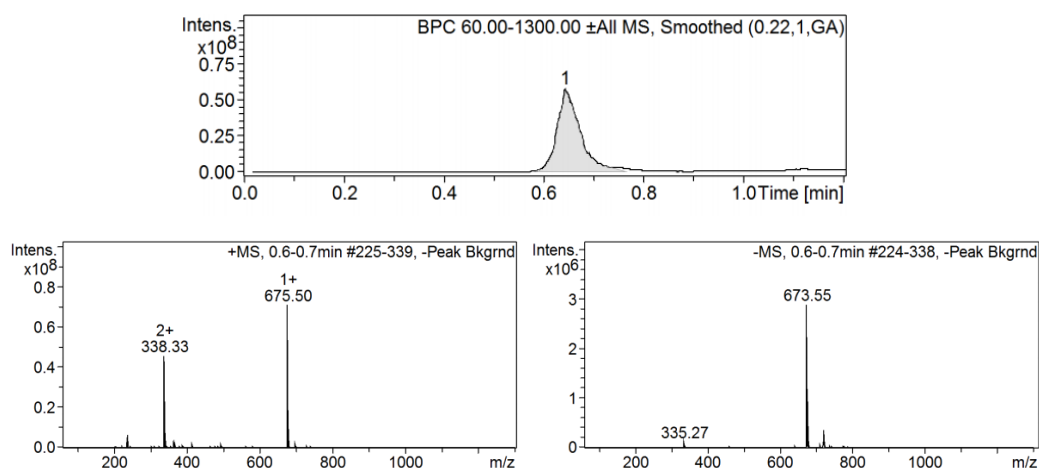
Figure 16. Top: LC-MS trace of purified Q2NS. The peak labelled "1" corresponds to the detection of ions as they are eluted from the column. Bottom: Positive (left) and negative (right) electrospray ionisation mass spectra of integrated peak "1". The peaks labelled "1+" and "2+" represent m/z of singly and doubly-protonated Q2NS.

2.3 Ligand Exchange Procedure

The disulphide group present in the structure of Q2NS makes it suitable for conjugation to CdTe/CdS core/shell QDs via formation of a thiolate complex to the QDs surface, after cleavage of the disulphide bond. Briefly, aliquots of Q2NS were dissolved in a small amount of DMSO (10-100 µl). The CdTe/CdS QD solution was degassed by sonication under vacuum, filtered, and stored in an oxygen-free glove box in 4 ml aliquots at a concentration of 1µM. A small amount (0.1-10 µl) of the Q2NS DMSO solution was added to each aliquot, and the solutions were left stirring in the dark, under N_2, overnight. The resultant conjugates were then cleaned twice via centrifugation after dilution with excess propan-2-ol, and resuspended in ultrapure water. Success of the ligand exchange was ascertained by measuring the absorbance spectrum of the supernatant after cleaning for traces of unbound Q2NS.

2.4 Optical Spectroscopy

Optical spectroscopy techniques are those which involve measuring the interactions between light and matter, including absorption, photoluminescent emission and reflection, and dependent on factors such as polarisation, wavelength, and intensity, among others. It is obvious, therefore, that optical spectroscopy techniques are critical for the characterisation of systems involving QDs. Ultra-fast spectroscopic techniques such as PL lifetime and transient absorption (TA) spectroscopy allow for precise interrogation of excited

state dynamics in optical systems, and time resolved spectroscopic techniques are useful for the measurement of their emergent properties, including photoluminescent quantum yield (PLQY) and absorption spectra.

2.4.1 Steady State Photoluminescence Spectroscopy

Photoluminescence (PL) or fluorescence spectroscopy is the measurement of the properties of photoluminescent emission, and the excitation that leads to this emission. This is distinct from being a measurement of excitation in general. In a typical steady state PL spectroscopy experiment, a sample in a quartz or plastic cuvette is continuously illuminated with a collimated beam of unpolarised light, with wavelength controlled by a monochromator. A separate monochromator is used to collect the light that is emitted from the illuminated sample. To account for fluctuations in the intensity of the excitation, as well as wavelength-dependent intensity in an imperfect light source, a reference signal is also measured directly from the excitation.

PL scans can be obtained in two domains:

1) PL emission spectroscopy, where the excitation wavelength is kept constant, and the emission intensity of the sample as a function of wavelength is recorded. The resulting spectrum is known as the emission spectrum.

2) PL excitation spectroscopy, where the emission monochromator is maintained to measure the emission intensity at a fixed wavelength, while the excitation wavelength is varied (holding the intensity at a fixed value). The spectrum maintained is known as the excitation spectrum of the sample.

These scanning regimes can be combined to obtain 2D spectra of excitation vs emission. PL spectra were acquired for this work on an Edinburgh Instruments FLS 980 spectrometer with double excitation and emission monochromators. Constant temperature was maintained and controlled using a liquid Peltier cooler/resistance heater system.
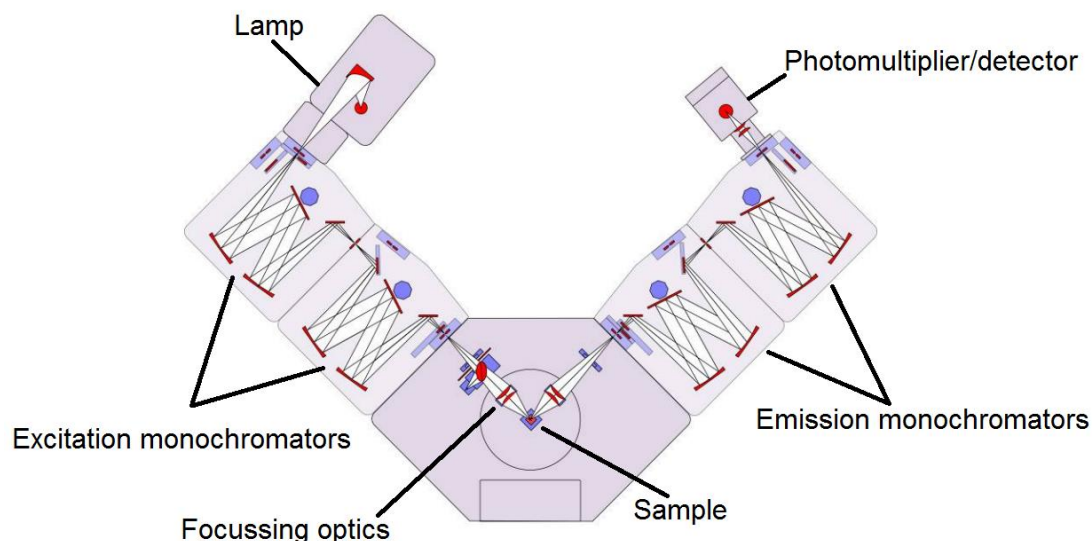
Figure 17. Schematic of Edinburgh Instruments FLS 980 spectrometer system, in steady state PL mode. Excitation of the sample is achieved using a doubly monochromated halogen light source. Emission is measured by monochromators leading to a switchable PMT-900 photomultiplier detector. Image adapted from Edinburgh Instruments FLS 980 manual.

2.4.2 PLQY Determination with Integrating Sphere

For a photoluminescent sample, the photoluminescent quantum yield (PLQY), is defined as the number of photons emitted via photoluminescence as a proportion of the number of photons absorbed, and is usually expressed as a percentage. Depending on the QD type, and the presence, or otherwise, of non-radiative recombination paths, values of PLQY for QDs can range from ~4% to almost unity.[39, 117] In order to accurately evaluate the PLQY for a particular sample, it is important to be able to accurately measure both the absorption of photons by a sample as well as emission.

An integrating sphere consists of a hollow spherical cavity, with all internal surfaces coloured in a reflective, diffuse, white coating. Small ports in the sphere allow light to be directed into and collected from the sphere. The sample that is to be investigated is placed within the sphere, in a non-absorbing cuvette or holder. Any light that enters the sphere will be scattered in a diffuse fashion around the inside of the sphere, preserving intensity but destroying any spatial information; the light within a sphere of sufficiently high quality will be of roughly equal intensity at all points within the sphere. Entry and exit ports are separated by a baffle, to prevent light immediately exiting the sphere without being diffused. In order to measure PLQY of a photoluminescent sample, light of a wavelength sufficient to excite the sample is directed into the sphere, and is collected, along with the light

subsequently emitted by the sample, at the exit port. The proportion of light absorbed by the sample can be ascertained by comparing intensities of the relevant wavelength at the exit port of the sphere, with and without the sample present. The number of photons absorbed is calculated by considering the frequency-energy relation $E = h\nu$. This is compared to the number emitted by the sample, collected at the exit port to obtain the PLQY.

Spectra were recorded for QDs dispersed in ultra-pure water and chloroform in sealed quartz cuvettes, using the aforementioned Edinburgh Instruments FLS 980 with integrating sphere attachment. PLQY was calculated from these spectra using FL980 software.
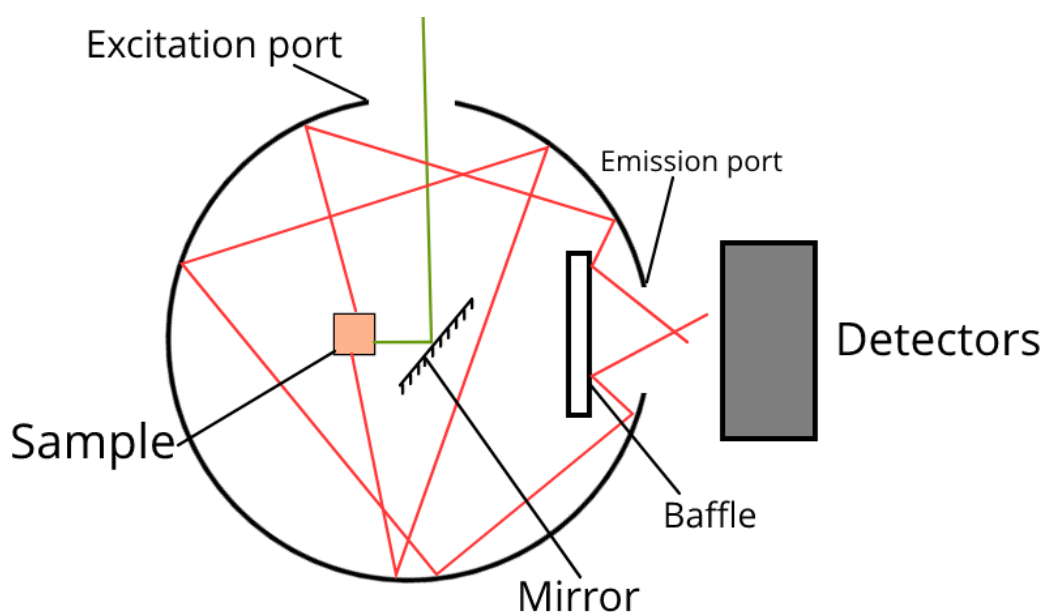
Figure 18. Principle of operation of integrating sphere, for PLQY determination. Light emitted from the sample (red) as well excitation light that is not absorbed is reflected an arbitrary number of times within the volume of the sphere, before collection at the exit port.

2.4.3   UV-Vis-NIR

Ultra-violet/visible/near-Infra-red (UV-Vis-NIR) absorption spectroscopy describes steady-state techniques used to measure how a given sample absorbs light as a function of wavelength. Many electronic transitions in QDs have energies in this range of the electromagnetic spectrum, so UV-Vis-NIR spectroscopy is ideal for interrogating the optoelectronic properties of QDs. Distinctly from PL excitation spectroscopy, UV-vis-NIR spectroscopy measures absorption by all excitation events, not only those that eventually result in radiative recombination. Importantly, a colloidal QD sample's absorbance is

proportional to its concentration; if the molar extinction coefficient is known, then the molar concentration of a given sample of QDs can be ascertained via the Beer-Lambert law:

$$A = \varepsilon(\lambda)CL. \tag{25}$$

Here, A is the absorbance, C is the molar concentration, L is the path length of the light through the sample and ε(λ) is the wavelength-dependent molar extinction coefficient. The molar extinction coefficient of a particular QD type is both size and material dependent, and can be estimated from features of both PL and UV-Vis-NIR absorbance spectra.[40, 118]

Within a UV-Vis-NIR spectrometer, a beam of light of controlled wavelength divided in two by a beam splitter, with each part of the divided beam heading through a separate, identical cuvette, before the intensity is measured by photodetectors. Typically, only one cuvette contains the sample of interest; the other contains a "blank" which is the solvent or dispersal medium in which the sample of interest is dissolved or dispersed. If the path length of the beam through the cuvettes is known, the absorbance of the sample can be calculated by noting the difference in intensity between the intensity of the beam that has passed through the sample, and that which has passed through the blank. The subtraction can also be performed with a single beam by measuring the absorbance of the blank and then the sample (or vice versa) but this does not account for fluctuations in the intensity of the lamp light. An absorbance spectrum is generated by varying the wavelength of the light using a monochromator, and measuring the absorbance as a function of the wavelength. UV-Vis-NIR spectra were obtained using an Agilent Technologies Cary Series UV-Vis-NIR spectrophotometer.
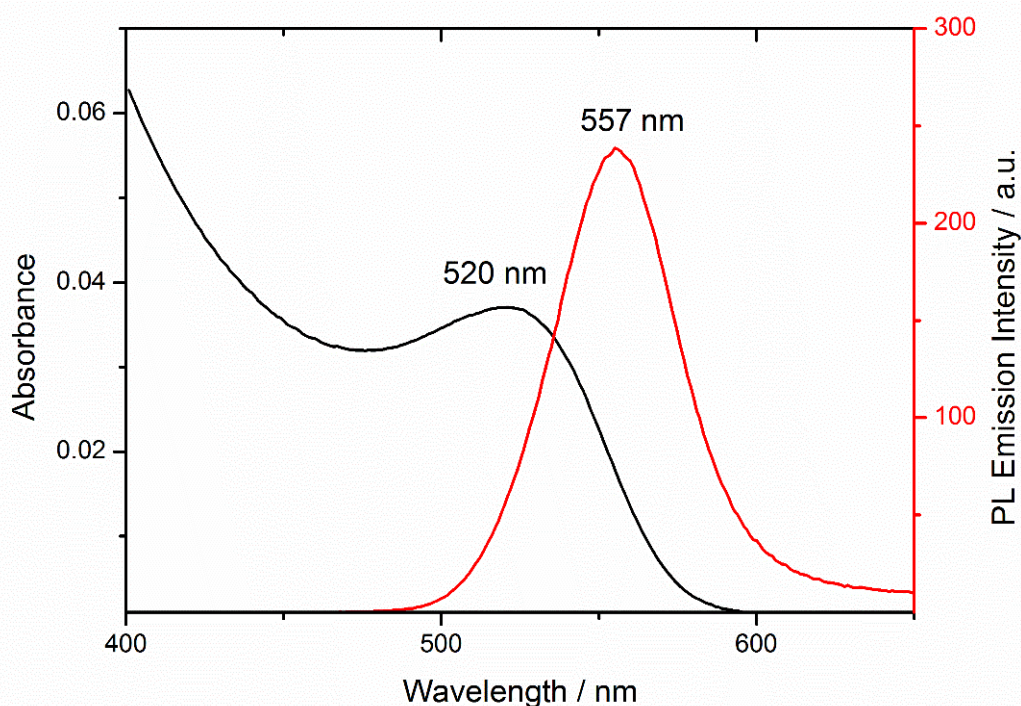
Figure 19. Example UV-Vis (black) and PL emission (red) spectra for a typical sample of CdTe/CdS core/shell QDs. The first excitonic transition is visible in the UV-Vis spectrum at 520 nm, and the emission wavelength of the sample is at 557 nm.

2.4.4   PL Lifetime

The advent of highly-controllable pulsed laser sources, as well as highly sensitive, time-accurate photomultipliers has allowed for the development of useful time-resolved PL spectroscopy/ fluorescence lifetime spectroscopy. A typical lifetime experiment works on the principle of time-correlated single photon counting (TCSPC); the sample (in a cuvette) is illuminated with a short (~100 ps) pulse from a laser of relevant wavelength, resulting in excitation of the sample. The time between the pulse and the first detection of an emitted photon is then recorded, via photomultiplier and fast electronics, for a very large number of pulses, and plotted on a histogram. The experiment is stopped when the largest histogram bin reaches a sufficient, user defined value; when enough data is recorded, the frequency density of each histogram bin is proportional to the probability of detecting the first photon at the corresponding time after excitation. Immediately after photoexcitation, the maximum number of fluorophores (in this case QDs) are in the excited state, and so the probability of emission is at a maximum. After a certain amount of time, some excited states have depopulated, and so the probability decreases. The resulting plot is the emission intensity as a function of time after excitation, usually described by a sum of exponential decays:

$$I = A_0 + \sum_i A_i e^{-\frac{t}{\tau_i}}$$

(26)

Here, A_0 is a constant which considers decay timescales longer than those measured in the experiment, τ_i are the time constants and A_i are the associated amplitudes. This contains a wealth of information about the excited state dynamics of the photoluminescent system; the time constant of the dominant process is known as the PL lifetime, and is the characteristic timescale that describes excited states that can lead to radiative recombination. In simple cases, it is possible to identify individual recombination processes or mechanisms by the assignment of different time constants, however in QDs, excited state dynamics are complex, and due to factors including size polydispersity, any given ensemble of QDs may have an arbitrarily large number of recombination processes.
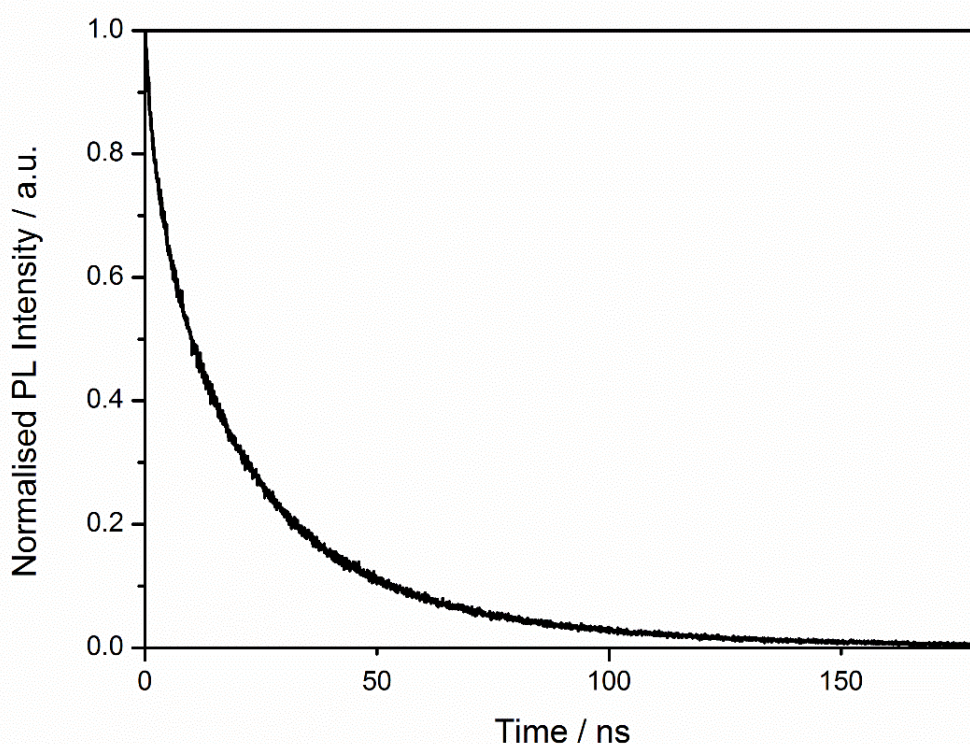
Figure 20. Typical transient PL trace for a sample of CdTe/CdS QDs. Immediately after excitation, PL intensity is at maximum. PL intensity decays with a multi-exponential time dependence as excited states are depopulated.

In this work, transient PL spectra were obtained for CdTe/CdS QDs and CdTe/CdS-Q2NS conjugates using the aforementioned Edinburgh Instruments FLS 980. Typically, samples were prepared in ultra-pure water at 0.01-2 µM and sealed in a quartz cuvette under a

protective N_2 atmosphere. Excitation was achieved with an Edinburgh Instruments EPL 475 diode laser emitting at 472.8 nm, with average pulse width of 79.5 ps. The pulse period was set to 200 ns and the average power incident on the sample was approximately 2 mW. TCSPC was performed on photons emitted at the PL peak, and the resulting data was analysed using Edinburgh Instruments PL980 software. The instrument response function (IRF) was obtained by measuring scattering from a dilute solution of milk and subtracted from obtained traces.

2.4.5   Transient Absorption Spectroscopy

The Pauli Exclusion Principle states that no two fermions can ever simultaneously occupy the same quantum state. In QDs, this means that no two electrons or holes can inhabit the same excited state at once; a QD that has been excited into the minimum-energy excited state will therefore be unable to absorb a photon whose energy corresponds to this transition. For an ensemble of similar QDs, the result of this is that a short time after excitation, the absorbance that corresponds to the minimum energy transition is decreased, as the population of electrons at the CBM is increased. As the CBM population decreases, through radiative recombination, or otherwise, the absorbance recovers.

For QDs, transient absorption spectroscopy allows insight into excited state dynamics of QDs, typically with finer time-resolution than PL lifetime spectroscopy. TA experiments have another advantage over transient PL experiments, in that they are not only sensitive to electronic states which can result in radiative recombination. In a typical experiment, a sample of QDs is excited by a short pulse of light with photon energy sufficient to achieve excitation of electrons to an energy state higher than the CBM. This is known as the "pump" pulse. A short time later, a "probe" pulse of a specified wavelength is incident on the sample, and the absorption of this pulse by the sample is recorded. When the probe pulse corresponds to the minimum-energy transition, a characteristic behaviour is observed; absorbance quickly decreases after the "pump" pulse as electrons cool to the CBM. This is termed a "bleach" as states are no longer accessible. As these electrons recombine with holes, radiatively or otherwise, or are extracted from the QD, the absorbance recovers, due to the depopulation of the minimum energy electron state. Similarly to PL lifetime spectroscopy, this recovery can be fitted with a multi-exponential function, and time constants can be ascribed to specific processes that lead to depopulation of the minimum energy state. In this mode, TA spectroscopy is typically considered to be sensitive only to the

electron population at the CBM, as the cooling of holes to the VBM is much faster and cannot be resolved by current instrumentation.
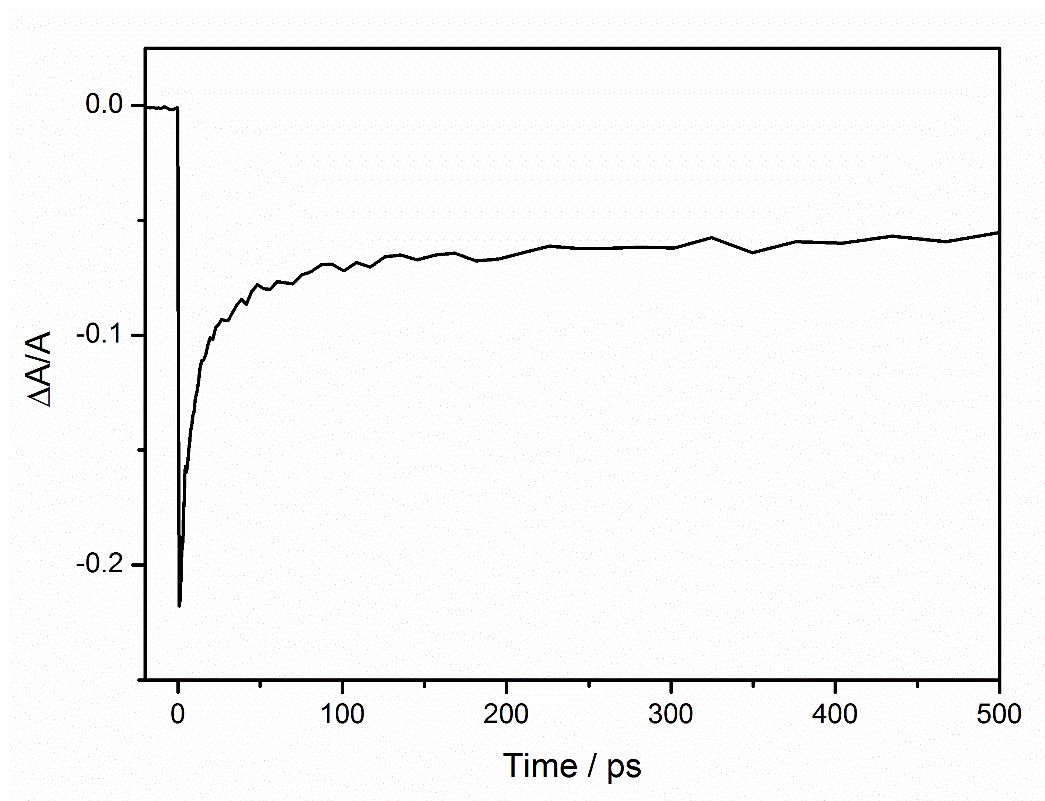
Figure 21. Typical absorption transient. Fractional absorbance by CdTe/CdS QDs at a wavelength consistent with the first excitation in QDs is plotted as a function of time after application of a "pump" pulse. Soon after excitation (1-2 ps) absorbance decreases, as electrons arrive at the CBM, having cooled from hot states. The subsequent multi-exponential decay is due to depopulation of the CBM due to recombination processes.

It is also possible to perform wavelength-resolved TA experiments, where the absorption at a fixed time point after the pump pulse is measured as a function of wavelength, allowing for time-resolved probing of states at varying energy levels after excitation. It is typical to choose a time point soon after excitation, where carrier population at the CBM is maximised. Such a plot of the pump-induced absorbance change is termed a TA spectrum, or bleach spectrum, and allows assessment of the degree of bleaching of states involved in radiative recombination. The time point at which bleach spectra are obtained can be varied to produce a 2-D spectrum.
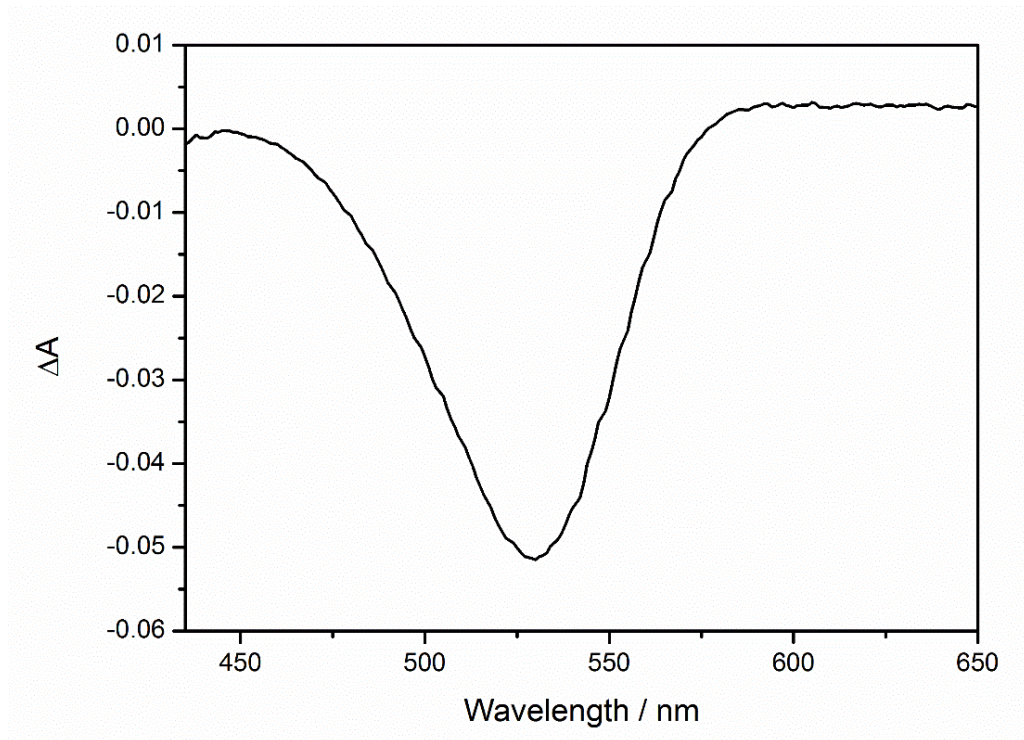
Figure 22. Typical pump-induced absorbance change for the sample of QDs from figure 21. A short time after application of the pump pulse, absorption decreases as conduction band states are filled. The decrease in absorbance is greatest at approximately 530 nm, a wavelength that corresponds to the band edge excitation.
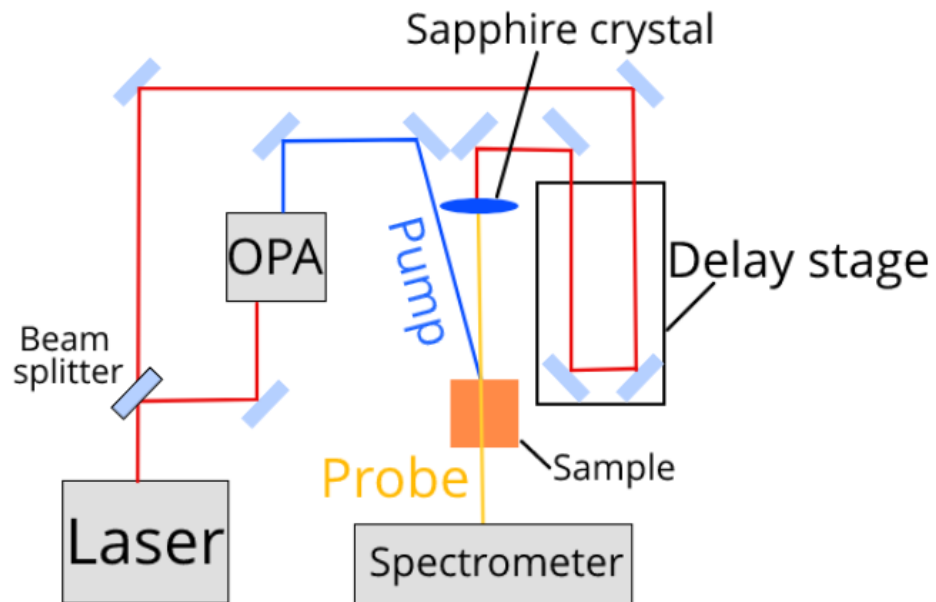
Figure 23. Simplified schematic of TA spectroscopy setup. Control of time delay between pump and probe is achieved using a time-of-flight delay stage.

TA spectroscopy experiments were performed on CdTe/CdS QDs and CdTe/CdS-Q2NS conjugates. A Ti:sapphire laser was used to pump a Topas Prime optical parametric amplifier (OPA) to achieve pump pulses at 420, 450 and 480 nm (~10 nm full width at half-maximum, 100 fs, 250 nJ). The rest of the OPA output was passed through a sapphire crystal to generate a white light continuum which was used as the probe to record changes in absorption between 435 nm and 720 nm. Ultrafast broadband transient absorption measurements were carried out at randomly ordered time points in a Helios (Ultrafast Systems LLC) spectrometer (-20 ps to 3 ns, ~0.2 ps resolution). The samples were magnetically stirred to avoid photocharging effects during the measurements and low pump fluences were used to decrease the probability of multi-photon absorption. The experimental setup is illustrated in figure 23.

2.5   X-ray Crystallography

The wavelengths of x-rays are similar to inter-atomic distances in ionic crystals. X-rays incident on a crystal are can reflect from atomic nuclei. Bragg's law describes the condition of constructive interference of the reflected radiation from a crystal with lattice spacing d:

$$n\lambda = 2d \sin\theta. \qquad (\,27\,)$$

Here, λ is the wavelength of the incident x-rays, θ is the angle of incidence and n is the order of the interference peaks, an integer. For a known wavelength and controlled angle, it is therefore possible to determine the crystal lattice spacing in a given sample. A sample of QDs dried onto a substrate can be considered a powder, with a random and isotropic distribution of lattice orientations. As the number of QDs is large, it can be assumed that a significant number of lattices are orientated appropriately for acquisition of a diffraction spectrum; however to avoid the effects of potential anisotropic structure, the sample can be slowly rotated to sample all orientations.

Diffraction peaks obtained from nanoparticle samples are subject to broadening that is dependent on the particle size, described by the Scherrer equation:

$$a = \frac{\kappa\lambda}{\beta \cos\theta} \qquad (\,28\,)$$

Here, a is the nanoparticle size, β is the peak width, and κ is a unitless factor that accounts for the shape of the nanoparticle, which usually takes a value of about 0.9.[119] For roughly

monodisperse, monocrystalline QDs, the average size can therefore be estimated from x-ray diffraction spectra.

X-ray spectra for this work were obtained for $CuInS_2$ QDs using a P'Analytical X'Pert MPD Bragg-Brentano diffractometer, with a Cu $k\alpha_1/k\alpha_2$ radiation source (λ=0.15418 nm). Samples were prepared by repeatedly drop-casting solutions of QDs dispersed in chloroform onto a silicon zero-diffraction plate, and waiting for the solvent to evaporate, leaving a dry powder. Angle scans for values of 2θ from 15°-60° were performed over approximately 25 minutes with a 0.05° step size. Obtained spectra were compared with International Centre for Diffraction Data (ICDD) database values for chalcopyrite $CuInS_2$.

2.6   X-ray Photoelectron Spectroscopy

The energy of x-ray photons is of the same order of magnitude as the energy by which electrons are electrostatically bound to atomic nuclei in many materials. The specific value of this binding energy will depend on the identity and chemical state of the element in question. X-ray photoelectron spectroscopy allows identification, quantification and characterisation of elements in a sample by determination of the binding energies of the electrons within a sample.

An x-ray of energy hν incident on a sample has the chance to eject an electron; the kinetic energy of this ejected electron E_k can be related to the binding energy of the initial state E_b as follows:

$$E_b = h\nu - (\varphi + E_k). \tag{29}$$

In this expression, $\varphi = E_{vac} - E_F$ is the work function of the material, where E_{vac} is the vacuum level, and E_F is the Fermi energy. If the energy of incoming photons is accurately known, measurement of the energy of emitted electrons therefore allows for calculation of the binding energies of electrons within the sample. Auger processes also result in emission of electrons. Here, energy from higher-level valence electron moving into a vacated state is transferred to another electron, which is subsequently ejected. The energies of photoelectrons and Auger electrons alike can be compared with database values for identification of elements present in a sample; these elements can be quantified by application of appropriate sensitivity factors to measured photoelectron peaks.

In this work, samples of QDs were prepared by drop casting QDs onto a template-stripped gold surface, before evaporation of the solvent. X-ray photoelectron spectra were obtained for Cd, Te, Cu, In, S, and C overnight, depending on the QD type. The positions of

photoelectron peaks were calibrated to the position of the C1s peak. Peaks were fitted and used for determination of particle stoichiometry using Thermo Scientific Avantage software using Scofields relative sensitivity factors. Emission of electrons from a sample can result in a build-up of positive charge, particularly for samples consisting of a large amount of non-conductive organic matter; this can result in skewing of acquired peaks. To avoid this, an electron-emitting "flood gun" was incident on the sample during data acquisition.

2.7   Electron Microscopy

The Abbe limit provides an estimation for the diffraction limited best resolution for an optical microscope:

$$d = \frac{\lambda}{2n \sin \theta} \qquad\qquad (\,30\,)$$

In this expression, d is the minimum resolvable distance, λ is the wavelength of the light, and $n \sin \theta$ is the numerical aperture of the lens, where n is the refractive index of the medium, and θ is half the convergence angle of the focus of the lens. For visible light (λ ~ 550 nm), and realistic values of the numerical aperture (~0.9) the maximum achievable resolution will be approximately 250 nm. Clearly, this is insufficient for the study of the structure of most nanomaterials.

Wave-particle duality is one of the central principles of the theory of quantum mechanics. For a massive particle, such as an electron, with momentum p, the de Broglie wavelength can be defined:

$$\lambda = \frac{h}{p} \qquad\qquad (\,31\,)$$

Electron microscopic techniques are those which use electrons to illuminate the sample. The wavelength, and therefore the diffraction limit, depends on the momentum of the electrons in the imaging beam, but the most powerful electron microscopic techniques (such as Scanning Transmission Electron Microscopy, or STEM) now achieve resolutions up to 50 pm (0.5 Å), less than an atomic radius. These techniques therefore allow imaging of the atomic structure of nanomaterials.

2.7.1   Sample Preparation for Electron Microscopy

For imaging of crystal structures, it is necessary to have a substrate material that has no crystallinity itself. For this reason, amorphous carbon substrates are commonly used; the crystal structure of the QDs can be resolved against the amorphous, isotropic background. For this work, ultrathin amorphous holey carbon on gold grids were used for imaging of QDs;

the grids consist of a gold mesh with 50 μm pitch coated with an ultra-thin layer of amorphous carbon of varying thickness. Gold was chosen over more common copper to prevent background contributions during elemental analysis of copper-containing $CuInS_2$ QDs. Samples were prepared by drop-casting 1-5 μM QD dispersions in chloroform or ultra-pure water onto the TEM grids, and wicking away excess solvent using filter paper. For QDs in aqueous dispersions, the grids were subsequently cleaned under argon plasma for 10 seconds to remove any unwanted organic material, which can cause accumulation of charge at the surface. For $CuInS_2$ and $CuInS_2$/ZnS QDs in chloroform, the grids were also cleaned under argon plasma, and stored in an oxygen-free glove box. QDs prepared for the scanning transmission electron microscopy (STEM) and electron energy loss spectroscopy (EELS) experiments were additionally baked overnight, under vacuum at 100 °C to further remove organic material.

For imaging of QDs within cells, cells were fixed as described in section 2.8 and embedded in epoxy. 100 nm sections were then cut using a microtome, which were mounted on the sample grid.

2.7.2   Bright-Field Transmission Electron Microscopy

Transmission electron microscopy (TEM) is one of the two major modes of electron microscopy, along with scanning electron microscopy. In the TEM experiments described here, electrons are accelerated across a specified potential, and focussed to a tight beam a pair of condenser lenses. The beam then passes through an aperture, and is then incident on the sample. Electrons are either absorbed by the sample, are scattered by reflection from atomic nuclei, or are transmitted straight through. At high magnifications, the contrast is obtained mostly due to scattering, and atomic nuclei therefore appear dark. An image of the sample is obtained by collecting the transmitted electrons using a further aperture and pair of lenses, directing them onto a charge-coupled-device (CCD) detector. The TEM is kept evacuated to a low pressure (10^{-5} - 10^{-4} Pa) to avoid collisions between electrons and air molecules. In this work, images of QD samples prepared as described above were obtained using a FEI Titan3 Themis G2 TEM fitted with 4 EDX silicon drift detectors. The electron accelerating voltage was 300 kV, and images were acquired using a Gatan One-View CCD.

2.7.3   High-Angle Annular Dark Field STEM

Scanning transmission electron microscopy (STEM) involves raster-scanning of a finely-focussed beam of electrons over the sample, building up an image pixel-by-pixel. This is opposed to standard TEM where the entire sample is illuminated with electrons, and

interference effects between electrons can cause losses in fidelity. High-angle annular dark field (HAADF) STEM describes an image acquisition strategy where electrons that are scattered from the sample at a sufficient angle are detected by an annular array of detectors. The acquired image is therefore in the opposite contrast to bright-field TEM; scattering centres show up brighter than the surroundings. HAADF techniques necessitate the use of STEM, as opposed to standard TEM, as electrons can be scattered in any direction. HAADF-STEM images were acquired for this work on a Nion UltraSTEM instrument, with hardware aberration correction.

2.7.4 Electron Energy Loss Spectroscopy

High quality STEM images are achieved using a beam of electrons with narrow energy distribution. There are a number of ways that these electrons can scatter inelastically from a sample of interest, including ionisation processes, excitation of inter-band transitions, and electron-plasmon interactions. In any case, as long as the energy distribution of the electron beam is narrow, the energy loss associated with any of these scattering processes can be measured. Similarly to XPS, the energies associated with ionisations by removal of strongly bound "core" electrons are element-specific; it is therefore possible to identify, and quantify the elemental composition of a material by detection of electrons of energy loss consistent with these specific transitions.

Electron energy loss spectroscopy (EELS) involves measurement of the energies of these scattered electrons. If the initial energy of each electron in the beam is precisely known, then energy losses can be determined, and associated with a particular mechanism. It is a techniques which is highly complementary to TEM, particularly in a scanning mode (STEM) due to the requirement of both for a highly controllable monochromatic electron beam. Combination with a STEM system also allow spatially resolved EELS to be performed (STEM-EELS).

Particularly for $CuInS_2$ and $CuInS_2/ZnS$ QDs, features of spatially resolved EELS spectra are often very weak due factors determined by the thinness of the sample.[120] However, the QDs exhibit a large peak associated with plasmonic excitation, as well as resolvable and quantifiable edges consistent with core-loss ionisation of Cu, In and S, as illustrated and described in figure 24.
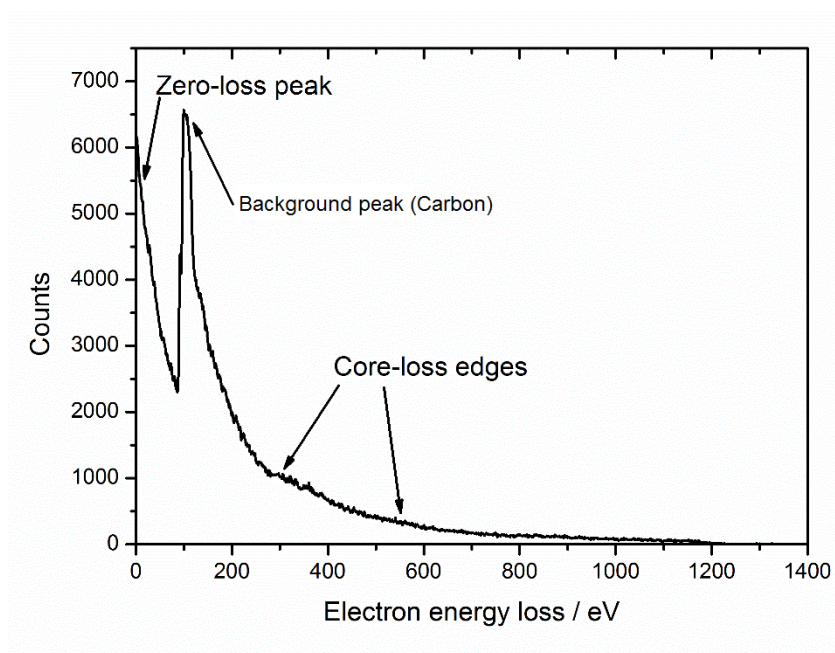
Figure 24. Example EEL spectrum for QDs. A large number of electrons are not subjected to inelastic scattering, giving rise to the zero loss peak. The background peak is due to the amorphous carbon film on the sample grid. Energy losses from ionisation of atoms by emission of "core" electrons result in "edges" in the fine structure of the decay at high electron energy losses; it is these core loss edges that are analysed to determine elemental composition.

For this work, EELS was used in an imaging mode on $CuInS_2$ and $CuInS_2/ZnS$ QDs. During acquisition of a HAADF-STEM image of single QDs, EEL spectra were recorded, and stored so that each pixel had a corresponding EEL spectrum. For each spectrum, Cu and In edges were located, and after subtraction of the background signal using a power-law fit immediately prior to the relevant edge, the intensities were extracted to produce maps showing the spatial distribution of these elements. These measurements were performed on the Nion UltraSTEM microscope in parallel with HAADF-STEM measurements. Each EELS "map" took between 7-15 minutes to acquire. An accelerating voltage of 60 kV was used.

2.8   Live Cell Experiments

2.8.1   Cell culture

MCF-7 cells were obtained from the European Collection of Authenticated Cell Cultures (ECACC) as frozen stock, and subsequently cultured in 75 cm^2 flasks in Dulbecco's Modified Eagle Medium (DMEM, Sigma) with 10% foetal bovine serum (FBS, Sigma), and 20 mM GlutaMAX (Sigma). Cells were stored in a moisture-controlled incubator at 37 °C with a 5%

CO_2 atmosphere. The adherent MCF-7 cells were subcultured every 3-4 days. This was achieved by washing with Dulbecco's phosphate buffered saline (DPBS), before submersion in TrypLE dissociation reagent. One fifth of the resulting cell suspension was then diluted in growth media, then transferred to a new flask. Passage numbers for all cells used in experiments were less than 20.

Most experiments were performed on cells plated on 96-well plates. During subculture, the number concentration of cells was counted using a haemocytometer. The cell suspension was then diluted with the relevant medium to a concentration of $5x10^4$ cells/ml. Each well on the 96-well plate was then inoculated with 100 µl of the diluted suspension, in order to achieve 5000 cells per well. The plates were then incubated overnight to allow the cells to adhere to the surface.

2.8.2 Toxicity studies

Cell viability was measured using CCK-8 (Cell counting kit 8, Sigma), a colourimetric assay. CCK-8 consists of a water-soluble tetrazolium salt (2-(2-methoxy-4-nitrophenyl)-3-(4-nitrophenyl)-5-(2,4-disulfophenyl)-2H-tetrazolium, monosodium salt, or WST) in buffered aqueous solution. In the presence of live cells, WST is reduced to an orange-coloured, water-soluble formazan dye, with absorption maximum at 450 nm. The rate of production of the reduced dye is proportional to the number of metabolically active cells present in the solution, as well as their rate of metabolism. It is therefore possible to measure cell viability, by measuring the absorption due to the presence of reduced dye a fixed time after introduction to the cells.[121]

MCF-7 cells were plated in 96-well plates at a confluency of 5000 cells per well, and incubated overnight. QDs were sterilised before addition to the cells by passing them through a 0.22 µm Acrodisc syringe filter. QD dispersions in DMEM were prepared and added to the cells, with QD concentrations ranging from 0.1-100 nM, so that the total volume in each well was 100µl. A control was also prepared without QDs. The cells were then incubated for 24-48 hours in the presence of the QDs. After the chosen incubation time, 10 µl CCK-8 solution was added to each well, and the plate was further incubated for 2 hours. The absorbance at 450 nm (concurrent with the absorption maximum of the formazan dye) was then measured using a plate reader. Viability of cells was calculated, for each QD concentration, by measuring the absorbance at 450 nm in each well containing QDs, normalised to control. The absorption due to the QDs was accounted for by subtracting absorbance of wells containing QDs but no CCK-8.
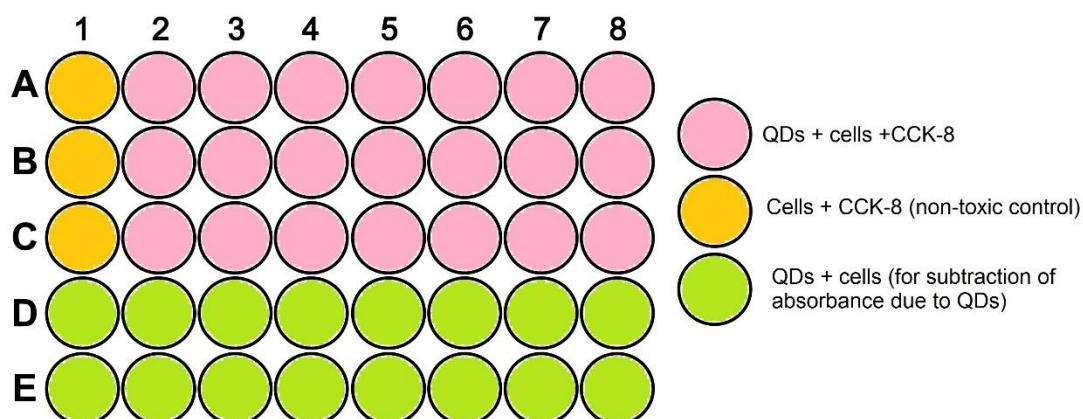
Figure 25. Format of well plate for toxicity experiments. All wells contained 5000 cells in 100 µL culture media. Pink wells represent wells where cells were incubated with QDs and CCK-8 (n=3 for each of 7 concentrations). Orange wells represent a negative control (no QDs). Green wells contained the relevant amount of QD solution but no CCK-8.

2.8.3   Non-directed Endocytic Uptake of QDs

Endocytic uptake of QDs by MCF-7 cells was investigated. Typically, cells were plated at 5000 cells/well in a 96-well plate and incubated overnight, as described above. In a similar fashion to the toxicity studies, sterile QD dispersions in 100 µl of the appropriate medium were prepared, with concentrations ranging from 0.1-50 nM, and added to the cells. The plates were then returned to the incubator. In some cases, the cells were incubated within a fluorescence plate imager (BioTek Cytation 5) and continuously imaged (details of imaging protocols are in section 2.9). After a fixed time point, typically 1-48 hours after addition of the QDs, the QD-containing medium was removed, and the cells were washed with DPBS before medium not containing QDs was re-added. The resulting plated cells were then imaged as described in section 2.9.

2.8.4   Use of Cell-Penetrating Peptides

TAT is a protein within human immunodeficiency virus (HIV) that is responsible for transduction of the virus into the cell. The peptide sequence TAT-c (sequence CGRKKRRQRRR) consists of amino acid residues 48-57 of HIV TAT, and is known for its ability to facilitate transfection of material into cells; it is therefore termed a cell-penetrating peptide (CPP). [122, 123] An important feature is the thiol-containing cysteine residue at the n-terminus, which allows binding to the surfaces of QDs.

To prepare the TAT-c conjugated QDs, 10 mg TAT-c (provided by Dr. Masayoshi Tanaka, Tokyo Institute of Technology) was dissolved in 50 µl DMSO. Dispersions of TGA-stabilised

CdTe/CdS QDs in ultra-pure water were prepared at concentrations of 1μM and volumes 1-2 ml. A sufficient volume of the TAT-c DMSO solution was then added to the QDs to achieve an average TAT-c:QD ratio of 10:1. The dispersions were then gently mixed overnight, in the dark, using a tube rotator. The QDs were the cleaned by centrifugation as described in section 2.1.4. Success of the conjugation was ascertained by measuring the absorbance spectra of the solutions before and after cleaning, and comparing with that of an equivalent solution of TAT-c. The resulting QDs were then used in QD uptake experiments using the same protocols described in section 2.8.3.

2.8.5 Cell Squeezing

Developments in on-chip microfluidic systems in recent years allow for precise manipulation of very small volumes of liquid (such as cell suspensions in media) in a sterile environment. Recently, it has been shown that cells which are rapidly mechanically deformed form transient pores in the membrane; this allows for diffusion of molecules or nanomaterials into the cell interior.[124] An advantage of this is that endocytosis is avoided; delivered nanomaterials end up in the cell cytosol.

Cell squeezing experiments were performed using a cross-flow deformation scheme, illustrated in figure 26. Briefly, opposing microfluidic channels direct the cell suspension at a predetermined flow rate to a stagnation point, where shear forces deform the cells to a degree determined by the flow rate. Cells were suspended in running buffer (DPBS with 0.5% methyl cellulose, viscosity ~39 mPas). QDs were sterilised using a 0.2μm Acrodisc 25mm syringe filter. QDs were added to the cell suspension at a final concentration of 100 nM, before passing through a cell strainer (40μm pore size, Fisher Scientific Ltd) to remove aggregated cells. The solution was then loaded into a sterile syringe and injected into the cross-flow device by a syringe pump at a flow rate of 100 μl/min. The deformation of the cells was recorded with high speed camera mounted on an inverted microscope (Nikon Eclipse Ti). The cells were collected and incubated for 15 mins at room temperature. The cells were then washed with DPBS to remove excess QDs. Control cells were incubated and treated in the same manner (forgoing deformation) for the same duration of time (~30 mins).
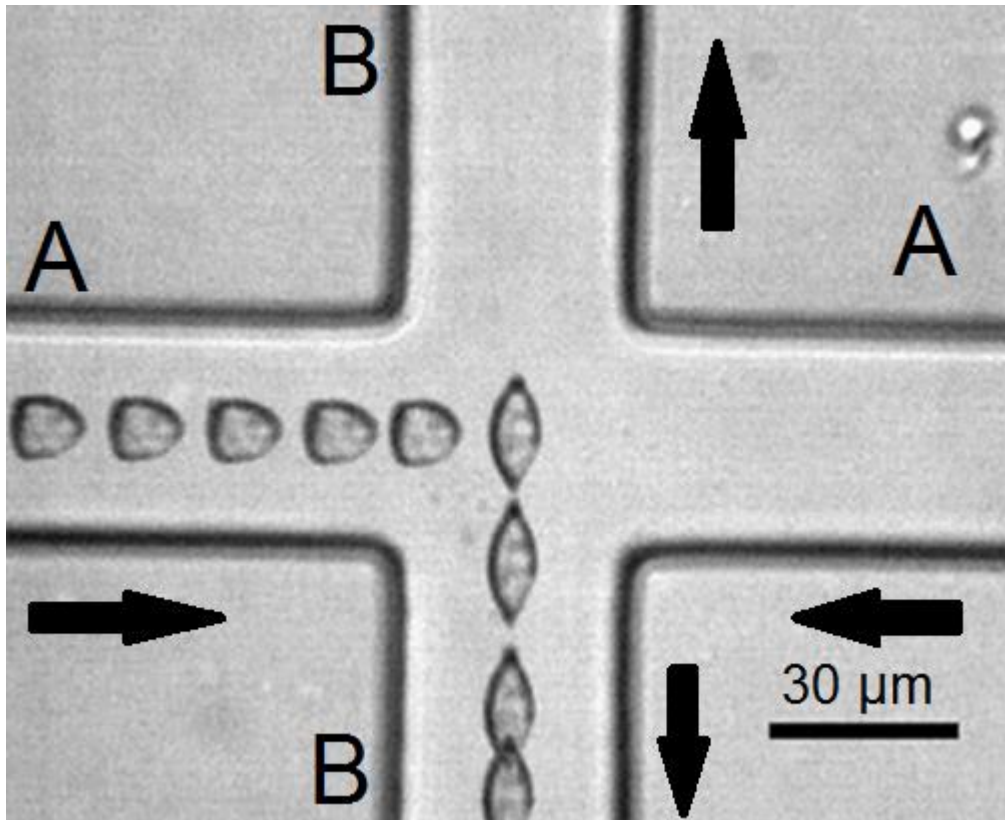
Figure 26. Light microscope image stack of cell squeezing apparatus. A suspension of cells is flowed into the device through opposing channels (A) before meeting at a stagnation point, where cells are deformed by shear forces, before exiting the chip (B). Image courtesy of Fern Armistead.

The cells with QDs were suspended in 200 µl culture media in 8 well cover-glass incubation chambers. The chamber was mounted on confocal microscope, (DMi8 Leica) for fluorescence and bright field imaging of the cells. The images were analysed and intensity of the fluorescence from each cell was measured using ImageJ.

2.8.6   Immunostaining

Immunostaining describes biological techniques that use antibodies to label proteins through specific antibody-protein interactions. Antibodies are large, y-shaped proteins that recognise other, particular proteins (such as those of a virus causing an infection, known as antigens) and bind to them, as part of the immune response. In this work, the goat derived antibody anti-EEA-1 was used to label early endosomes within MCF-7 cells, as early endosomes are associated with the protein early endosome antigen-1 (EEA-1), the antigen to anti-EEA-1. A mouse-derived fluorescent antibody that binds to goat anti-EEA-1 is then added, in order to fluorescently label the endosomes, an example of indirect

immunostaining. Simultaneous fluorescent imaging of these labelled endosomes, as well as QDs allows the degree of co-localisation to be established; strong co-localisation of QDs and endosomes suggests that QDs are mostly within endosomes, and that uptake of QDs has been dominated by endocytic processes.

In a typical experiment, QD-containing cells (as prepared in 96-well plates, by protocols detailed in sections 2.8.1) were "fixed" using paraformaldehyde (PFA). The PFA solution preserves the cells from decaying by covalently crosslinking proteins within the cell, resulting in a penetrable but stable cell structure. Briefly, the media was aspirated from the cells, which were subsequently washed twice using 200 µl DPBS. A 4% PFA in DPBS solution was added, and the plates were left in the dark at 4 °C. After 30 minutes, the PFA solution was aspirated, and replaced with 100 µl DPBS per well, to keep the cells moist.
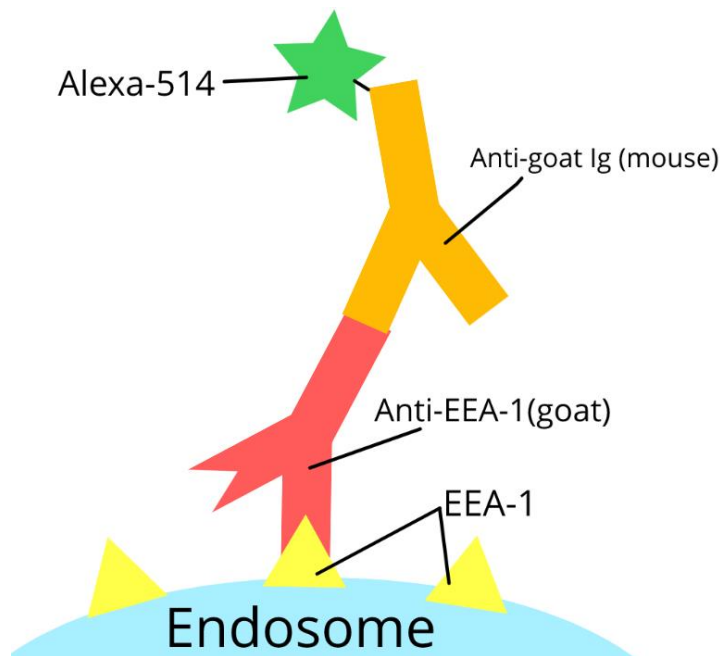
Figure 27. Scheme of immunostaining strategy used to label endosomes.

After fixing, a solution containing goat anti-EEA-1 (Thermo) was added, in a volume such that the concentration of anti-EEA-1 in each well was 1 µg/ml. The plates were then left at 4 °C for 3 hours to allow antibody-antigen binding. The plates were then washed with DPBS, before introduction of Alexa-514-labeled mouse anti-goat immunoglobulin (Thermo), which binds to the anti-EEA-1, as illustrated in figure 27. Simultaneously, Hoescht 33342 stock solution in DPBS (Thermo) was incubated with the cells, at a volume sufficient to achieve 1 µg/ml in each well; Hoescht 33342 stains DNA, allowing visualisation of the nuclei of the cells.

The plates were left for a further 3 hours, before further washing with DPBS. The resulting stained cells were imaged by confocal microscopy, as detailed in section 2.9.2.

2.9   Fluorescence microscopy

Fluorescence microscopy involves any microscopic technique where contrast is achieved by detection of light emitted from fluorophores, rather than be detection of scattered or reflected light. This is often performed in tandem with bright field reflection or transmission images. In this work, two major forms of fluorescence microscopy were used, and are described in this section.

2.9.1   Epifluorescence Microscopy
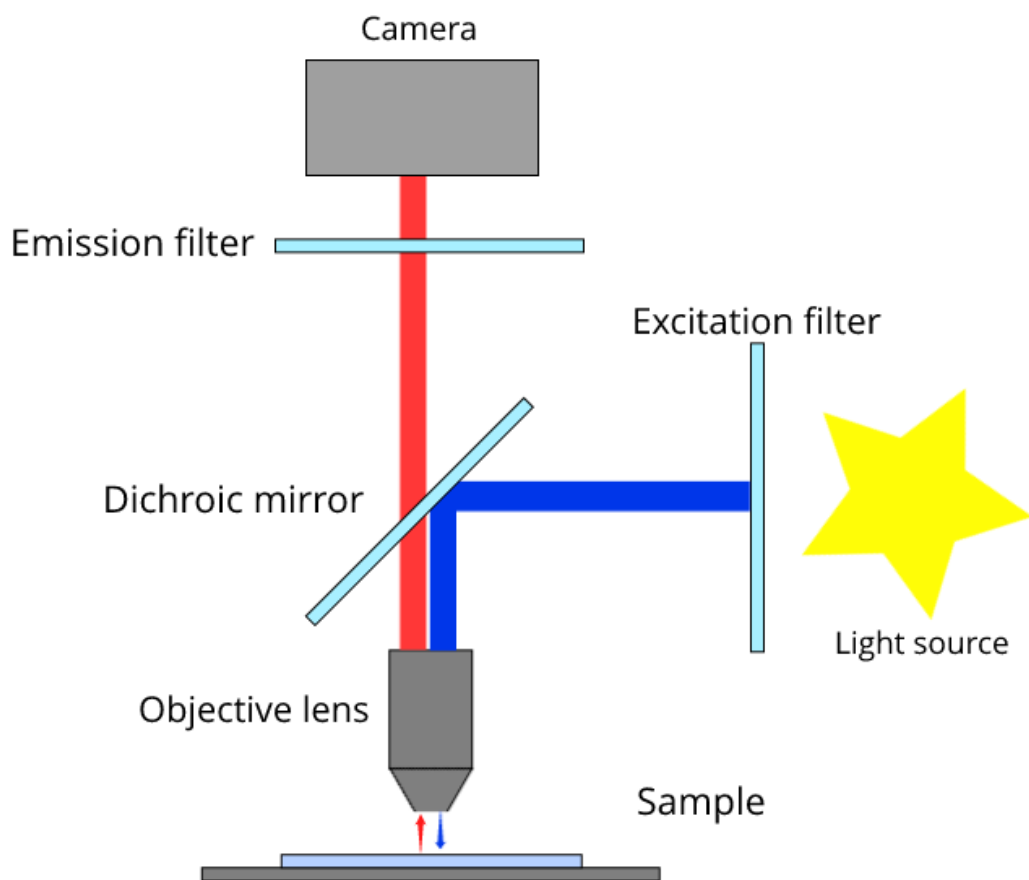
Figure 28. Cartoon of principle of operation of an epifluorescence microscope. A dichroic mirror separates the excitation beam from light emitted by the sample, which is collected by a camera.

Epifluorescence microscopy is the more simple of the two techniques used in the work described in this thesis. In a typical epifluorescence microscope, a light source, usually an incandescent lamp, emits white light, which is collimated and then filtered to the chosen wavelength for excitation of the relevant fluorophore. This parallel light is then reflected by a dichroic mirror, before it is directed onto the back of an objective lens, which is focussed on the fluorescent sample. Fluorescent emission from the sample is collected by the objective lens, and is transmitted through the dichroic mirror, before passing through another filter (to remove extra light) and impinging on the camera or other detection optics. A dichroic mirror is an optical device which reflects light of short wavelengths, but transmits longer wavelengths. The cut-off wavelength below which light is reflected can be chosen. In order for the excitation beam to be reflected, and the emitted light to be transmitted and detected, the correct dichroic mirror for the fluorophore in use must therefore be chosen. Resolution in epifluorescence microscopy is limited by the Abbe limit, and therefore cannot be much better than about 200 nm for green light. In this work, a Nikon e600 epifluorescence microscope was used to analyse samples of cells.

2.9.2   Confocal Fluorescence Microscopy
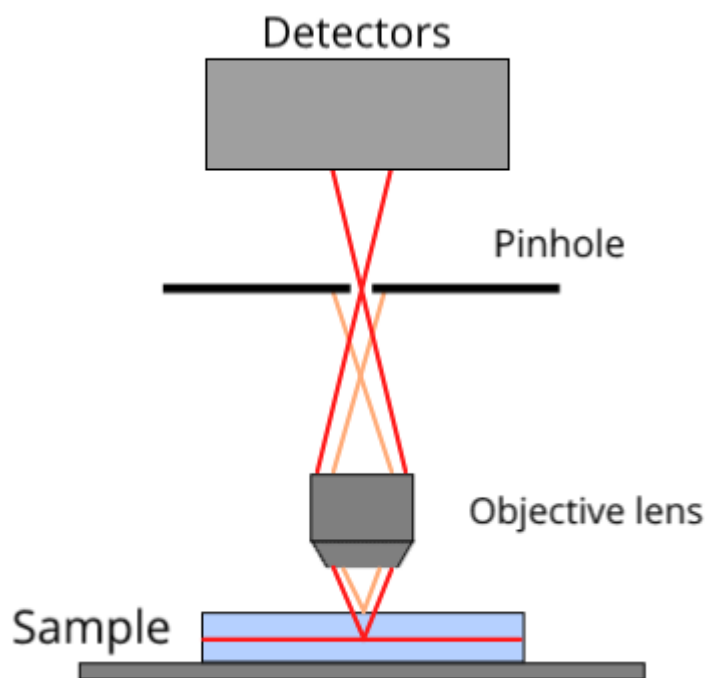
Figure 29. Simplified cartoon of principle of operation of confocal microscope. Light from the image plane (red) is focussed through a pinhole, and light from other depths (orange) is blocked, resulting in acquisition of a fine "slice" in depth.

Confocal microscopic techniques can achieve increased resolution over traditional epifluorescence microscopy by blocking any out-of-focus light using a pinhole. Some confocal-based techniques that rely on stochastic emission by fluorophores can allow for features as small as 10-50 nm to be resolved.[125] In epifluorescence microscopy, light emitted from each depth level in the sample is detected (a significant amount of which, particularly for powerful objective lenses, will be out of focus). Elimination of this light using a pinhole, as in confocal microscopy (figure 29), allows a much narrower depth slice to be acquired in a single images. This allows 3-dimensional images of objects to be acquired, by obtaining and stacking a number of 2-dimensional images at varying depth.[126] High resolution in the x and y (horizontal) directions is additionally achieved by raster-scanning a laser spot over the sample for excitation. The resulting images have excellent horizontal resolution (as low as 10 nm) and improved depth resolution (~50-100 nm) compared to epifluorescence techniques.[125, 126]

Confocal microscopy was performed on samples of cells incubated with QDs using a Leica DMi8 using laser excitation at 488 nm, with adjustable emission filters. For the immunostaining experiments, a Yokogawa CV7000 (AstraZeneca) automated confocal imaging system with selectable monochromated excitation and emission systems was used.

2.10 Cyclic Voltammetry of Q2NS-QD Conjugates

The reduction potential, or redox potential of a species is a measure of the tendency of that species to accept an electron. In other words, for redox species, it is the potential energy of an electron that will reduce that species, or alternatively the potential at the cathode (electron source) for the half reaction at equilibrium, and is connected to the energy level of the orbital that will accept the electron. Redox potential is therefore expressed in volts, often with respect to a standard electrode with well-characterised potential. In electrochemistry, conventionally the standard hydrogen electrode (SHE) is the defined zero-point by which reduction potentials are calibrated, and describes the ideal oxidation of hydrogen, with half reaction:

$$\tfrac{1}{2}\,H_2 \rightarrow H^+ + e^-$$
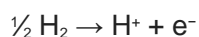
The absolute electrode potential (defined as the potential relative to an electron at rest in a vacuum) of the SHE is 4.44 ± 0.02 V. In solid state physics, when discussing energies of electrons in solids, convention is to use opposite signage (to account of the negative charge of the electron).[127] For redox species in solution, cyclic voltammetry allows direct measurement of the redox potential, with reference to an electrode with known potential

with respect to SHE. The potential difference between a "working electrode" and a "counter electrode" of conductive metal immersed in the solution is measured against a "reference electrode" maintained at a constant potential. The potential is scanned forward and backward at a controlled scan rate, and the current measured at the working electrode is recorded. The resulting plot is termed a cyclic voltammogram; an example is shown in figure 30. The peaks labelled V_{pa} and V_{pc} are the peak anodic and cathodic potentials respectively. The peak cathodic current is reached when all of the substrate at the working electrode has been reduced, and conversely the peak anodic current is reached when it is all oxidised. For a sweeping potential, these are offset from the reduction potential (defined for equilibrium conditions) due to the limitation of diffusion of ions to the electrode. The reduction potential $V°$ is therefore halfway between the potentials of peak measured anodic and cathodic current:

$$V° = \frac{V_{pc} + V_{pa}}{2}$$

(32)
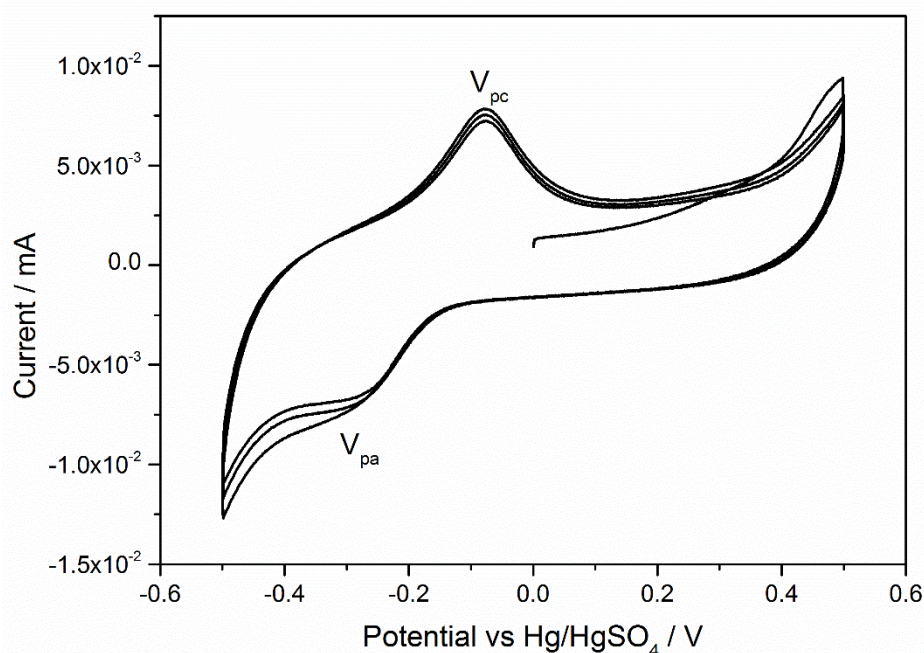
Figure 30. Example cyclic voltammogram, obtained for Q2NS-conjugated CdTe/CdS QDs immobilised on a gold working electrode, against a mercury/mercurous sulphate reference electrode.

For this work, cyclic voltammetry was performed on CdTe/CdS QDs conjugated with the acceptor molecule Q2NS. A working electrode consisting of a 100 nm gold layer on glass was incubated with a solution of 1 mM 6-mercaptohexanol and 0.2 mM 6-amino-1-hexanethiol

in ethanol to form a self-assembled monolayer (SAM), which was then gently rinsed with water. A sample of Q2NS CdTe/CdS conjugates (Q2NS:QD ratio 20:1) in 1 mM HEPES buffer was incubated with the electrode for 1 hour, so that the QDs became electrostatically immobilised on the electrode. Cyclic voltammetry was then performed at 50 mVs^{-1} against a mercury/mercurous sulphate reference electrode in order to obtain the reduction potential.
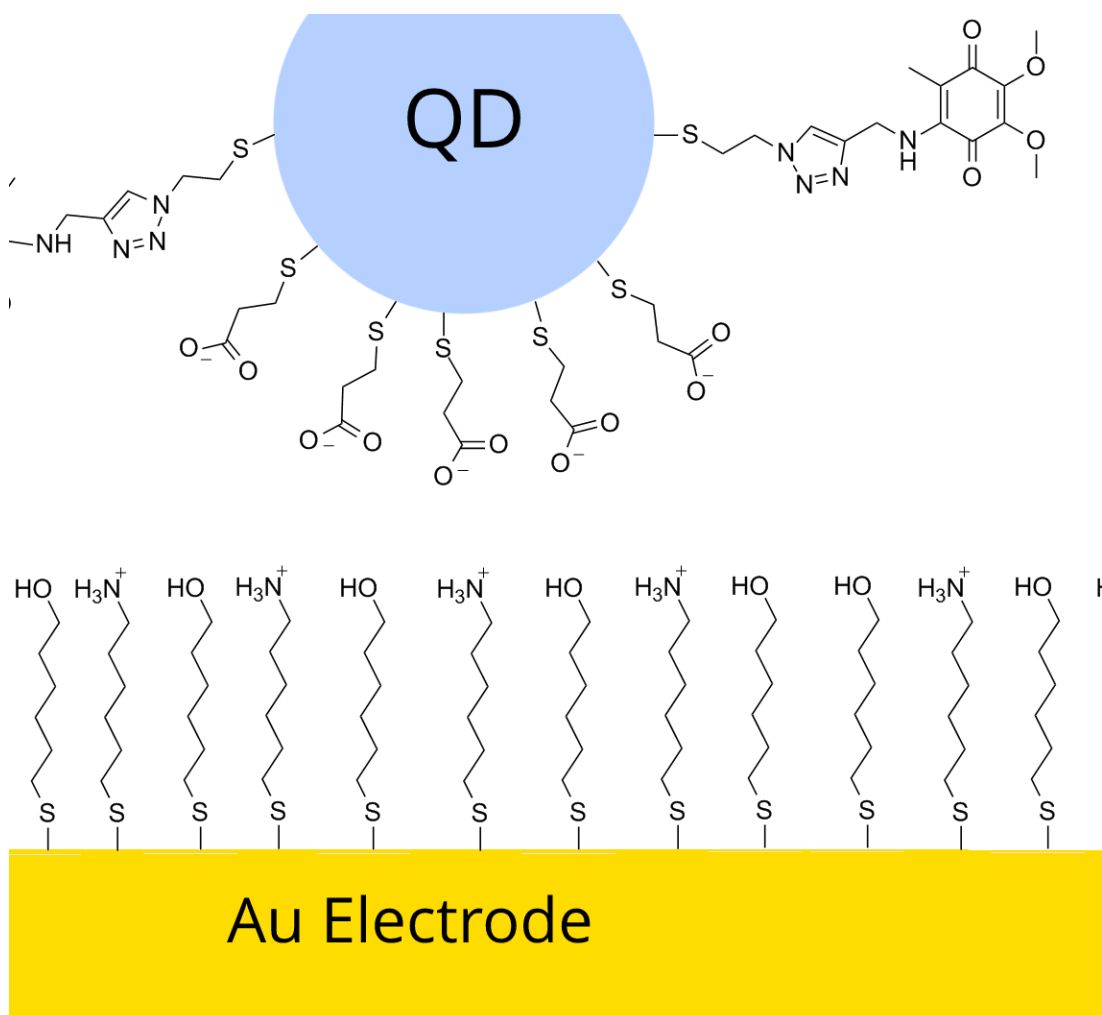
Figure 31. Immobilisation of Q2NS-conjugated QDs on the working electrode. A mixed SAM of 6-mercaptohexanol and 6-amino-1-hexanethiol is used to impart net positive charge to the electrode. The QDs, which are stabilised by TGA, are electrostatically immobilised on the electrode.

2.11 Zeta Potential Measurements – Electrophoretic Light Scattering

Stability of a colloidal dispersion, particularly in aqueous environments, or very polar solvents is often mediated by charge. That is, in a charged homocolloid (where every particle

has similar properties, particularly size and charge) electrostatic repulsion between individual particles will prevent flocculation and preserve the dispersion. The zeta potential (also ζ-potential) is a measure of the degree of this electrostatic repulsion, and is defined as the electric potential, relative to a point far away in medium, of the stationary boundary layer of dispersant on the surface of the particle. For very polar solvents (such as water), this layer of fluid can be quite thick, as strongly charged particles co-ordinate with dipolar solvents to produce highly-ordered layers.

Colloids with large populations of charged ligands or functional groups on their surfaces will therefore exhibit large zeta-potentials. For solutions with high ionic strength, screening of charges by mobile ions in the solution can serve to reduce the zeta potential of a colloid. As a rule of thumb, colloids which exhibit zeta potentials of magnitude greater than 30 mV can be considered stable, with stability generally increasing for higher potentials.[128, 129]

Electrophoresis is the motion of charged particles within a dispersion as a response to an electric field. For an applied electric field E, the electrophoretic mobility is defined as:

$$\mu_e = \frac{v}{E} \qquad (33)$$

Here, v is the drift velocity of the particle as a result of the electric field. The mobility is related to the zeta potential ζ by:[130]

$$\mu_e = \frac{\epsilon_r \epsilon_0 \zeta}{\eta}. \qquad (34)$$

Light undergoes Rayleigh scattering, in all directions, when incident upon small, dilute and diffuse particles. Particularly for monochromatic light, scattered light can interfere from that which is scattered from neighbouring particles. The result is structure in the image of scattered light, known as a "speckle pattern" where constructive and destructive interference causes bright and dark spots depending on the random distances between particles. As the particles undergo Brownian motion (random, jiggling motion due to thermal fluctuations) this speckle pattern will change, according to a timescale related to the speed of motion of the particles. The correlation function $g(\tau)$ describes this timescale. After long times $\tau_0 + \tau$, particles have diffused due to Brownian motion long enough that their new configuration has no correlation to that at τ_0, and the value of $g(\tau)$ is zero. However, at short times, correlations are high, as the particles have not had much time to move, and $g(\tau)$ takes some positive value; perfect correlations (stationary systems, or time differences of zero) give a unitary value to the correlation function.

For particles that are also undergoing drift due to electrophoresis, the frequency of scattered light is Doppler shifted by a frequency v_D with respect to incident light. The correlation function of the mixed signal of scattered and reference light is given by the following expression:

$$g_{mixed}(\tau) = A + B\cos(2\pi v_0)e^{-\Gamma\tau} + Ce^{-\Gamma\tau}.$$ (35)

Here, A, B, C and Γ are constants. The frequency v_0 is related to the Doppler frequency by the equation:

$$v_0 = |v_D - v_M|$$ (36)

Here, the frequency v_M is the modulation frequency, which relates incident and reference light. The correlation function can be acquired by collecting an image of the speckle pattern of a given scattering system undergoing electrophoresis, and extracting the time-resolved intensity at each pixel. The Doppler frequency is related to the drift velocity v by the expression:

$$v_D = \frac{vq}{2\pi}$$ (37)

Here, q is the amplitude of the scattering vector. The velocity can therefore be extracted and used in combination with equations 33 and 34 to determine the zeta potential for the colloidal system.

In this work, zeta potential measurements were made for 50 nM solutions of QDs dispersed in 0.1 M HEPES buffer, adjusted to pH 7.2, using a Malvern Instruments Zetasizer Nano. Briefly, small volumes of solutions are placed in a cell consisting of a thin, U-shaped tube with a gold electrode at each terminus. The instrument then applies an oscillating electric field, and automatically measures and returns the relative population distribution of zeta potentials via the methodology outlined above. Some representative outputs for a sample of TGA-capped CdTe/CdS QDs are presented in figure 32.
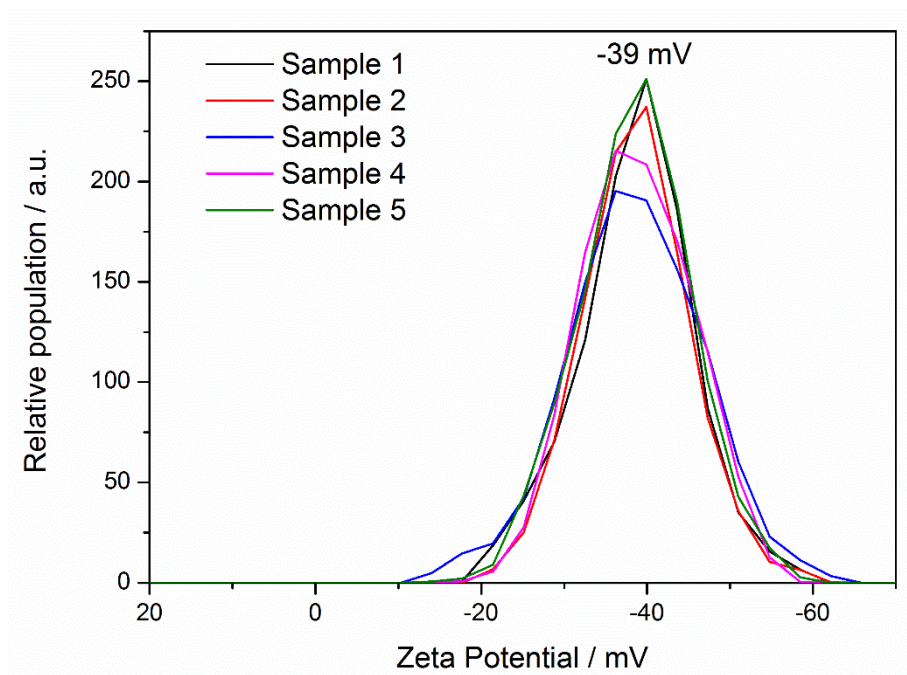
Figure 32. Typical zeta-potential distributions for 5 samples of a solution of TGA-capped CdTe/CdS QDs, as produced by the Malvern Instruments Zetasizer Nano. A common, narrow peak at -39 mV is measured, suggesting stable colloid.

3 Compositional Domains in CuInS$_2$ Quantum Dots

Understanding the excited state dynamics of a particular QD type is critical for its development into a redox sensor. CuInS$_2$/ZnS QDs were attractive candidates for development of redox sensing QDs due to their reduced toxicity[113] and synthetic simplicity in comparison to Cd-based QDs. For the case of CuInS$_2$/ZnS QDs, the excited state dynamics are intrinsically linked to the atomic structure of the QDs, particularly with respect to point defects. The following study was performed in order to more fully understand the internal structure of CuInS$_2$ core and CuInS$_2$/ZnS core/shell QDs, and how this relates to their unusual optical properties.

3.1 Background

As mentioned in section 1.6, toxicity is a significant setback in the application of QDs in biosensing, an issue that is particularly prevalent in cadmium-based QDs. Even outside of biosensing, European regulations (2016/217) that limit the use of cadmium in commercial products provide motivation to work towards cadmium-free QD technologies. Chalcopyrite (I-III-VI$_2$) copper indium sulphide (CuInS$_2$) QDs are emerging as a potentially less toxic alternative.[113, 131-133] Aside from their reduced toxicity compared to CdX (X = S, Se, Te) QDs, CuInS$_2$ QDs are particularly technologically important; they exhibit PL emission from yellow to the near infra-red, the wavelengths where light can penetrate most deeply through biological tissue.[134] As well as the usefulness that this affords to development of biosensors, their broad absorption and large Stokes shift make them ideal candidates for absorbing material in photovoltaics, as well as for use in light-emitting devices.[135, 136]

Compared to most CdX (X = S, Se, Te) QDs, CuInS$_2$ QDs typically display a wide Stokes shift and broad emission, with particularly strong size-dependence; empirical exponential functions that relate particle size to excitonic features have greater exponents for CuInS$_2$ QDs than Cd-based QDs.[40, 118] This behaviour has been ascribed to a radiative recombination mechanism involving crystal lattice defects as the donor state, in a donor-acceptor pair (DAP) recombination scheme,[137-139] although there has been broad discussion in the literature positing varying dominant mechanisms for a wide range of CuInS$_2$ materials.[140-143] In generalised QD systems, energy states associated with structural point defects are shown to be strongly dependent on the size of the QD, which explains the strong size dependence of defect state-related luminescence.[40, 139, 144]

CuInS$_2$/ZnS core shell QDs display a type-I band alignment, which results in the expected increase in PLQY due to passivation of surface trapping states; over-coating CuInS$_2$ cores with a ZnS shell typically results in improvement in PLQY from approximately 4% to around 65%. However, this increase in PLQY is often accompanied by a significant blue shift in the emission wavelength, attributed to exchange of cations between the lattices of chalcopyrite CuInS$_2$ and zinc blende ZnS, whose lattice mismatch is approximately 2%. The result is a partially alloyed structure rather than a true "core/shell" particle with a sharply defined boundary. This alloyed structure has a wider band gap than the core particle.[145]

In 2014, Kraatz et al reported evidence from transient absorption experiments that indicate that the transition responsible for emission in chalcopyrite CuInS$_2$/ZnS QDs involves recombination from an electronic state consistent with an In$_{Cu}$ anti-site defect (a point defect where a copper(I) is replaced by an indium(III) within the lattice).[49] Furthermore, studies have identified that Cu-poor QDs typically display higher photoluminescent quantum yield (PLQY) than their equivalent stoichiometric (Cu:In:S = 1:1:2) counterparts, which is attributed to an increase in the number of In$_{Cu}$ and V$_{Cu}$ in these QDs; these defects are expected to have a lower formation energy in Cu-poor chalcopyrite.[146-149]
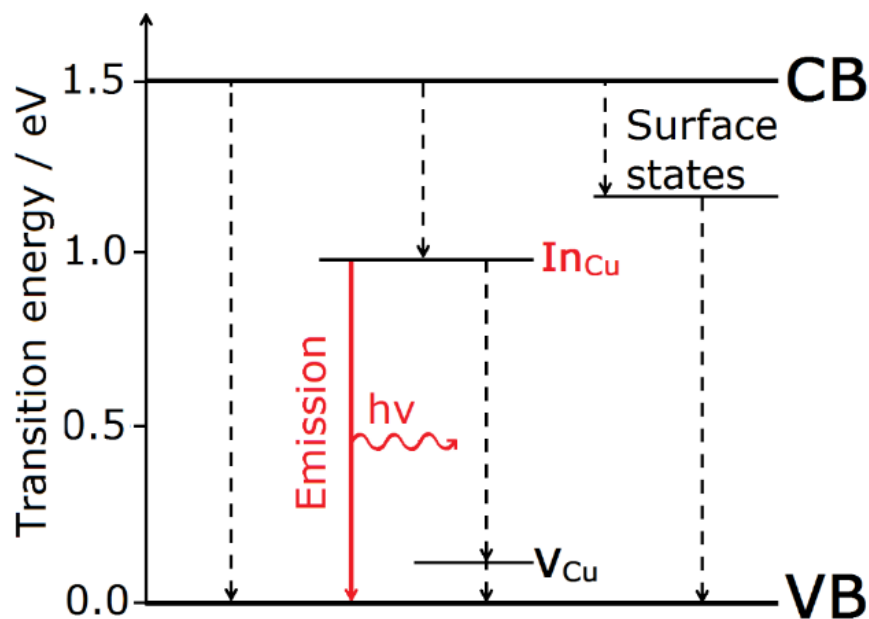
Figure 33. Proposed recombination mechanisms in chalcopyrite CuInS$_2$. Non-emissive transitions are shown with dotted arrows. The emissive transition is assigned to an intra-gap state-to-valence band transition, with the donor state arising as a result of In$_{Cu}$ displacements within the lattice.[49]

The presence of these luminescence-related defects in the QDs has been inferred from spectroscopic data, as well as understanding of the properties of the bulk material, however their nature within the QD crystals had until the time of this work not been investigated. The stated aims of the study are:

- Synthesise and characterise high-quality examples of typical $CuInS_2$ core and $CuInS_2$/ZnS core/shell QDs, which exhibit luminescent properties in line with those currently present in the literature.

- Image the internal crystal structure of the resulting $CuInS_2$ core and $CuInS_2$/ZnS core/shell QDs using electron energy loss spectroscopy (EELS).

- Relate the observed crystal structures to current models for defect-related PL in these QDs.

3.2   Optical Properties

$CuInS_2$ core and $CuInS_2$/ZnS core/shell QDs were synthesised according to the procedures outlined in section 2.1.3. In order to provide a valid control, the core/shell particles that were analysed in this work were grown from the same cores. Both core and core-shell QDs display typical broad band emission, consistent with the defect-related recombination mechanism. Emission spectra and PLQY data were acquired for 50 nM solutions of QDs in chloroform, and are shown in figure 34 and table 1. The core particles displayed a typical broad band PL emission at 688 nm (FWHM 121 ± 1 nm) Addition of the ZnS shell led to a blue shift in the PL emission maximum by 43 nm (maximum 645 nm, FWHM 119 ± 1 nm). This blue-shifting is consistent with literature,[145] and is likely due to incorporation of zinc into the $CuInS_2$ core via exchange of cations. Core particles displayed weak luminescence with a PLQY of 4.1 ± 0.8 %, improving to 36 ± 1 % upon addition of a shell, again consistent with passivation of surface trap states involved with non-radiative recombination of excitons.

UV-Vis spectra were acquired for the same QD dispersions, recorded against a chloroform blank. Both core and core/shell particles show absorption spectra typical for particles with either high size polydispersity or a defect-rich structure, with broad excitonic features. These spectra are included in figure 35. The location of the first excitonic transition is enabled by finding minima in the second derivatives of the absorbance spectrum; the spectra were smoothed using a fast Fourier transform filter included in OriginPro 8.6, before calculation of the derivative. Local minima consistent with the first excitation were located at 572 nm and 582 nm for core and core/shell particles respectively. The red-shift in the position of the first excitation upon shell addition is attributed to a decrease in the band gap energy as the

particle size is increased. The result of this red shift, in combination with the blue shift in PL peak positon upon shell addition, is a large decrease in the Stokes shift, from 116 nm before shell addition to 63 nm post-addition. It is important to note that the first excitonic transition is consistent with excitation to the conduction band minimum, and not the deep intra-gap defect state that is theorised to be principally involved in photoluminescence. Estimation of particle size based on the position of the emission maximum was perfomed by fitting to the empirical equation:[40]

$$d = 68.952 - 0.2136\lambda_{PL} + 1.717 \times 10^{-4}\lambda_{PL}^2 \qquad (38)$$

This returns an average size of 2.6 ± 0.2 nm for the core particles. This calculation was not performed for core/shell QDs, as it would be unwise to approximate them to the core $CuInS_2$ QDs given the blue-shifted PL.
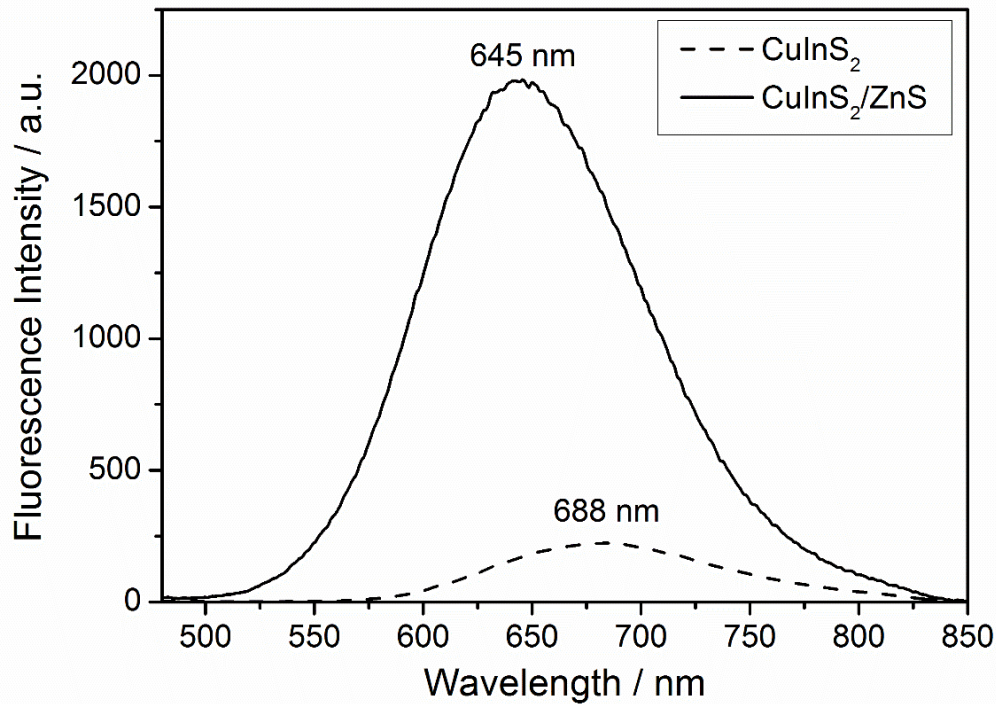
Figure 34. PL emission spectra for core CuInS₂ (dashed) and core/shell CuInS₂/ZnS QDs (solid) with excitation at 450 nm. Spectra are normalised to the measured PLQY for each QD type. Addition of a ZnS "shell" results in a 43 nm blue shift of the PL peak, as well as an 8.9-fold increase in the PLQY.
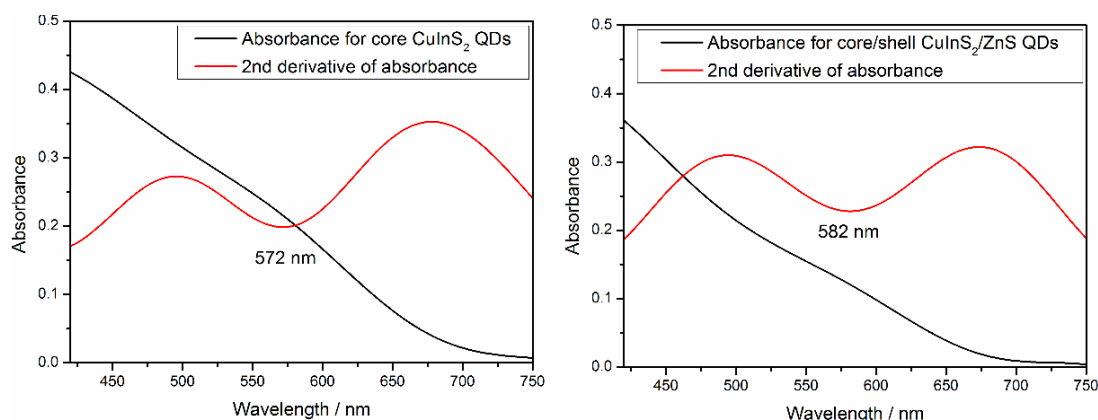
Figure 35. Absorbance spectra and their second derivatives for core CuInS$_2$ (left) and core/shell CuInS$_2$/ZnS (right) QDs.

Importantly, the optical properties of these QDs are typical of those found in the literature.[40, 49, 74, 85, 113, 131, 132, 138, 147] A summary of the most important results is given in table 1.

	PL Emission max	PLQY	1st Excitation	Stokes shift
CuInS$_2$	688 nm	4.1 ± 0.8 %	572 nm	116 nm
CuInS$_2$/ZnS	645 nm	36 ± 1 %	582 nm	63 nm

Table 1. Summary table of optical properties of CuInS$_2$ core and CuInS$_2$/ZnS core/shell QDs.

3.3 Verification of Stoichiometry

Stoichiometry of the core particles was ascertained using x-ray photoelectron spectroscopy (XPS) as described in section 2.6. Samples were prepared by repeatedly drop-casting a 5 µM dispersion of QDs in chloroform onto a gold substrate, resulting in a thick layer of QDs. The poor conductivity of this thick layer required use of an electron-emitting "flood gun" to avoid positive charge accruing over time as electron are ejected. Photoelectron peaks at binding energies of 932.3 eV, 445.8 eV, 161.2 eV and 162.2 eV, corresponding to Cu 2p$_{3/2}$, In 3d$_{5/2}$ and an S 2p doublet respectively, were observed in good agreement with literature data for CuInS$_2$ nanoparticles.[150] These peaks were fitted and used for determination of particle stoichiometry using Thermo Scientific Avantage software with Scofield's relative sensitivity factors; analysis gave the ratio of Cu:In:S to be 1.0:0.9:2.7. The excess of sulphur is attributed to the dodecanethiol (DDT) capping ligand. Importantly, the measured Cu:In ratio is stoichiometric, within the expected instrumental uncertainty.
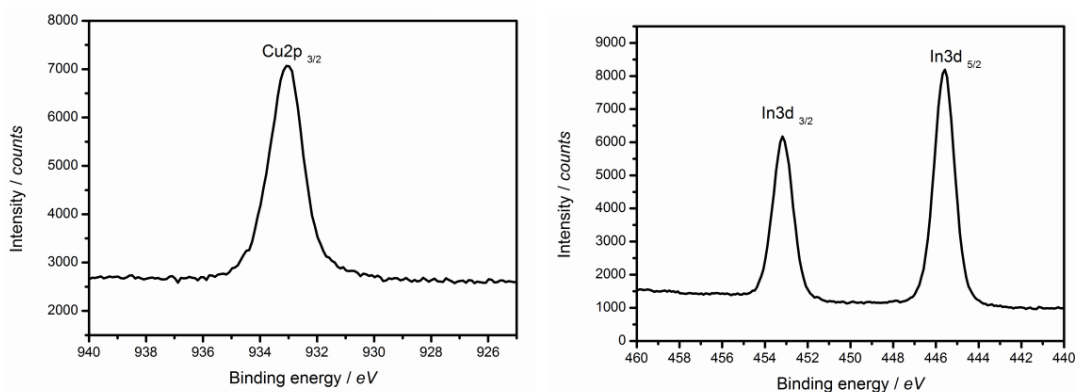
Figure 36. X-ray photoelectron peaks for Cu2p$_{3/2}$ (left) and In3d (right) used to quantify Cu:In ratio for CuInS$_2$ QDs.

3.4   Crystal structure and Particle Sizing

X-ray diffraction was used to confirm the crystal structure of the QDs, and performed as described in section 2.5 Diffraction patterns from both core and core-shell QDs agreed well with literature data for chalcopyrite CuInS$_2$.[151] The similarity in diffraction patterns for core and core/shell particles is expected due to the thin geometry of the shell and low lattice mismatch (2%).

Assuming a shape factor of 0.9, Scherrer analysis of the peak widths suggests an average particle size of 2.1 ± 0.2 nm, slightly smaller than that calculated from optical data.
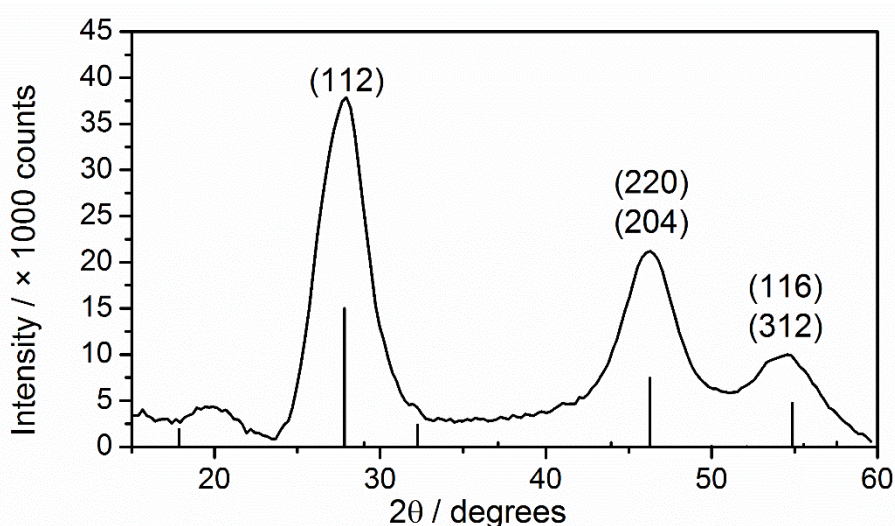
Figure 37. Powder X-ray diffraction (XRD) pattern for a dried sample of core CuInS$_2$ QDs. The spectrum correlates well with literature data for chalcopyrite CuInS$_2$.[151] (ICDD 04-005-5202)

HAADF-STEM was used to image both core and core/shell particles, as described in section 2.7.3. The QDs display a triangular projection, consistent with a tetrahedral shape and in agreement with the literature.[40, 113] The mean size (in this case, defined and measured as the distance from one vertex of the triangular projection of the QD to the opposite side) was determined to be 2.4 ± 0.3 nm (n = 32) for the cores, increasing to 2.7 ± 0.4 nm (n=37) upon the addition of the ZnS shell. Uncertainties in sizes reported here are standard deviations of Gaussian functions used to fit histograms of particle sizes.
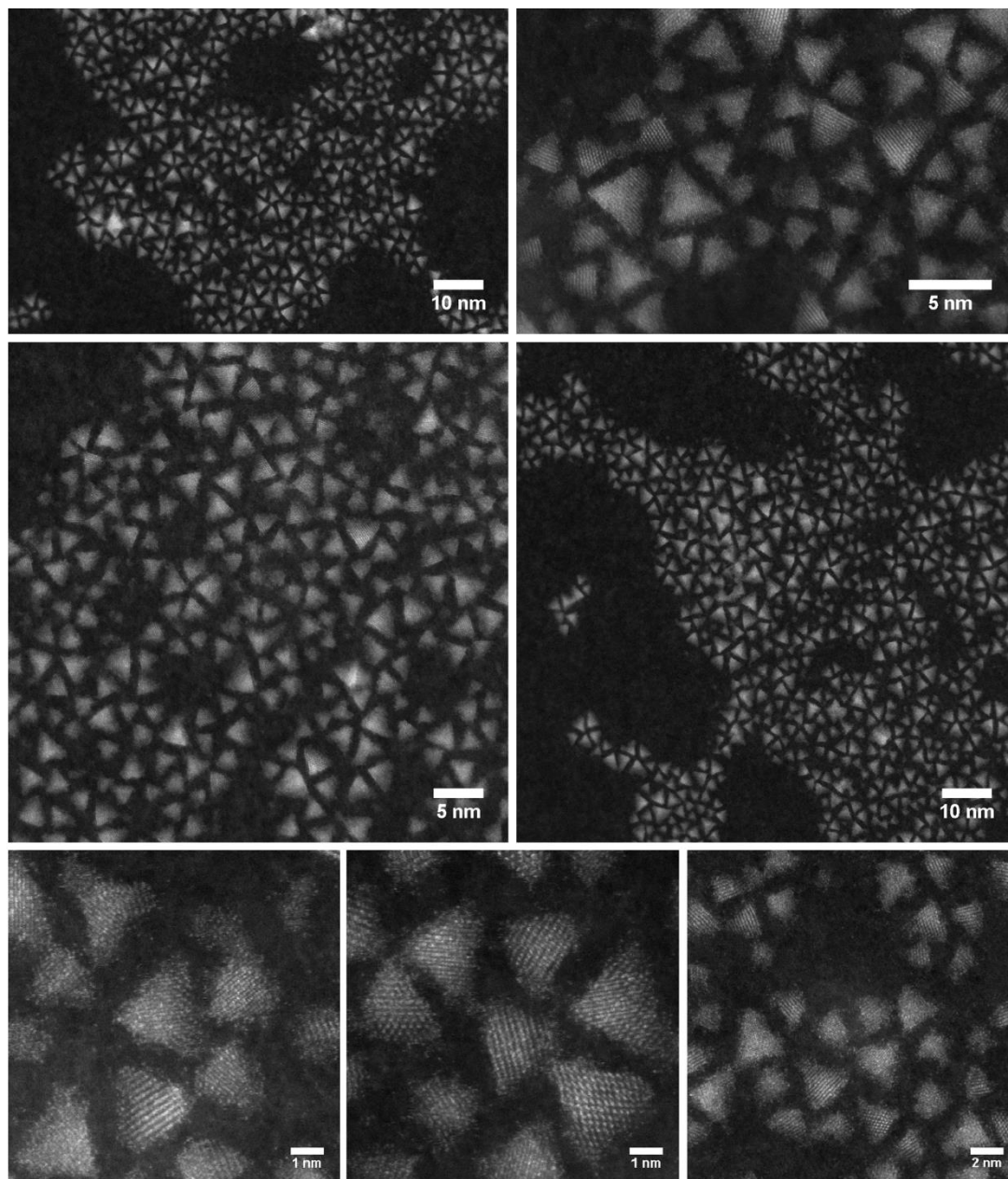
Figure 38. HAADF-STEM images of CuInS₂/ZnS core/shell QDs showing triangular projections and monocrystalline structure.
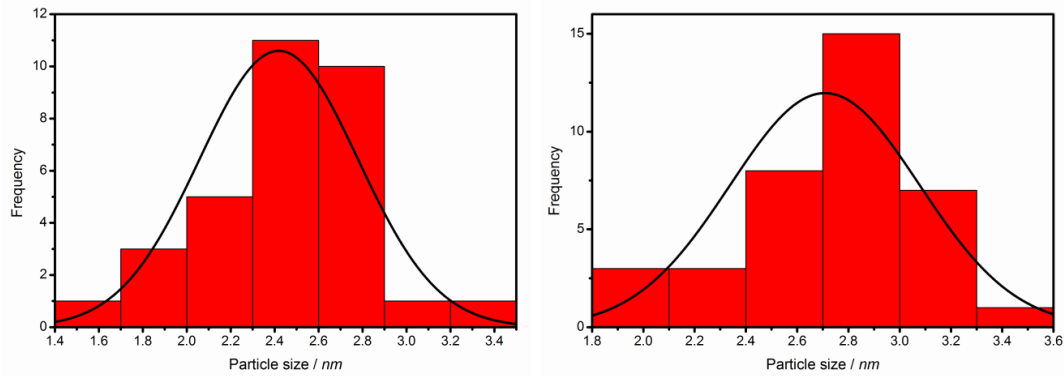
Figure 39. Histograms of particle sizes as measured by HAADF-STEM for CuInS$_2$ core (left, n=32) and CuInS$_2$/ZnS core/shell QDs (right, n=37). Overlaid curves are Gaussian fits used to determine average size and uncertainty.

Imaging parameters were optimised during acquisition of survey images, to avoid effects detrimental to image quality. At high magnifications, using accelerating potentials over approximately 100 kV resulted in damage to the particles, evidenced by morphological changes in the particles during image acquisition, as illustrated in figure 40. For this reason further images, including EELS maps, were obtained using an accelerating voltage of 60 kV. Particularly for the core CuInS$_2$ QDs, surface charging effects were observed at high magnification in areas with high particle density, manifesting in a "blurring" of the image and loss of contrast. For this reason, high-magnification images and EELS maps were acquired only for particles in areas of relatively low particle density.
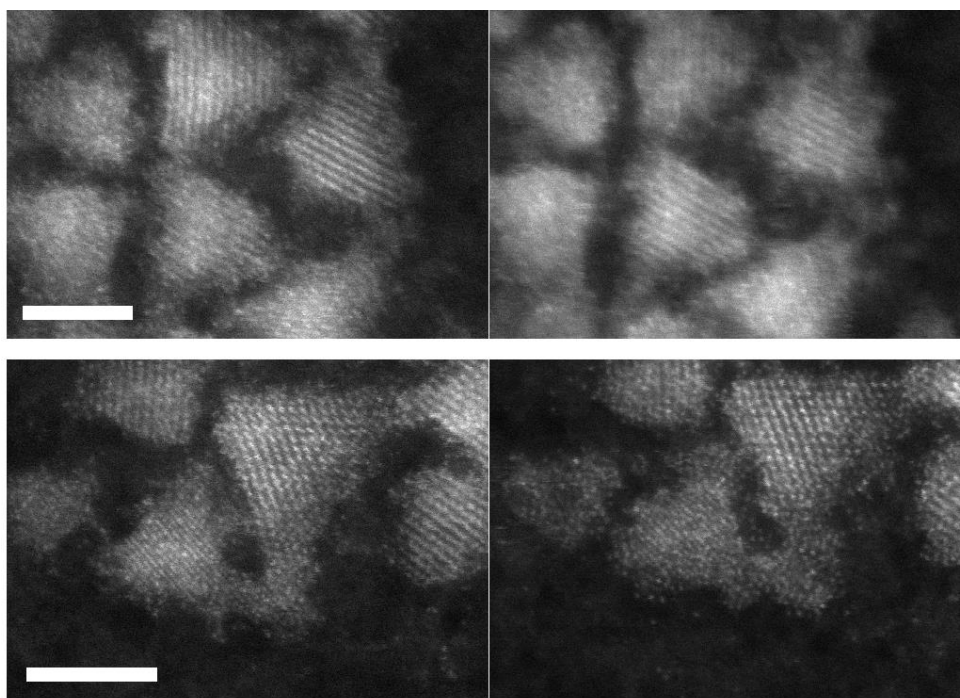
Figure 40. Effects of surface charging (top, left to right) and particle damage (bottom, left to right) on survey image quality for core CuInS$_2$ QDs. Scale bars 2 nm.

3.5   EELS Mapping

Samples of core and core/shell QDs were prepared for EELS measurements as described in section 2.7.4. EELS maps of Cu and In were obtained for samples core and core/shell QDs. Maps were obtained of QD in areas of the TEM grid with a relatively low surface number density, to avoid surface charging effects experienced during acquisition of survey images. Measurements were taken with an accelerating voltage of 60kV; beam energies higher than approximately 100 kV caused damage to the particles in-situ. Depending on the resolution used, the acquisition time for each map was between 7–15 minutes; to minimise imaging time, the parameters for each image were varied, depending on how many particles were to be imaged at once, and how extreme the effects of surface charging were deemed to be for the current sample. Each pixel of an acquired map consists of an EEL spectrum for the corresponding location in the image plane. For each spectrum, core-loss edges corresponding to copper and indium were located, and after subtraction of the background signal using a power-law fit immediately prior to the relevant edge, the intensities were extracted to produce maps showing the spatial distribution of these elements. Intensities of each copper and indium map were normalised to unity to allow convenient reproduction as images; due to the weak signal from the QDs, the acquired data was not deemed to be quantitative to high resolution.
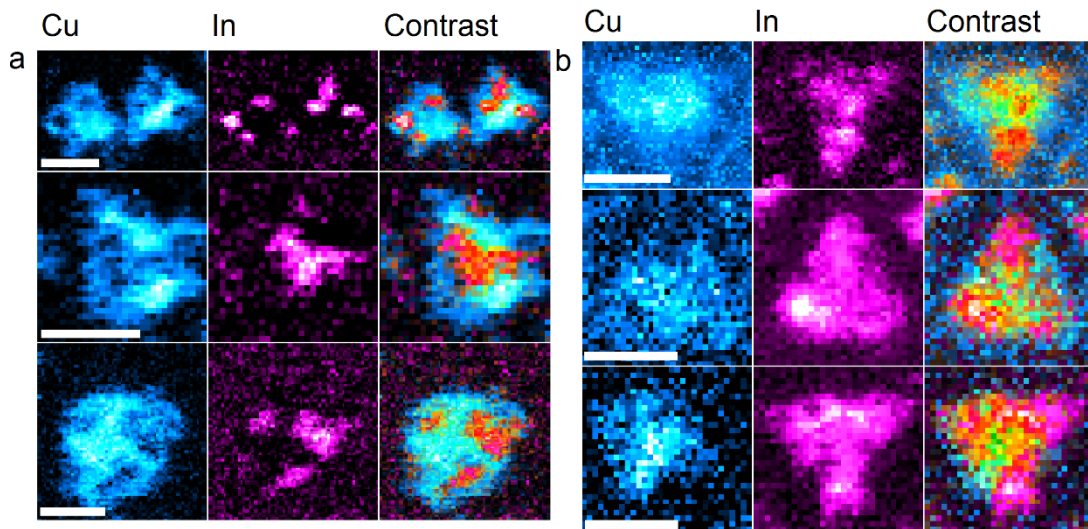
Figure 41. Elemental maps of Cu and In for CuInS₂ core (a) and CuInS₂/ZnS "core/shell" (b) QDs. The column labelled "Contrast" is a subtractive RGB difference overlay of the respective Cu and In maps. On each QD, areas of high In signal correspond with a low Cu signal and vice versa, showing segregation of Cu and In within particles. Scale bars 2 nm.

As shown in figure 41, STEM-EELS elemental maps of the particles systematically show separation of copper and indium within individual particles, giving both In-rich and In-poor areas, which spatially correspond to Cu-poor and Cu-rich, respectively. This is observed in both $CuInS_2$ core and $CuInS_2$/ZnS core/shell particles. In general, indium-rich areas are distributed seemingly randomly within the QD, and are between 4–8 Å in size. For these samples, the number of In-rich segregated areas per particle ranged between 1 and 4. Evidence of these segregated areas immediately suggests an origin of the In_{Cu} antisite defect suggested from spectroscopic data; In-rich/Cu-poor regions are expected to have a number of In_{Cu} displacements in stoichiometric $CuInS_2$ if the chalcopyrite lattice structure is preserved, which XRD experiments suggest is the case. Furthermore, studies of formation energies in $CuInS_2$ and the analogous chalcopyrite copper indium selenide ($CuInSe_2$) suggest a low formation energy for these In_{Cu} defects, especially when present as part of a $In_{Cu} + 2V_{Cu}$ defect pair.[149, 152] In fact, presence of the $In_{Cu} + 2V_{Cu}$ defect system is also known to promote formation of $Cu_{In} + In_{Cu}$ defect pairs, resulting in large "clusters" of defects within the lattice.[153] It is worth noting that the formation energy of In_{Cu} is expected to be lowered in Cu-poor $CuInS_2$, concurrent with the observation of increased quantum yield in these off-stoichiometric QDs.[148] In fact, the large tolerance to off-stoichiometry displayed by the analogous $CuInSe_2$ in the Cu-poor regime has been explained by the stability of the $In_{Cu} + 2V_{Cu}$ pair.[154]

This compositional heterogeneity within particles will lead to a wide variance in environments for the donor-state In_{Cu} defects; the length scale across which composition varies is frequently larger than that of the size of a single In_{Cu} + $2V_{Cu}$ defect pair. It has previously been shown that the energy level of an impurity or defect-related electronic state is strongly dependent on its environment – in this case this is not only the location of the defect within the particle, but the local composition; the band gap of $CuInS_2$ has been shown to be closely related to the Cu:In ratio, and the energy of these defect states is dependent on the local band gap.[155, 156] Compositional heterogeneity therefore leads to heterogeneity in both band gap and defect state energy within individual particles. This effective broadening of features of the band structure in turn therefore leads to the broad PL emission characteristic of $CuInS_2$ QDs.
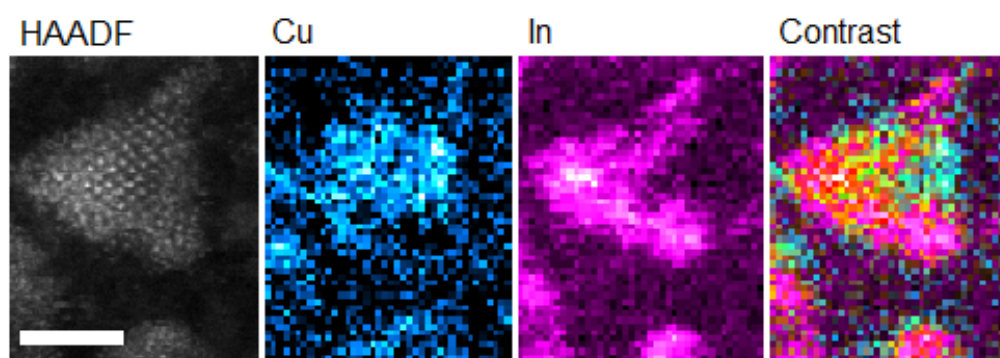
Figure 42. HAADF TEM image, along with elemental maps of Cu and In for a CuInS₂/ZnS QD., showing lattice structure and elemental segregation.

For the $CuInS_2$/ZnS core/shell QD, the degree of segregation in some particles appears smaller than that of the core $CuInS_2$ QDs. This may be due to an annealing process that occurs during the shell growth step, as well as the internal rearrangement of the lattice as the aforementioned cationic exchange with ZnS takes place. In combination with the integration of Zn into the QD, this suggests an origin for the discrepancy in Stokes shift between the core and core/shell QDs for the same reasons as outlined above; variation in local composition, and therefore local bandgap will change the energy level associated with the emissive In_{Cu} defects.

3.6   Concluding remarks

The optical characteristics of both $CuInS_2$ core and $CuInS_2$/ZnS core/shell QDs are in agreement with the previously posited model of In_{Cu}-defect mediated DAP emission. A new insight is the observed compositional heterogeneity, which is identified as the origin of these

luminescent centres. Although many synthesis routes for these QDs are present in the literature, and it is not possible to confirm that these will all yield equivalent internal compositional distribution, the characteristic wide PL and large Stokes shift displayed by chalcopyrite QDs from a broad gamut synthesis routes does suggest internal compositional heterogeneity is an inherent feature of chalcopyrite $CuInS_2$ QDs; it is a feature of the defect-tolerant nature of chalcopyrite $CuInS_2$.[132]

The close lattice mismatch with ZnS and favourable band alignment means that ZnS can act as an effective passivant of $CuInS_2$ surface states that might otherwise lead to non-radiative recombination. However, spectroscopic data also suggests a certain amount of Zn is incorporated into the core of $CuInS_2$/ZnS core/shell particles during the shell growth step, however the segregated, defect-rich structure of the $CuInS_2$ core is conserved.
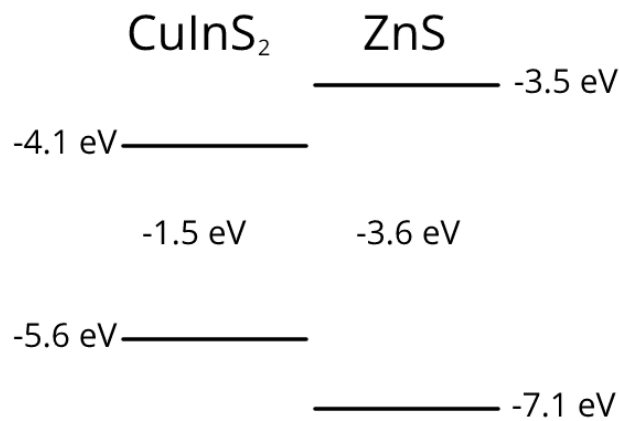
Figure 43. Band gap alignment at minimum energy transition for chalcopyrite CuInS₂ and ZnS. The band alignment is such that any photogenerated exciton in a CuInS₂/ZnS core/shell is confined to the core, and ZnS acts as an effective passivant of CuInS₂ surface states.[157]

The observed separation of Cu and In is consistent with a large population of In_{Cu} defects, which support intra-band electronic states involved in radiative recombination of excitons, leading to the characteristic photo-physical properties of $CuInS_2$ QDs. The energies associated with these states are highly dependent on the local bandgap, which in turn is strongly dependent on local composition. This accounts for the broad spectral features associated with absorption and luminescence in these QDs, as well as the marked change in spectral properties when zinc is introduced during the shell addition step.

This new understanding of the presence of natural intrinsic defects within $CuInS_2$ QDs identifies them as an ideal platform for further study of the control and effects of defects on QD properties. The segregated, defect-rich nature of these particles can be considered analogous to that of highly doped semiconductor QD, providing a simple model platform for their study.[158] A limitation in this approach to studying doping in QDs is that it is difficult to precisely control individual particle stoichiometry; many particles displayed segregation of differing degrees to others. However, the ease of production and high luminescence of these QDs, as well as advances in microscopic and spectroscopic techniques (such as those described in this chapter, as well as electronic-optical techniques such as single-particle cathodoluminescence) will mean these QD can provide a model platform for developing mechanistic understanding of doping in QDs.

4 Excited State Dynamics of CdTe/CdS QD-Acceptor Systems

The excited state dynamics of charge transfer-based QD/acceptor redox sensors is currently under-investigated; most studies focus on steady state optical properties of such sensors and their applications to biology. In this chapter, the excited state dynamics of a model QD-acceptor conjugate were investigated by a number of time-resolved and steady state techniques, with the aim of providing insight into how current technologies might be improved.

4.1 Background

Most of the QD-based redox sensing strategies described in section 1.7 are based on the principle of photo-induced charge transfer between a QD and some redox-active ligand. For these sensors, understanding the time dynamics of the charge transfer process between a QD and its conjugated acceptor/donor enables strategies to be designed to enhance the efficiency of transfer, and limit the impact of any competing processes. Aside from development of redox sensors, charge extraction from QDs is already a widely studied field.[59] For example, in QDs applied to photovoltaics, extraction is required before charges recombine either radiatively, with typical timescales of tens to hundreds of ns, or non-radiatively, where trapping or Auger recombination can occur in the first few ps after excitation.[159] While it is often straightforward to predict steady-state optical properties of QDs of a number of different materials, given information about particle size and band structure, the excited state dynamics in QDs is less widely understood, and often differs greatly between apparently similar particles.[160]

For effective redox-sensitive QDs, a system must be designed which exhibits a redox-switchable, luminescence-quenching charge or energy transfer process that is significantly faster than the timescale associated with radiative recombination. For sensors based on charge transfer, this can be achieved either by increasing the radiative recombination timescale, decreasing the charge transfer timescale, or by employing a combination of the two. Ideally this is achieved without increasing the influence of other non-radiative relaxation processes.

CdTe/CdS core-shell QDs exhibit a type-II heterostructure which results in spatial separation of the electron and hole after excitation, as illustrated in figure 44. The band alignment is such that a photo-excited electron will be confined to the CdS shell, with the resulting hole being confined to the core. Thinner CdS shells will result in a quasi-type-II alignment where

the hole is confined to the CdTe core, and the electron is delocalized across the whole QD. This charge separation greatly increases the recombination lifetime vs the core-only QDs, even for thin shells. [161, 162] Another advantage of the charge separation is the expected increase in charge extraction efficiency due to the location of the electron on the CdS surface. This charge separation and long recombination lifetime compared to other QD types means that CdTe/CdS core/shell QDs are expected to be excellent candidates for the development of charge transfer-based QD redox sensors.
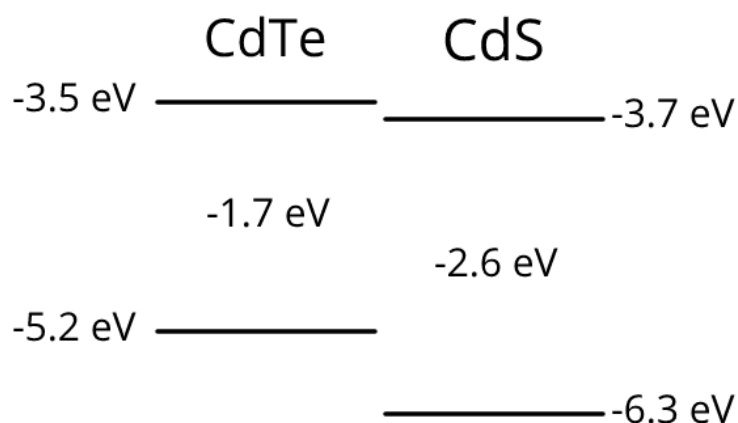
Figure 44. Band gap alignment at minimum energy transition for bulk zinc blende CdTe and CdS. The close energetic proximity of the conduction band minima result in a type-II or quasi-type-II band structure in QDs, where the electron is confined to the shell or delocalised, and the hole is confined to the core.[161, 162]

Quinones are a popular choice for electron acceptors in redox-sensing QD-acceptor conjugates.[17, 21, 98, 111, 112] Q2NS is an electron acceptor based on the structure of the metabolic cofactor coenzyme Q_{10}, which has previously been shown to exhibit redox-switchable quenching of luminescence of conjugated CdSe/ZnS core/shell QDs, both in solution and in within living cells, where changes in redox environment were resolved.[112] The proposed mechanism of quenching is by electron transfer to Q2NS, when the quinones of Q2NS are in the oxidised state. Reduction of Q2NS moves the LUMO to a level inaccessible by conduction band electrons in the CdSe/ZnS QDs, in turn preventing the quenching due to electron transfer.
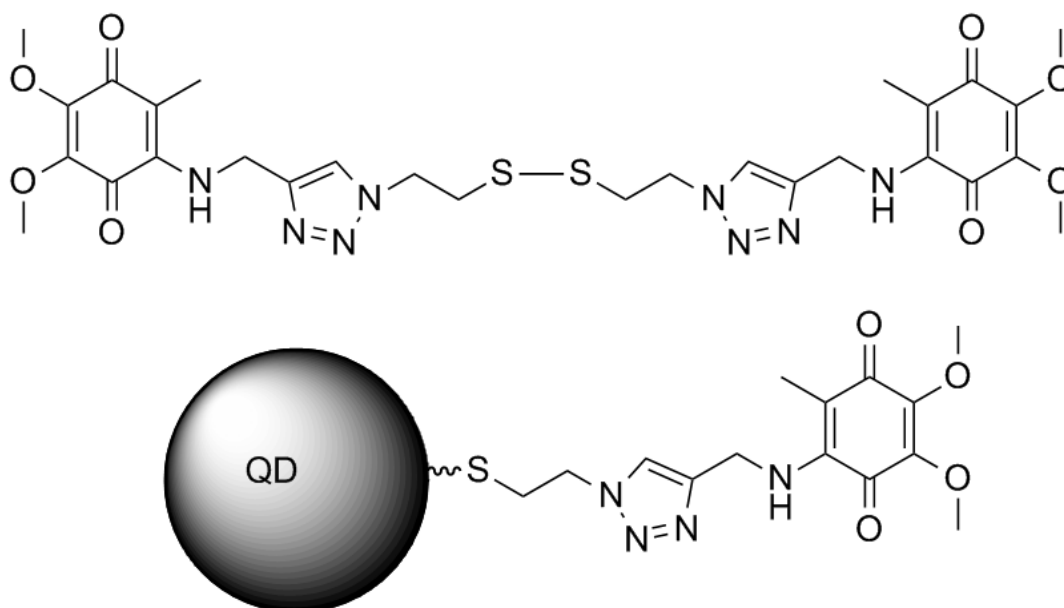
Figure 45. Structure of electron acceptor Q2NS (top). Conjugating to QDs (bottom) involves reduction of the disulphide bond to form a thiolate bond with the cations on the QD surface.

For the reasons outlined, coupled with the synthetic simplicity of Q2NS, CdTe/CdS QDs were chosen for use with Q2NS for the study of excited state dynamics in QD-acceptor redox sensors, shown in figure 45. Although it has previously been concluded in the literature that electron transfer to oxidised Q2NS is responsible for quenching of luminescence, the precise mechanism has not been investigated. The aims of this study are therefore:

- Synthesise CdTe/CdS QD-Q2NS conjugates with varying ratios of Q2NS:QDs,
- Assess whether luminescence can be reversibly switched by changing the redox state, and determine whether quenching is more efficient than for type-I CdSe/ZnS QDs,
- Employ optical spectroscopic techniques, combined with theoretical calculation, to determine the precise mechanism of quenching.

4.2 QD Synthesis

TGA-stabilised CdTe/CdS core/shell QDs were synthesised according to the method described in section 2.1.1 The solution was heated under reflux for 1 hour to grow the core CdTe QDs. Thiourea was added in a Cd:S ratio of 1.5, and the solution was refluxed for a further 1 hour to allow formation of the CdS shell. The resulting QD dispersions were cleaned using procedures described in section 2.1.4 and dispersed in ultra-pure water. The resulting QDs displayed bright emission at 557 nm (FWHM 44 nm), with absorption characterised by

a first excitation feature at 528 nm (Stokes shift 29 nm), as located by a minimum in the 2nd derivative of the absorption, shown in figure 46.
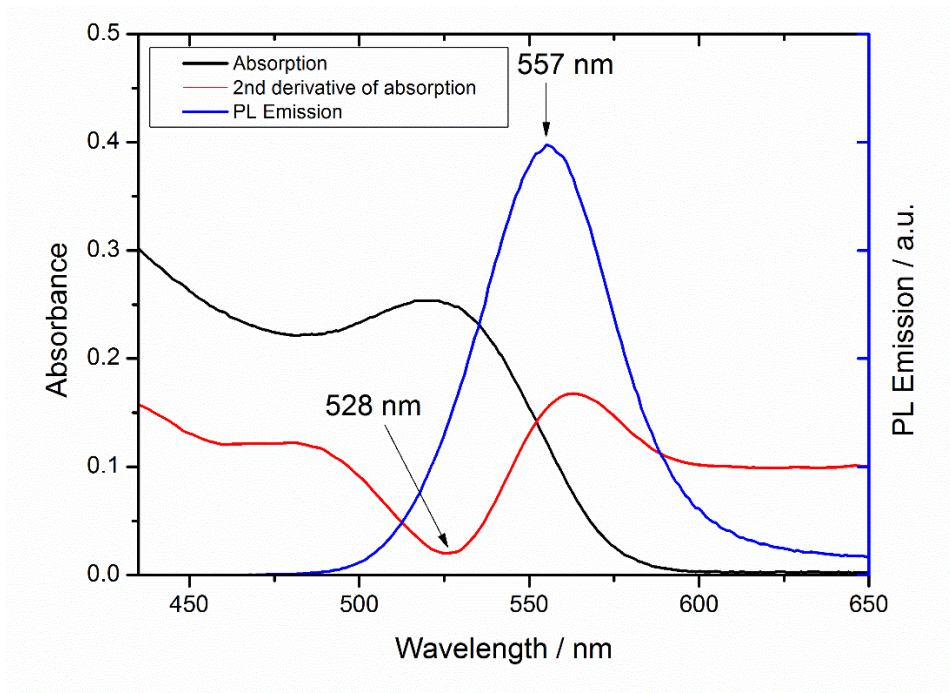
Figure 46. Absorbance and PL emission spectra (λ_{ex}=420 nm) for CdTe/CdS QDs. The red line represents the second derivative of the absorption spectrum.

Two minima are visible in the second derivative of the absorbance spectrum, at 528 nm (consistent with the band edge transition) and 460 nm (consistent with a higher-level transition). For core-only CdTe QDs, studies comparing experimental observations with theoretical calculation show that these minima can be associated with specific excitonic transitions.[163, 164] However, it has been shown that adding a shell to a core CdTe QD, particularly one that achieves a type-II structure, significantly changes the position of higher level transitions.[165] It is therefore only possible to assign the band edge as the $1S_{3/2}$-1s excitation, resulting in a hole in the $1S_{3/2}$ state and electron in the 1s excited state.[163, 164]

The concentration of the QD solution, as well as an estimate of the QD size, was determined using the methods of Yu et al. For simplicity, the approximation that the QDs were CdTe only was made. The average diameter was determined by the empirical equation:

$$d = (9.8127 \times 10^{-7})\Lambda^3 - (1.7147 \times 10^{-3})\Lambda^2 + 1.0064\Lambda - 194.84 \qquad (39)$$

Here, Λ is the wavelength of the first excitation (determined from figure 46) and d is the diameter, calculated to be 3.0 nm. The molar extinction coefficient at the wavelength for the first excitonic transition is then calculated by:

$$\epsilon(\Lambda) = 10043 D^{2.12} \qquad\qquad (\,40\,)$$

This was found to be equal to $9.9 \times 10^4\ M^{-1}cm^{-1}$. The concentration of the stock solution was calculated, then diluted to yield a 4 µM dispersion in ultra-pure water.

QD sizes were then also determined by TEM. Bright-field TEM images of samples prepared as described in section 2.7.1 were acquired as described in section 2.7.2 (figure 47). The QDs are approximately spherical in shape, and diameters were calculated by manually fitting ellipses to the QDs using ImageJ, and recording the length of both semi-major and semi-minor axes. Sizes for 82 QDs were measured. Fitting a histogram of particle sizes to a normal distribution (shown in figure 48) gave an average diameter d = 3.2 ± 0.4 nm, which corroborates with the size determined by optical spectroscopy.
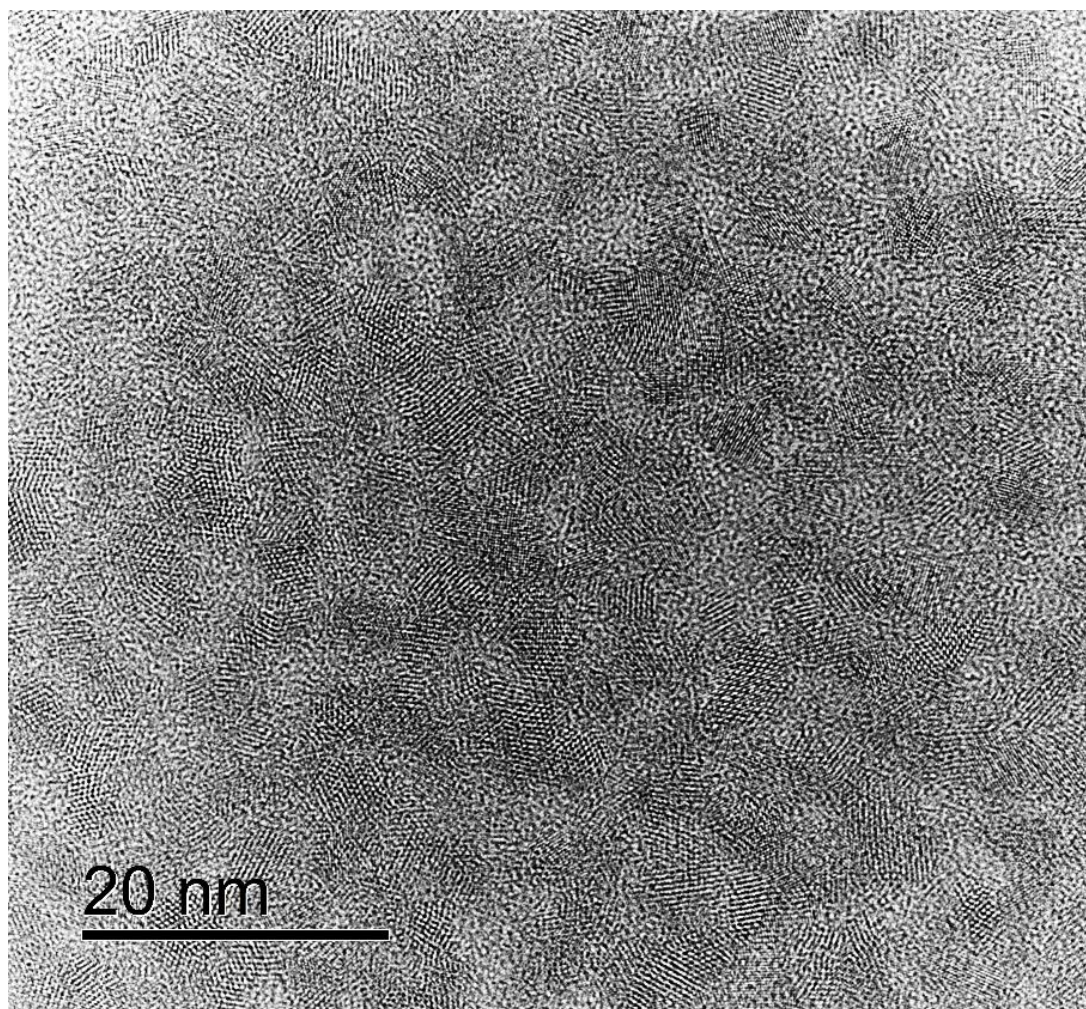
Figure 47. Typical bright-field TEM image of CdTe/CdS QDs, used for determination of average particle size.
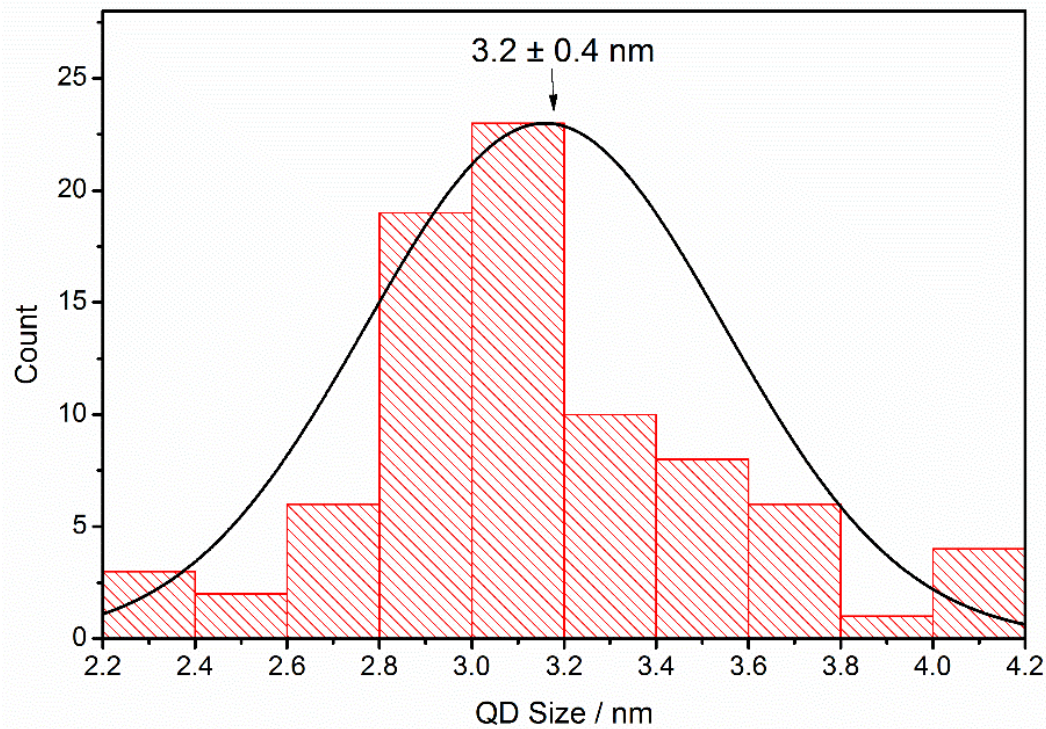
Figure 48. Histogram of diameters of CdTe/CdS QDs measured via TEM. The black curve is a normal distribution with peak at 3.2 nm with standard deviation of 0.4 nm (n=82).

4.3   Ligand exchange

The molecule Q2NS was synthesised as described in section 2.2. QD/Q2NS conjugates were produced in QD:quinone ratios of 1:10, 1:20, and 1:40, as well as a control sample where no Q2NS was added, by the methods described in section 2.3. These samples are referred to as 10Q, 20Q, 40Q and 0Q respectively. Note that the notation used here is based on the number of quinones per QD, not the amount of Q2NS; one unit of dimeric Q2NS accounts for two quinone groups. Completion of the ligand exchange was determined by measuring the absorbance of the samples before and after cleaning via precipitation and centrifugation, as shown in figure 49. Subtracting the normalised absorbance of the sample before cleaning from the absorbance of the sample after, leaves a residual signal that can be compared to the absorbance of a solution of Q2NS. No significant signal from absorbance of Q2NS is visible in the residual, suggesting that all added Q2NS is strongly associated with the surface; this is interpreted as completion of the ligand exchange reaction.
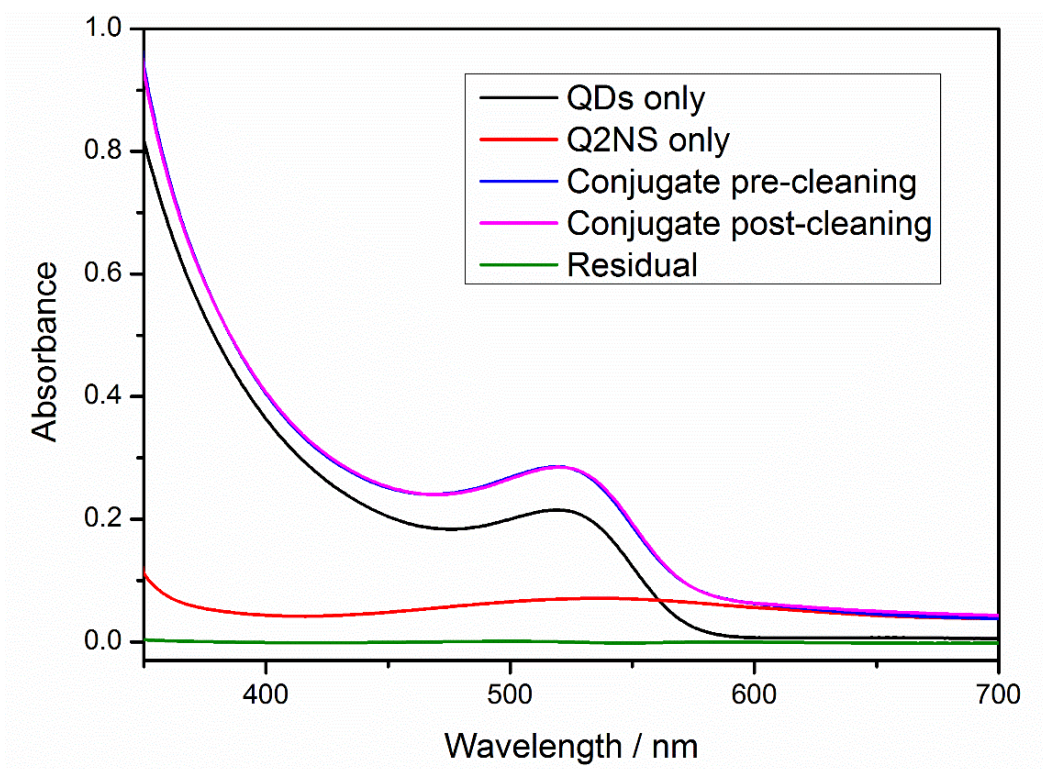
Figure 49. UV-Vis absorbance spectra of Q2NS-QD conjugated before and after cleaning. The residual (green) is the signal obtained by subtracting the absorbance of conjugates after cleaning (pink) from that before cleaning (blue). The black and red curves are the absorbance of equivalent amounts of QDs and Q2NS in solution.

The progress of the ligand exchange was also followed using PL spectroscopy. The sealed reaction vessel (a 4 mL cuvette) was placed in the spectrometer, and the PL intensity at the max emission wavelength was measured once per minute. The beam was blocked between measurements to reduce the effects of photo-degradation, and the sample was continuously stirred. After introduction of Q2NS to the QD solution, the PL intensity rapidly drops off as Q2NS associates with the surface, as shown in figure 50. This reduction in PL intensity is preserved after cleaning, as shown in figure 51.
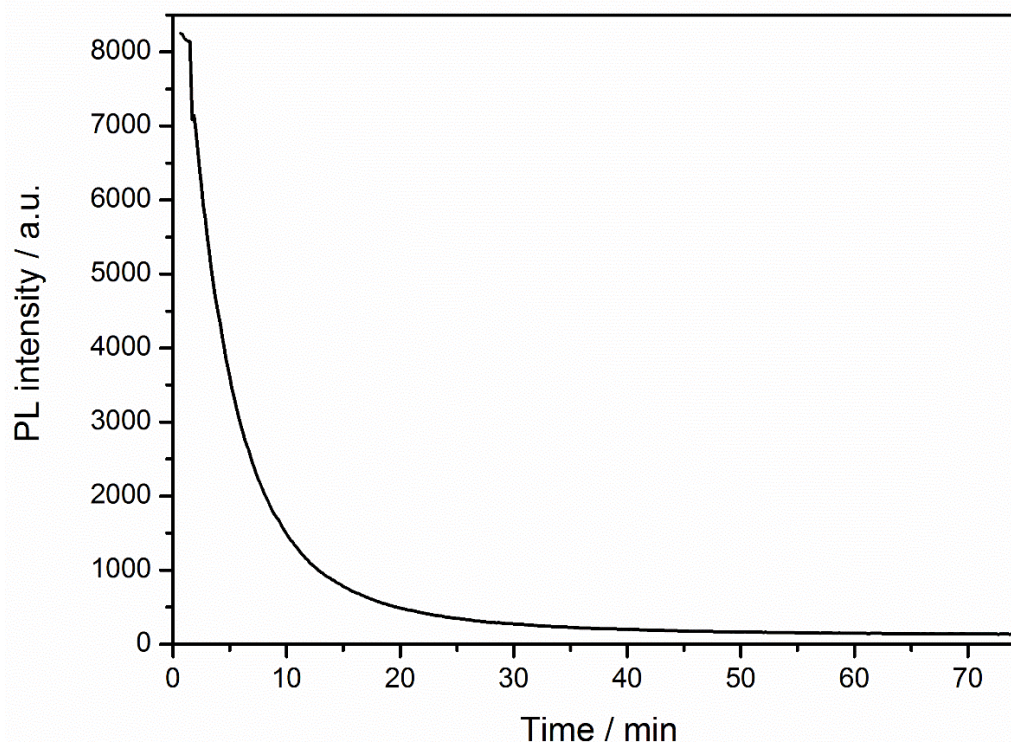
Figure 50. PL intensity vs time for 0.5 µM CdTe/CdS QDs incubated with 5 µM Q2NS (20Q).

A control experiment was performed, where Q2NS was replaced by the quinone molecule 2,3-Dimethoxy-5-methyl-p-benzoquinone (CoQ$_0$), the starting material in the synthesis of Q2NS. This molecule consists of the quinone "sensing" part of Q2NS without the "linker" that attached to the QD. Ligand exchange procedures were followed with both Q2NS and CoQ$_0$, to obtain a quinone: ratio of 20:1, in both cases. The resulting particles were cleaned, and their PL spectra acquired. Samples with Q2NS display a significantly quenched PL vs control (no quinone). However, samples with CoQ$_0$ do not display a significant decrease in the PL, suggesting that CoQ$_0$ has been removed during the cleaning procedure, and therefore does not strongly associate with the QDs. This further suggests that the mechanism of binding of Q2NS to the QDs is via formation of a thiolate bond; CoQ$_0$ does not possess the disulphide or thiol group necessary to form this bond.
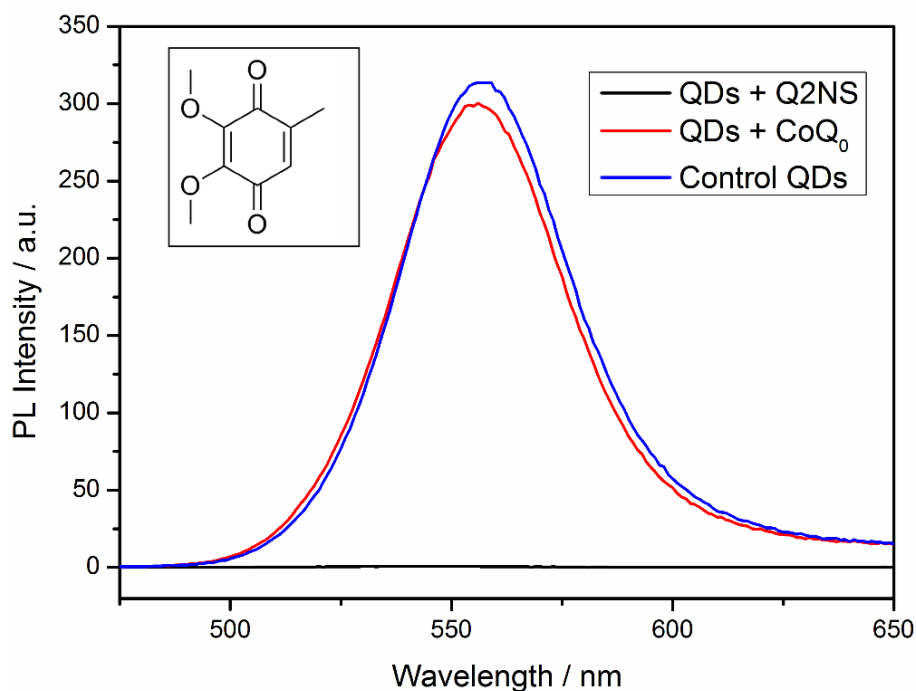
Figure 51. PL spectra (λ_{ex} = 420 nm) of samples of QDs after following ligand exchange and cleaning procedures with Q2NS (black) and CoQ$_0$ (red). Binding of Q2NS to the QD surface strongly quenches the QD luminescence. Inset: structure of CoQ$_0$.

4.4 Measurement of Per-Quinone Quenching Efficiency

A consequence of the presence of a "linker" between the QD and quinone acceptor group is that each acceptor is likely only to be responsible for the quenching of luminescence of a single QD. Importantly for small acceptor:QD ratios, the population of Q2NS bound to the QDs can be assumed to follow Poissonian statistics.[59] For a given Q2NS:QD ratio λ, the photoluminescence quantum yield (PLQY) can therefore be expressed as

$$I_\lambda \; = \; I_0 \sum_{n=0}^{\infty} \frac{\lambda^n e^{-\lambda}}{n!} (1 - 2\kappa_q)^n. \qquad (41)$$

Here, κ_q is the per-quinone quenching efficiency, defined as the probability that a single quinone group will quench an event that would otherwise result in radiative recombination, with $\kappa_{mol} = 2\kappa_q$ as the per-molecule efficiency. The parameter κ_q is related to the Stern-Volmer quencher rate coefficient k_q by the expression $\kappa_q = k_q\tau$, where τ is the excitation lifetime. In equation 41, the parameter n is the number of Q2NS on any particular QD, found with probability $P(n) \; = \; \frac{\lambda^n e^{-\lambda}}{n!}$, and I_0 is the PLQY for an unquenched sample.

To measure the efficiency κ_q, Q2NS:QD conjugates were prepared with Q2NS:QD ratios of 0 to 10. Figure 2 shows the measured PLQY for these samples; the above expression was fitted

using a weighted least-squares regression scheme to his data, as also shown in figure 52, resulting in a value for $\kappa_q = 0.21 \pm 0.02$.
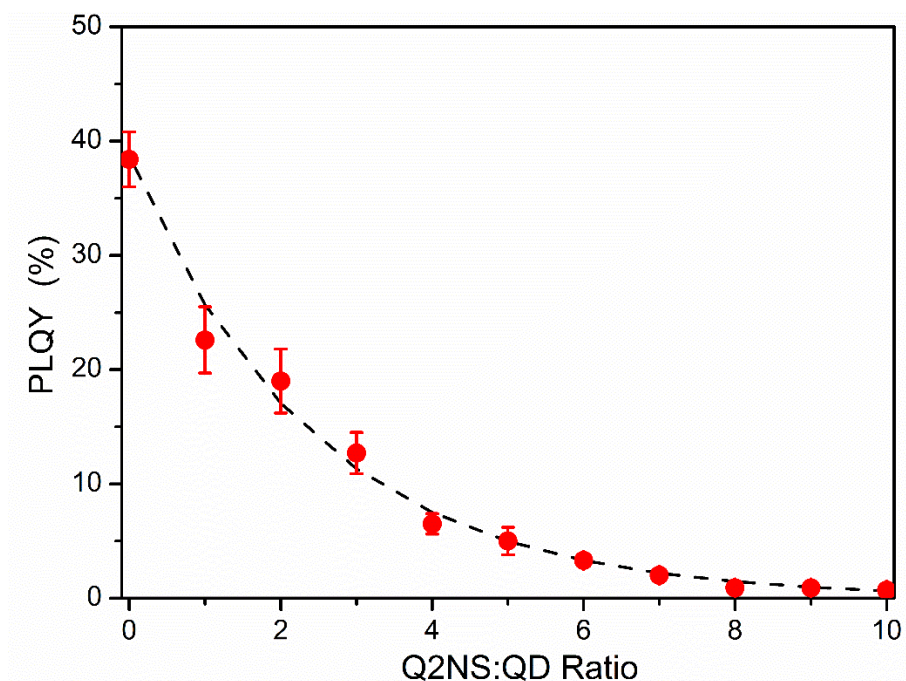
Figure 52. PLQY vs Q2NS:QD ratio (λ in equation 41) for Q2NS-QD conjugates in the ambient oxidised state. The dotted curve represents fitting to a quenching function that considers a Poissonian distribution of quenchers around QDs.

This quenching is highly efficient compared to other systems in the literature, where a large number (~100) of acceptors are typically required to achieve ~70% quenching of PLQY.[98, 111, 112] This suggests either that charge transfer from type-II or pseudo-type-II QDs is more efficient due to charge separation, or that there is a new and distinct mechanism that is responsible for charge transfer in these CdTe/CdS core/shell QDs.

4.5   Redox-dependent PL of Conjugates

PL spectra and PLQY for 4 mL, samples with 0, 10, 20 and 40 quinones per QD (termed 0Q, 10Q, 20Q and 40Q respectively) were measured with excitation at 420 nm. In order to reduce the quinones, 100 µl of a solution containing 100 mg/ml sodium dithionite and 100 mg/ml sodium ascorbate were added to each cuvette in a protective atmosphere. The solutions were thoroughly stirred and the PL spectra and PLQY measured. Results are summarised in table 2 and figure 53.

For oxidised samples 10Q, 20Q, and 40Q the luminescence was quenched by 98.7%, 99.8%, and 99.9%, with respect to the control (0Q) sample, as measured by comparison of PLQY.

This quenching is accompanied by a 6 nm blue shift in the luminescence peak position. The quenching is attributed to a fast electron transfer process between the QD and the quinones of Q2NS. The blue shift is attributed to the slight size polydispersity of the QDs; larger particles which possess longer-wavelength emission are less likely to possess a small number of Q2NS due to their increased surface area. The blue shift is more pronounced for 10Q and less for 40Q; at higher ratios of Q2NS:QD the number of QDs with few (1-6) quinones is very small, if a Poissonian distribution is assumed.

	0Q	10Q	20Q	40Q
Oxidised	38.7 %	0.7 %	0.08 %	0.03 %
Reduced	57.9 %	50.0 %	42.7 %	36.9 %

Table 2. Photoluminescent quantum yields of samples 0Q, 10Q, 20Q and 40Q before and after addition of reducing agents.
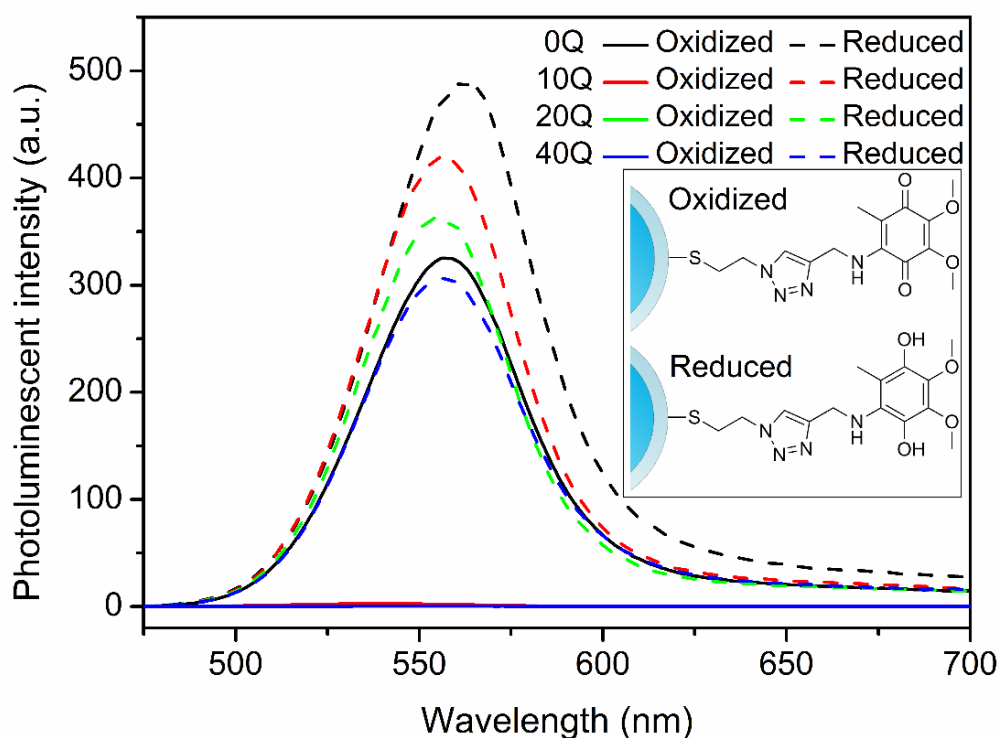
Figure 53. PL spectra (λ_{ex} = 420 nm) for QD:Q2NS conjugates 0Q to 40Q before and after addition of reducing agent. For samples with Q2NS, reducing agents cause recovery in luminescence from a highly-quenched state. Inset: Structure of QD-bound Q2NS in oxidised and reduced states.

Addition of the reducing agents suppresses the quenching effects of the quinones to an extent proportional to the number of Q2NS per QD, consistent with almost total suppression of the electron transfer event that results in quenching. The fact that PL does not recover to

100% of that exhibited by the control QDs is attributed to incomplete reduction of quinones in the aqueous environment, which cannot be made totally free of oxidants such as diatomic oxygen; samples with large Q2NS populations will therefore still have a small fraction of oxidised quinones even after introduction of the reducing agent. For the 0Q sample, the PL was red-shifted with respect to that of the 10Q, 20Q, and 40Q samples after addition of the reducing agents. This is attributed to passivation of surface traps by the Q2NS, which employs a thiolate binding complex.[166] Again for the 0Q sample, the improvement in PLQY after addition of reducing agents is attributed to their passivation of surface states, and the resulting suppression of non-radiative recombination pathways. The exact mechanism of this passivation is unclear, but improvement in PLQY upon addition of electron-donating or negatively-charged surface treatments is commonly observed for CdTe QDs.[45, 117] This is corroborated by transient PL and TA data, mentioned in the next sections.

4.6 Transient PL Spectroscopy

Transient PL traces were acquired for the QD samples, and fitted to multi-exponential decay functions (equation 25) as described in methods section 2.4.4. These traces are shown in figure 54.
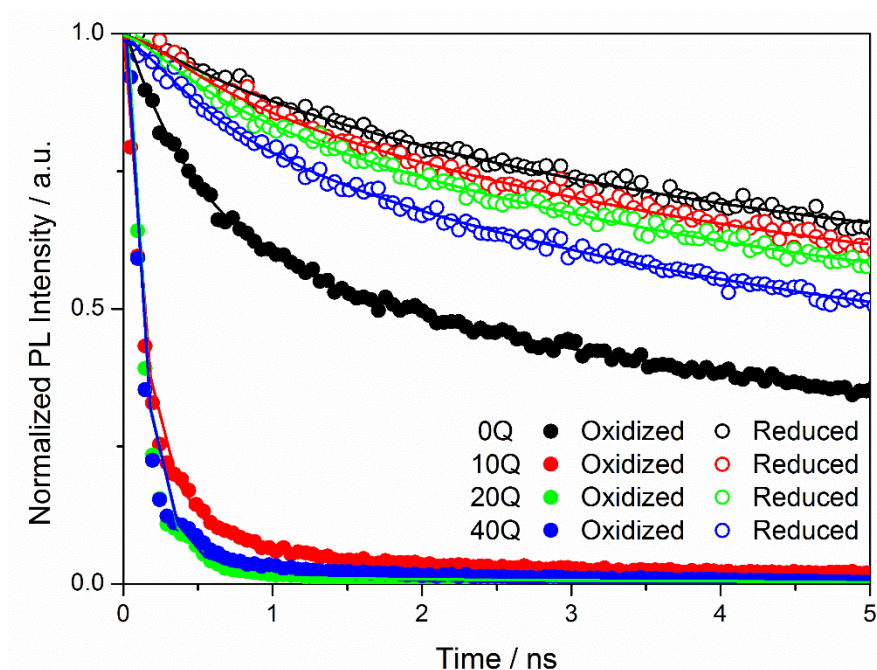
Figure 54. PL decay traces (λ$_{ex}$ = 420 nm, λ$_{em}$ = 560 nm) of samples in oxidized (filled circles) and reduced state (empty circles) for samples 0Q (black), 10Q (red), 20Q (green) and 40Q (blue). Bi-exponential or tri-exponential fits are displayed as continuous lines.

The oxidised samples display two distinctive behaviours; samples with Q2NS display a rapid drop in PL intensity after excitation which is adequately described by a tri-exponential decay of the form $I = A_0^{PL} + A_1^{PL}e^{-t/\tau_1^{PL}} + A_2^{PL}e^{-t/\tau_2^{PL}} + A_3^{PL}e^{-t/\tau_3^{PL}}$ and characterised by time constants τ_1^{PL} = 0.14 ± 0.01 ns, τ_2^{PL} = 0.46 ± 0.03 ns and τ_3^{PL} = 4.0 ± 0.9 ns. It is important to note that the fastest time constant is approximately the same as the response time of the instrument (0.10 ± 0.01 ns) and so it is not possible to resolve the underlying process behind this time constant, as shown in figure 55.
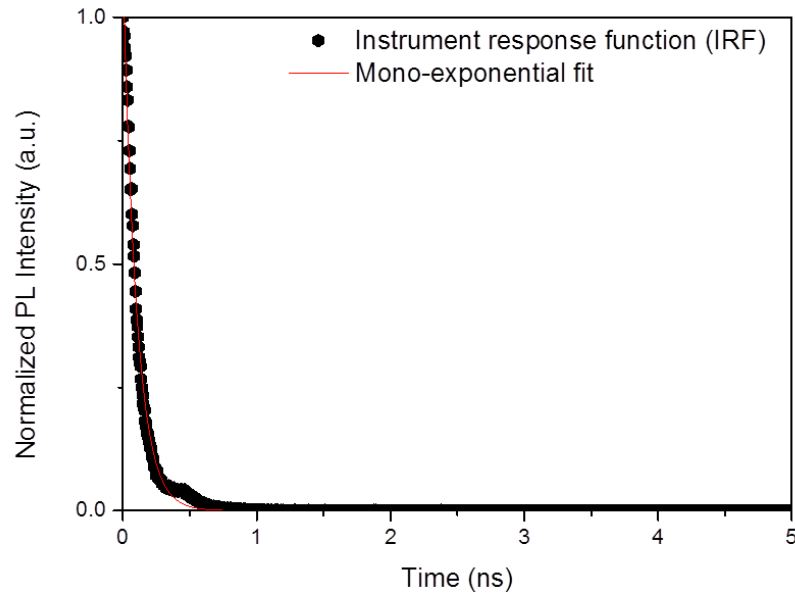
Figure 55. Instrument response function (IRF) of spectrometer used for transient PL measurements (λ_{ex} = 420 nm, λ_{em} = 560 nm). The "decay" signal due to scattering precludes measurements faster than about 0.1 ns.

Still in the oxidised state, the sample 0Q shows a much slower decay, that can be fitted by a bi-exponential equation using only τ_2^{PL} and τ_3^{PL}. This is a clear indication that a fast (at least 0.14 ± 0.01 ns) charge transfer occurs from the QDs to the oxidized Q2NS, causing the quenching observed in static PL measurements. In contrast, only very small differences are observed between the samples with and without Q2NS in the reduced state, shown in figure 54. Reduced samples with Q2NS (10Q, 20Q, 40Q) no longer exhibit the abrupt decay associated with the supposed fast transfer process. The fast time constant (τ_1^{PL}) is no longer needed to adequately fit these decays, which can again be described as bi-exponential with time constants τ_2^{PL} and τ_3^{PL}. The disappearance of this fast decay constant is in agreement with the recovery in PL observed in the static PL experiments, and is consistent with the reduced Q2NS no longer acting as a PL-quenching electron acceptor after it is chemically

Figure 57. TA bleach spectra for all samples in oxidised (left) and reduced (right) states.

Pump wavelength λ_{pump}=420 nm.

Figure 58 shows the first 50 ps of the corresponding time resolved absorption transients for each of the samples, obtained at a wavelength near the peak of these bleach features (530 nm). Also shown are tri-exponential fits to these transients. The reduction of absorbance is again due to the filling of states by electrons cooled to the CBM, and the value of $\frac{\Delta A}{A}$ (the fractional absorbance change) is proportional to the average occupation of the CBM.[167] These bleach transients rapidly reach an initial peak that then decays to a plateau over a few 10s of ps. This is typically observed in colloidal QD systems in which hot electrons created by the high energy pump pulse quickly cool down to the CBM giving rise to the initial peak. The decay is then produced by sub-nanosecond depopulation of the CBM, including by trapping of these cooled electrons, while the plateau represents long-lived electrons that may eventually contribute to emission by radiative recombination. Previous studies have shown that typical samples of CdTe QDs exhibit heterogeneity in the recombination pathways employed by individual QDs; some QDs contain a number of traps, where some are trap-free.[45, 168] The significant plateau in the TA transients confirms the presence of sufficient number of these trap free QDs (or QDs with very slow trapping rates), and explains why a PLQY of ~40% can be observed when the apparent trapping rate observed from the TA decay is much faster than radiative recombination. Sub-nanosecond decays to a plateau can also be observed during Auger recombination of excitons, when multiple excitons are generated in a QD due to absorption of more than one photon per QD, per pulse. However, in this case, low enough excitation fluences were used to make the probability of this process negligible ($<1.5\times10^{-05}$). A table of biexciton formation probabilities is available in the appendix (9.2).
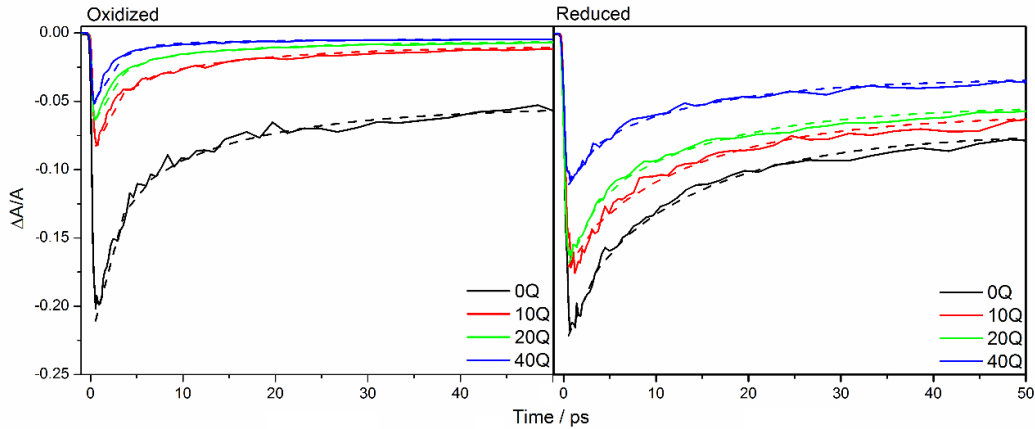
Figure 58. Absorbance transients obtained at 530 nm for all samples in oxidised (left) and reduced (right) states. Pump wavelength λ_{pump}=420 nm. The solid lines are guides for the eye, while the dashed lines represent multi-exponential fits.

For samples that have not been reduced, the peak amplitude is significantly reduced in samples with Q2NS (10Q, 20Q and 40Q) compared to control (0Q). The peak amplitude decreases as the ratio of Q2NS:QD increases, reaching approximately 40%, 30% and 20% of the peak amplitude for 10Q, 20Q and 40Q respectively. This agrees with the previous evidence that suggests electrons are extracted from the QD to the Q2NS before they cool to the CBM. Furthermore, for the oxidised samples with Q2NS, the "plateau" amplitude, associated with long-lived electrons that contribute to radiative recombination, is almost zero. This is in agreement with the observed quenching of PL, and further suggests that electrons that do cool to the CBM can also be transferred to the oxidised Q2NS.

After the samples have been reduced, a large increase of both peak and plateau amplitudes is seen for the samples with Q2NS. The increase in plateau amplitude, in particular, is in agreement with the improvement in PL observed after reducing the Q2NS. The increase in peak amplitude is consistent with suppression of transfer to the quinones that occurs before cooling to the CBM, as seen in the bleach spectra in figure 57. For the 0Q sample, a small increase in the bleach signal is observed. This increase in bleach signal, in combination with longer PL decay and improved PLQY for the 0Q sample upon addition of reducing agent further suggests that the reducing agent also affects other non-radiative recombination pathways, besides controlling quenching by changing the oxidation state of the quinones.

The decay curves for all samples are well described by a tri-exponential fit, of the form $I = A_0^{TA} + A_1^{TA}e^{-t/\tau_1^{TA}} + A_2^{TA}e^{-t/\tau_2^{TA}} + A_3^{TA}e^{-t/\tau_3^{TA}}$ with time constants of τ_1^{TA}= 2.0 ± 0.1 ps, τ_2^{TA} = 13.4 ± 0.8 ps and τ_3^{TA} = 480 ± 50 ps. A_0^{TA} is a time-independent constant, which represents

the plateau in the traces. The longest of the time constants, τ_3^{TA}, agrees with the value of τ_2^{PL}. The other two, τ_1^{TA} and τ_2^{TA}, are much shorter than the time response of the PL lifetime experiment, and so cannot be resolved in the transient PL data. However, the processes associated with these time constants would still contribute to the amplitude associated with τ_1^{PL}. Due to the inhomogeneity in QD samples mentioned before, rigidly assigning transfer timescales precisely to transitions is difficult; it is possible to fit almost any decay function with an arbitrarily large number of terms, however a small number of terms fairly safely allows a sensible general description of the de-excitation dynamics of an ensemble of QDs.
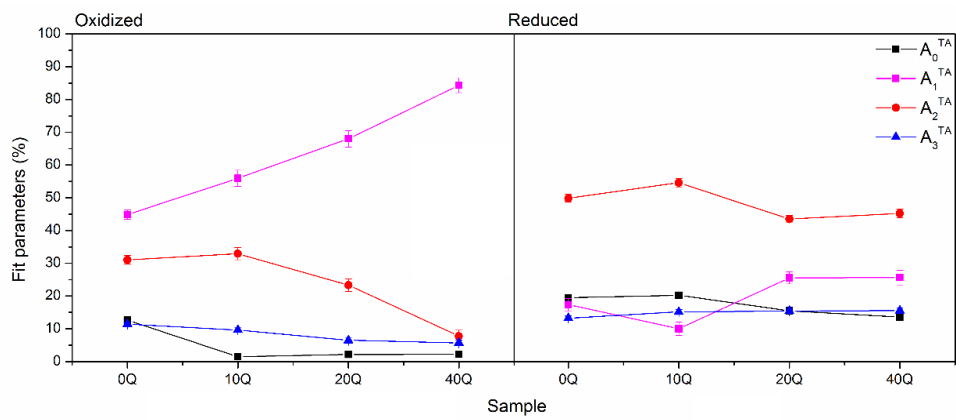
Figure 59. TA decay amplitudes for all samples in oxidised (left) and reduced (right) states.

Figure 59 shows the amplitude associated with each decay component for each sample in both oxidised and reduced states. For oxidised samples, increasing the ratio of Q2NS to QDs increases the amplitude associated with τ_1^{TA} at the expense of those associated with τ_2^{TA} and τ_3^{TA}, indicating that it is τ_1^{TA} that is associated with the electron transfer process from the CBM of the QD to oxidized Q2NS. For reduced samples, decay parameters are largely unaffected by Q2NS:QD ratio, indicating that this electron transfer process is suppressed.

To study the energy dependence of the charge transfer process, absorption transients for both oxidised and reduced samples 0Q and 40Q were obtained for pump photon energies of 2.75 eV and 2.58 eV, corresponding to pump wavelengths of 450 nm and 480 nm, respectively; these results are summarised in figure 60.
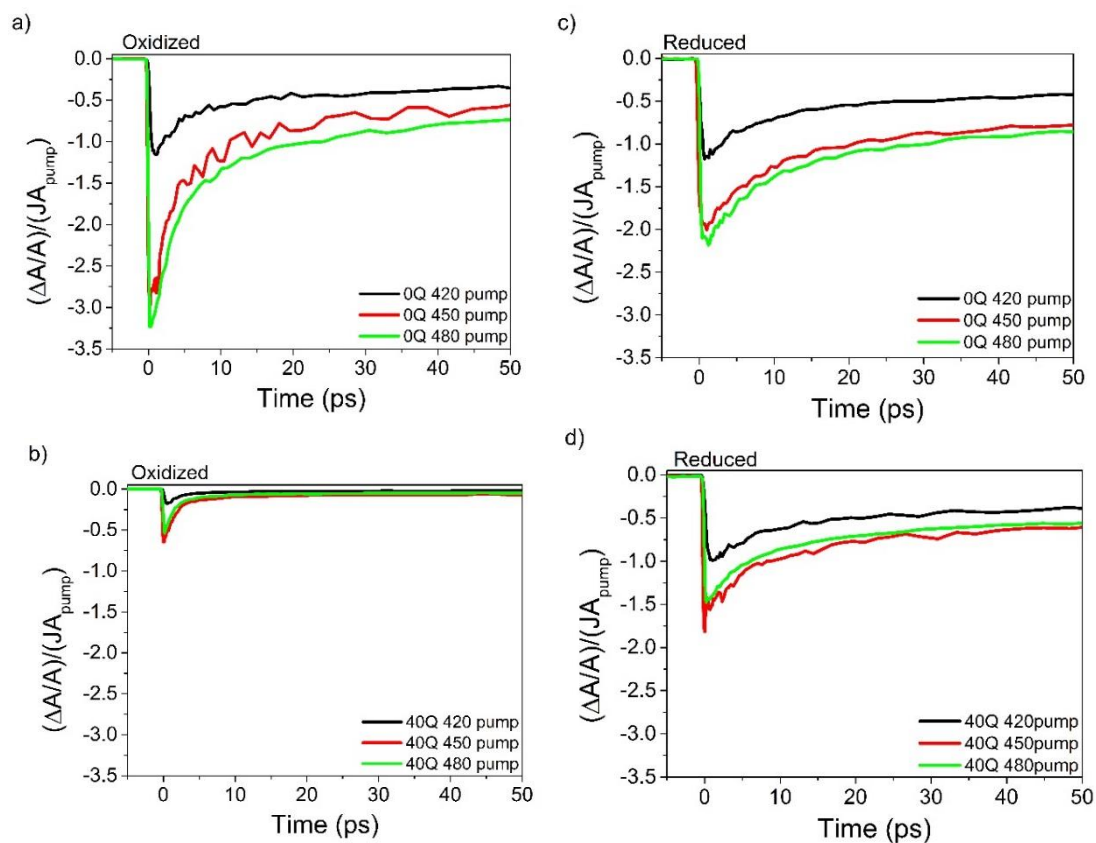
Figure 60. Fractional changes in absorption for samples a) 0Q in oxidized state, b) 40Q in oxidized state, c) 0Q in reduced state and d) 40Q in reduced state. Traces normalised by controlling absorbed photon flux density, JA_{pump}, to 1.7 x 10^{12} photons cm^{-2} per pulse.

The peak bleach for the oxidised 40Q sample compared to the oxidised 0Q sample is reduced approximately 6-fold, independent of pump wavelength. This indicates that transfer to the Q2NS by hot electrons is competes with cooling to the CBM, which reduces the number of electrons reaching the CBM. However, for both the oxidized 40Q and 0Q samples the peak when pumping at 420 nm is about one–third of that obtained when pumping at 450 nm or 480 nm. This indicates that significantly fewer electrons cool to the band edge after being initially excited to this higher energy state, suggesting the presence of a "hot" trapping process, accessible when pumping at higher energies, which later results in transfer to the quinone. After reduction of the quinones, the transients for 40Q and 0Q are largely similar, indicating that the electron transfer to the quinones has been switched off, both for "hot" transfer, as well as transfer from the CBM. For both 0Q and 40Q, in the reduced state, the peak bleach when pumped at 420 nm is now approximately two-thirds that when pumped at 450 nm or 480 nm. This suggests that the hot trapping mechanism allows later transfer to the quinones; reducing the quinones prevents transfer of electrons from traps, and a larger

fraction of these trapped electrons can now cool to the band edge. Additionally, the initial amplitudes of the reduced samples when pumped at either 450 nm or 480 nm were reduced compared to the oxidized 0Q, by a third and half for the reduced 0Q and 40Q, respectively. This is attributed to the effect of the reducing agents on the hot trapping process, which has been shown previously to be sensitive to surface treatments,[45, 117] also indicating the occurrence of some hot trapping when pumping at 450 nm and 480 nm.

4.8 Cyclic voltammetry of conjugates

As discussed in section 1.3.5, in order for efficient electron transfer to take place between the CBM of a QD and an external acceptor, the LUMO of the acceptor must lie energetically between the CBM and VBM. Additionally, for theoretical calculation of transfer timescales, it is important to have accurate estimates for the energies of the states involved; in this case the donor state is one associated with the QD, and the acceptor is the LUMO of Q2NS. A good approximation for the LUMO is the redox potential as determined by cyclic voltammetry.[169-171]

To estimate the LUMO of oxidised Q2NS, cyclic voltammetry was performed on the 40Q sample in order to determine the redox potential of Q2NS in its QD-bound conformation, using methods described in section 2.10. A cyclic voltammogram obtained at a scan rate of 50 mVs^{-1} is shown in figure 61. Peak anodic and cathodic currents were observed at 0.36 V and 0.56 V versus the normal hydrogen electrode respectively. Although redox of Q2NS is expected to be a two-electron process, only single peaks were observed. This is explained by the expected instability of the semi-reduced intermediate; a similar situation to the analogous ubiquinone/semiubiquinone/ubiquinol. The calculated redox potential is the average position of these two peaks, and is found at V° = 0.46 V vs NHE. This is higher than the value for the analogous ubiquinone-ubiquinol, which has reduction potential V° = 0.04 V Converting to vacuum level to find the estimated LUMO gives E$_{LUMO}$=-4.90 eV. This lies within the band gap of both bulk CdTe and CdS (as shown in figure 62) and therefore will do so for QDs, where the band gap is wider due to size confinement effects.
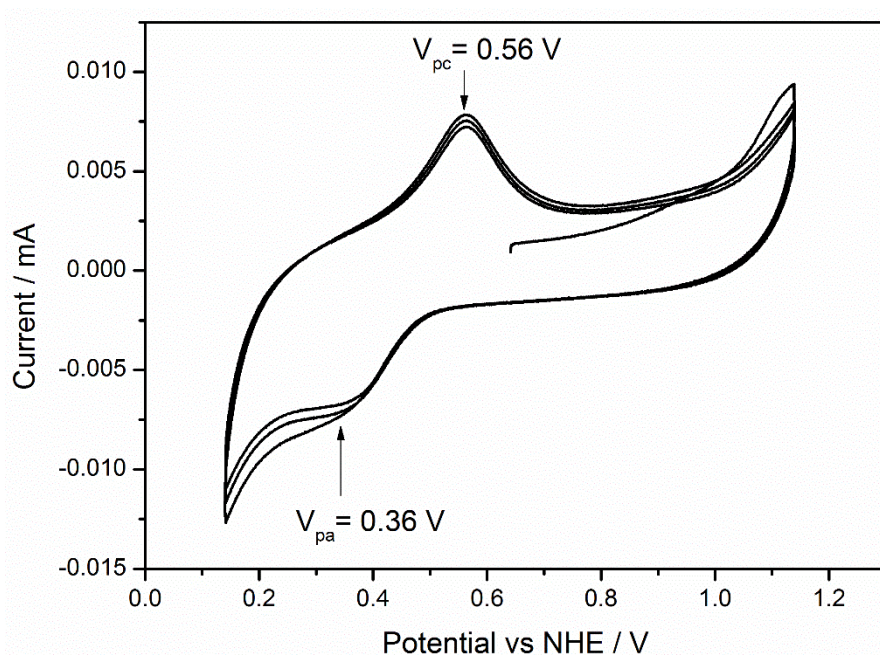
Figure 61. Cyclic voltammogram of sample 40Q obtained vs mercury/mercurous sulphate

electrode, presented vs normal hydrogen electrode potential.
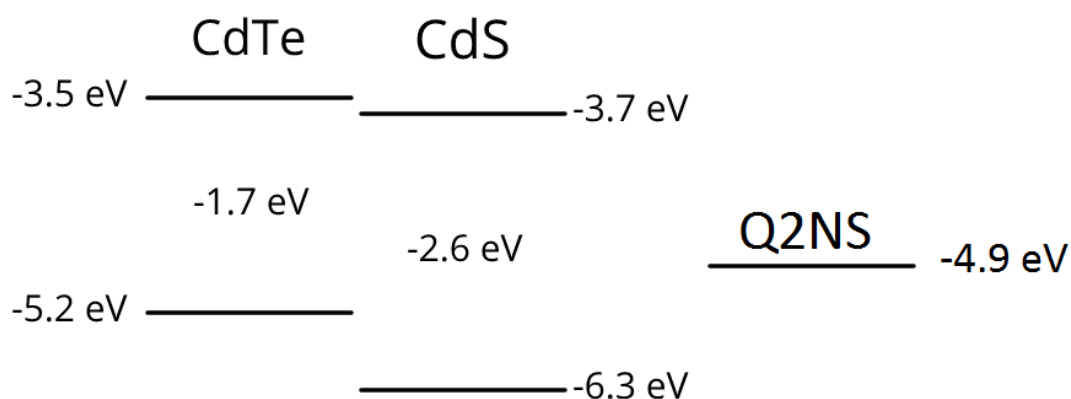
Figure 62. Band structure alignments for bulk zinc blende CdTe and CdS, with redox

potential of Q2NS. The redox potential of Q2NS lies within the band gap (which will be

wider for QDs) which enables it to accept photoexcited electrons.

4.9 Atomistic Semiempirical Pseudopotential Calculations

To gain further insight into the nature of the electron transfer process, calculations for transfer times for a simplified CdTe core QD-acceptor system were performed within the framework of the atomistic semiempirical pseudopotential method.[172] The QD core was represented by a CdTe core particle of radius 3 nm. To ensure the absence of any electronic coupling between QD and acceptor, the "linker" part of Q2NS was modelled as a one-atom-thick arm made of a zinc blende semiconducting material with a band gap much greater than

that of CdTe. The oxidised Q2NS was modelled, according to an established procedure,[159] as a localised acceptor state positioned at the end of the linker, whose energy coincided with the experimental estimate for the lowest unoccupied molecular orbital (LUMO) of Q2NS. For direct transfer of an electron from the CBM, calculated transfer times are of the order of nanoseconds, and increase for electrons excited to higher energy states. These transfer times are significantly longer than what is observed from TA measurements. Transfer times from a simulated surface trap state, however, agree closely with those observed. Depending on the relative position of the simulated trap state and attached acceptor, predicted transfer times range from a few (2-8) ps for the shortest distance trap, to tens (40-70) of ns for the furthest, covering all values in between. The transfer times are calculated assuming an Auger-mediated process, whose rates depend on the dielectric constant of the nanocrystal's environment. This process involves transfer of energy from the excited electron to VB holes, and is thought to be much faster than direct electron transfer for electrons resident in surface traps.[159] Dielectric constants ranging from 2.5 to 6 were considered, in order to represent the effects of ligands, solvents and shell material. The variation in the calculated transfer times for each particular distance accounts for this variation in dielectric environment. These simulations strongly suggest transfer to the Q2NS is dominated by a stepwise process involving an intermediate surface trap state. Despite the simplicity of this approach, where the linker is replaced by an atomic chain made of an insulating material and the electron acceptor is modelled only through the position of its LUMO, the calculated transfer rates reproduce the observed trends, particularly when considering the large number of quinones per QD.

4.10 Concluding remarks

These observations discussed in this are consistent with a step-wise electron transfer process. Regardless of the presence of Q2NS, hot electrons can be trapped in a localised QD state, at an energy that lies above the CBM, rather than cool directly to the band edge. Such trapped electrons can (i) cool to the band edge, (ii) non-radiatively recombine or (iii) transfer to an oxidized quinone (if present). The latter process is able to largely outcompete the others. Electrons that have reached the CBM can also transfer to an oxidised Q2NS, or can recombine, either radiatively or non-radiatively. These processes are summarised in figure 63
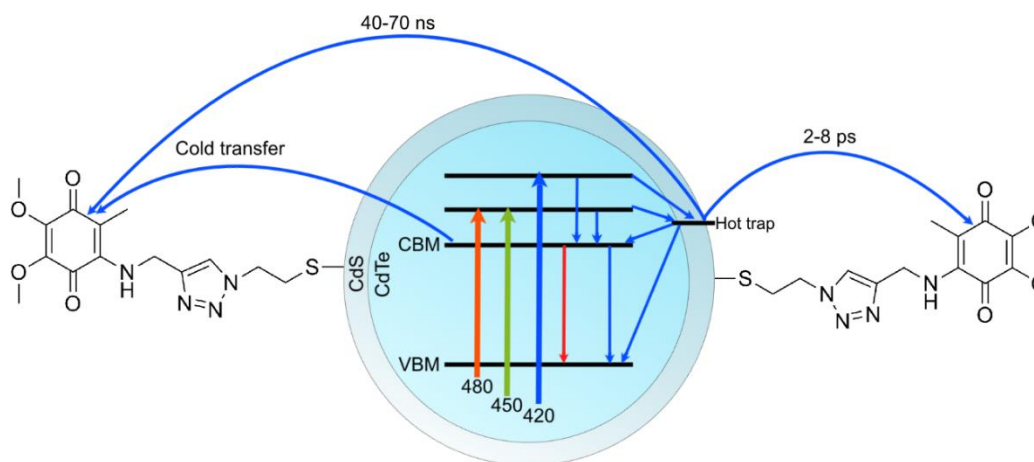
Figure 63. Schematic diagram of quantum dot energy levels and possible charge excitation and relaxation processes.Thin blue lines represent non-radiative processes, and the thin red line represents radiative recombination. Pumping at 2.95 eV (420 nm) allows efficient electron transfer to attached Q2NS via a high-lying intermediate surface trap state. The efficiency of this transfer is strongly dependent on the spatial separation of the attached Q2NS acceptor and trap state donor.

In conclusion, data from TA and transient PL experiment showed that electron transfer from colloidal CdTe/CdS QD to a surface bound electron acceptor is possible both by "hot" electrons and those that have cooled to the CBM. Analysis of the absorption bleach at varying wavelengths implicates a particular hot trap state that exhibits efficient transfer to the Q2NS. Transfer timescales predicted by calculations within the framework of the semiempirical atomistic pseudopotential method concur with these experimental observations. Upon chemical reduction of Q2NS, electron transfer from the QD is seen to be suppressed, so electrons cool to the band edge and undergo recombination as normal. Employing this bimodal electron transfer route greatly increases the quenching efficiency of the QD-acceptor system vs other QDs (as measured by comparison of per-quinone quenching efficiency) and extends their applicability as a useful biosensor. In addition to this, the new insight that hot trapped electrons can be efficiently extracted from the QDs using this organic molecule may have important consequences for other semiconductor industries, particularly in photovoltaics where charge extraction is one of the main barriers to improved solar cell efficiency.

5 Redox Sensitive QDs in Cells

The previous chapter discussed the synthesis and characterisation of a QD redox sensor consisting of a CdTe/CdS QD conjugated with the quinone molecule Q2NS. This chapter discusses the interaction of these CdTe/CdS QDs and their conjugates with Q2NS to MCF-7 cells, a breast cancer cell line. These cells were chosen as they are easy to grown and maintain, and display a particularly reduced redox environment.[173]

A major hurdle in the development of nanoparticle redox sensors is achievement of non-endocytic uptake, as well as determination of the location of the nanoparticles within the cell. With this in mind, a number of strategies for achieving uptake of the CdTe/CdS QDs are detailed here. The first, and simplest strategy involves the use of amine-terminated stabilising ligands (cysteamine) for the QDs. This may be expected to facilitate uptake in two ways: firstly, the net positive charge of the amine-functionalised QDs may improve uptake due to electrostatic attraction to the negatively-charged plasma membrane. Secondly, the proton-sponge effect exhibited by amine-rich species may allow for endosomal escape.

As detailed in section 1.6, cell-penetrating peptides (CPPs) are often used effectively for transfection of small molecules, and have been shown to improve delivery of nanoparticles into cells. Section 5.5 details the use of the CPP TAT-c for improvement of uptake of QDs into cells, and determination of the QDs fate.

The final method used for encouraging uptake was via cell squeezing, using protocols detailed in section 2.8.5. Experiments were performed using QDs with and without Q2NS.

A QD redox sensor of the type discussed here will be effective for a particular cell type if enough of the surface-bound Q2NS is reduced that PL recovers from the quenched, oxidised state. However, if all the Q2NS is reduced, the PL will be maximised, and the sensor will be unable to resolve changes in the redox potential. Here, work to ascertain the effectiveness of the Q2NS-conjugated QDs as redox sensors for MCF-7 are performed.

The aims for the work detailed in this chapter are as follows:

- Determine whether cysteamine-capped CdTe/CdS QDs escape endosomes after endocytosis by MCF-7.
- Determine whether TAT-c can allow enhanced uptake of QDs into MCF-7 cells, and determine fate of QDs after uptake.

122

- Use cell squeezing to achieve non-endocytic uptake, and then determine whether Q2NS-conjugated QDs are an effective redox sensor for MCF-7 using the criteria outlined above.

5.1 QD Synthesis

Red-emitting cysteamine-stabilised and orange-emitting TGA-stabilised CdTe/CdS core/shell QDs were synthesised as described in sections 2.1.1 and 2.1.2, and suspended in HEPES buffer (Sigma) with pH adjusted to 7.2. Optical spectroscopic data obtained for these QDs is given in figures 64 and 65. The QDs displayed the expected optical properties, with narrow emission and relatively broad Stokes shift. From absorption data, estimates for the average diameters of the QDs were calculated at 3.4 nm and 3.3 nm for the TGA- and cysteamine-stabilised QDs respectively (procedure detailed in the previous section). The zeta potentials were measured as -39 mV and +32 mV for the TGA- and cysteamine-stabilised QDs respectively, consistent with colloidally stable QDs. A summary of optical properties, as well as measured zeta potentials is available in table 3.
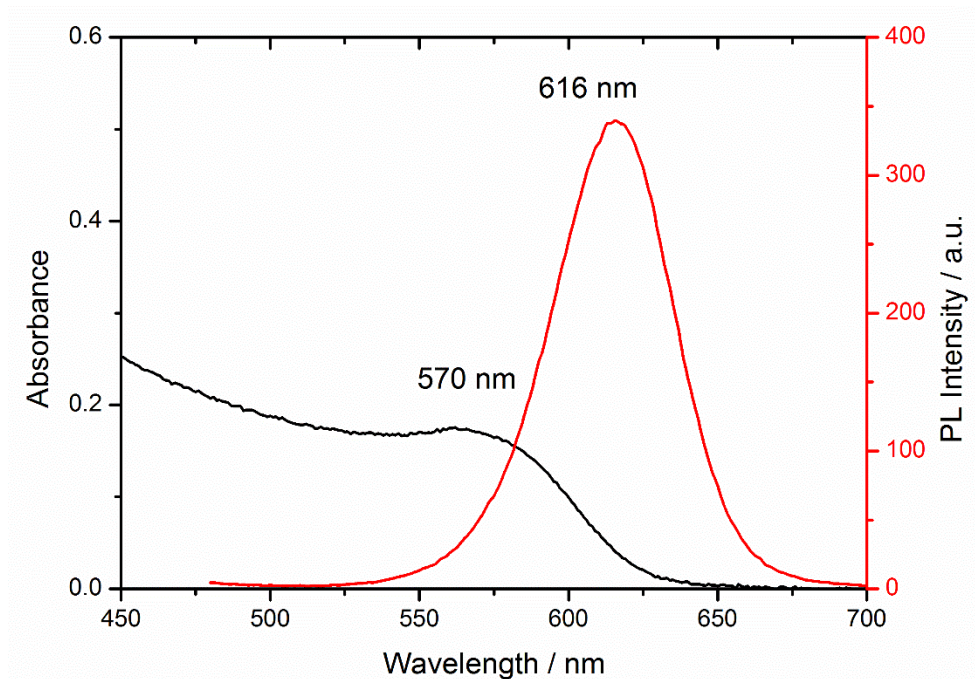
Figure 64. UV-Vis absorbance (black) and photoluminescence (red) spectra for red, cysteamine-stabilised CdTe/CdS core/shell QDs.
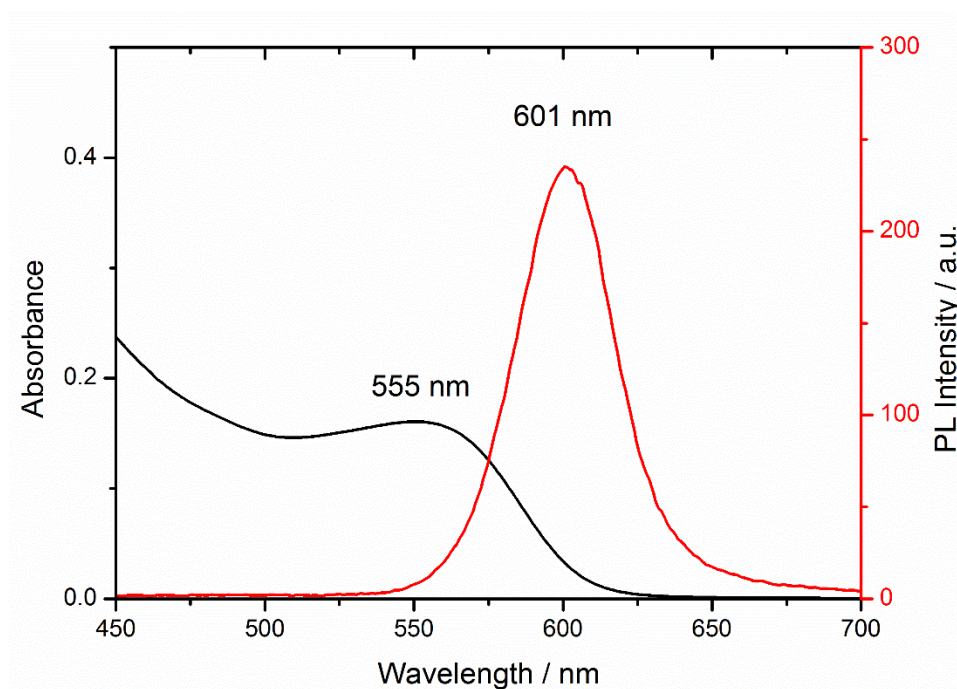
Figure 65. UV-Vis absorbance (black) and photoluminescence (red) spectra for orange, TGA-stabilised CdTe/CdS core/shell QDs.

QD	1st Excitation	Emission max	PLQY	Estimated size	Zeta potential
TGA-CdTe/CdS	555 nm	601 nm	46%	3.4 nm	-39 mV
Cysteamine-CdTe/CdS	570 nm	616 nm	42%	3.3 nm	+32 mV

Table 3. Summary of physical properties of TGA- and cysteamine-stabilised CdTe/CdS QDs used in cell experiments.

5.2 Viability Studies

An effective biosensor must not be highly toxic in the environment for which it is designed to be used. As mentioned in section 1.6, Cd-containing QDs have been shown to exhibit toxicity due to "leeching" of Cd into the cytosol. In addition, generation of reactive oxygen species at the surfaces of optically-active nanoparticles may also contribute to cell malfunction and death.[174] However, small doses of QDs may exhibit low enough toxicity to cancer cells to avoid their preclusion as effective redox sensors. Viability studies for both TGA-and cysteamine-capped QDs were performed to assess cytotoxicity of the QDs, using methods outlined in section 2.8.2. The results are summarised in the following figure 66.
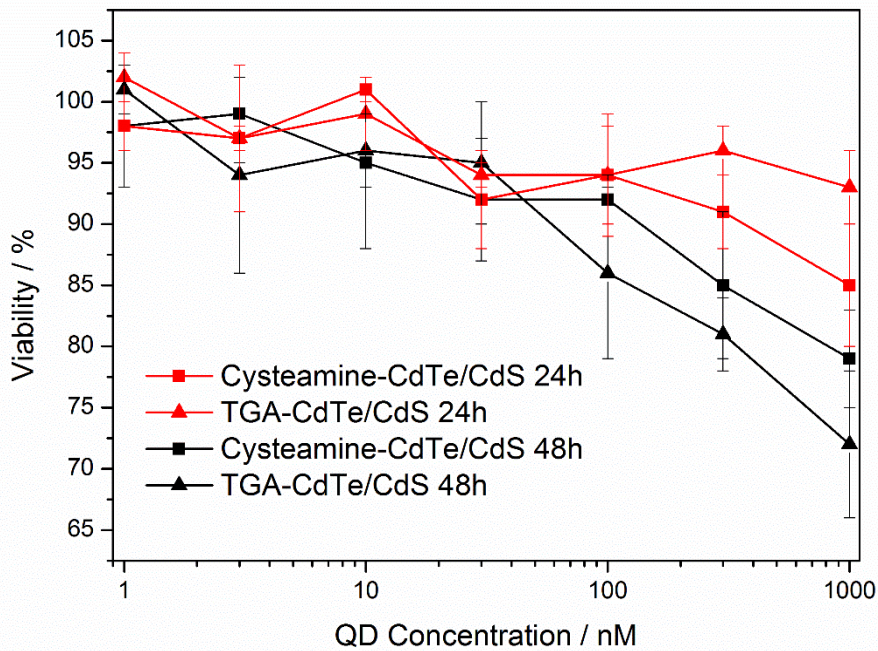
Figure 66. Viability of MCF-7 cells after 24 (red) and 48 (black) hours incubated with varying concentrations of TGA- and cysteamine-capped QDs. For both timescales, toxicity remains low until the concentration is increased to around 100 nM. For higher QD concentrations, toxicity is increased for longer timescales.

For small and intermediate concentrations (1-30 nM) viability remains high (>95%) for both 24 hour and 48 hour incubations with both QD types, consistent with low toxicity. For higher concentrations (100-1000 nM) toxicity begins to increase, and viability is reduced to around 75-80% after 48 hours, for both QD types. However, for shorter times, the toxicity still does not increase dramatically. This suggests that toxicity is largely due to slow leeching of toxic Cd into the cell. The QD concentrations necessary to obtain this toxicity, however, are very high (typical experiments use QD concentrations of 0.1-10 nM) and so we can conclude that for these cells, the QDs have limited toxic effects over the intended concentration range.

5.3 Passive Uptake of QDs

Both the TGA- and cysteamine-capped CdTe/CdS QDs were incubated with MCF-7 cells at varying concentrations, to determine whether the cysteamine-capped QDs would escape endosomes via the proton-sponge effect, as described in section 1.6. To this end, the experiments with TGA-capped QDs were performed as control.

5.3.1 Cysteamine-capped QDs

Cysteamine-capped QDs were incubated for 24 hours at concentrations of 0.1-10 nM with MCF7 cells as detailed in methods section 2.8.3 and then washed with DPBS. Confocal microscopy shows uptake of QDs into the cells, evidenced by bright, uniform fluorescence, as shown in figure 67.
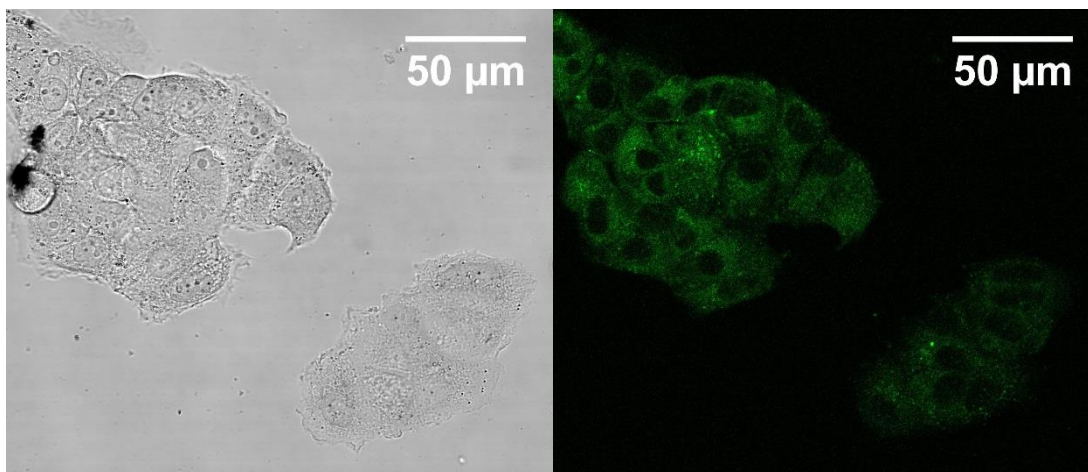
Figure 67. Bright field (left) and confocal fluorescence image (right) of MCF-7 cells incubated with 3 nM cysteamine-capped CdTe/CdS QDs. Bright fluorescence, co-localised with the cell is evidence for uptake of QDs by the cell.

To determine whether QDs had escaped from endosomes, an immunostaining study was performed in a separate experiment, as described in methods section 2.8.6. A representative image is presented in figure 68. Nuclear staining by Hoescht 33342 shows that QDs remain outside of the cell nucleus. By comparison of signals from the QDs and Alexa-416-conjugated EEA-1 (which stains endosomes), the QDs are almost completely co-localised with endosomes, which indicates that endosomal escape has not occurred. There are some areas on each image which show the presence of QDs not associated with EEA-1. This shows that the observed co-localisation is not merely an artefact due to crosstalk between the emission of the QDs and Alexa-416, however these areas are typically outside of the cells, and are thought to be due to aggregates of QDs in the solution which have not been endocytosed or washed away.
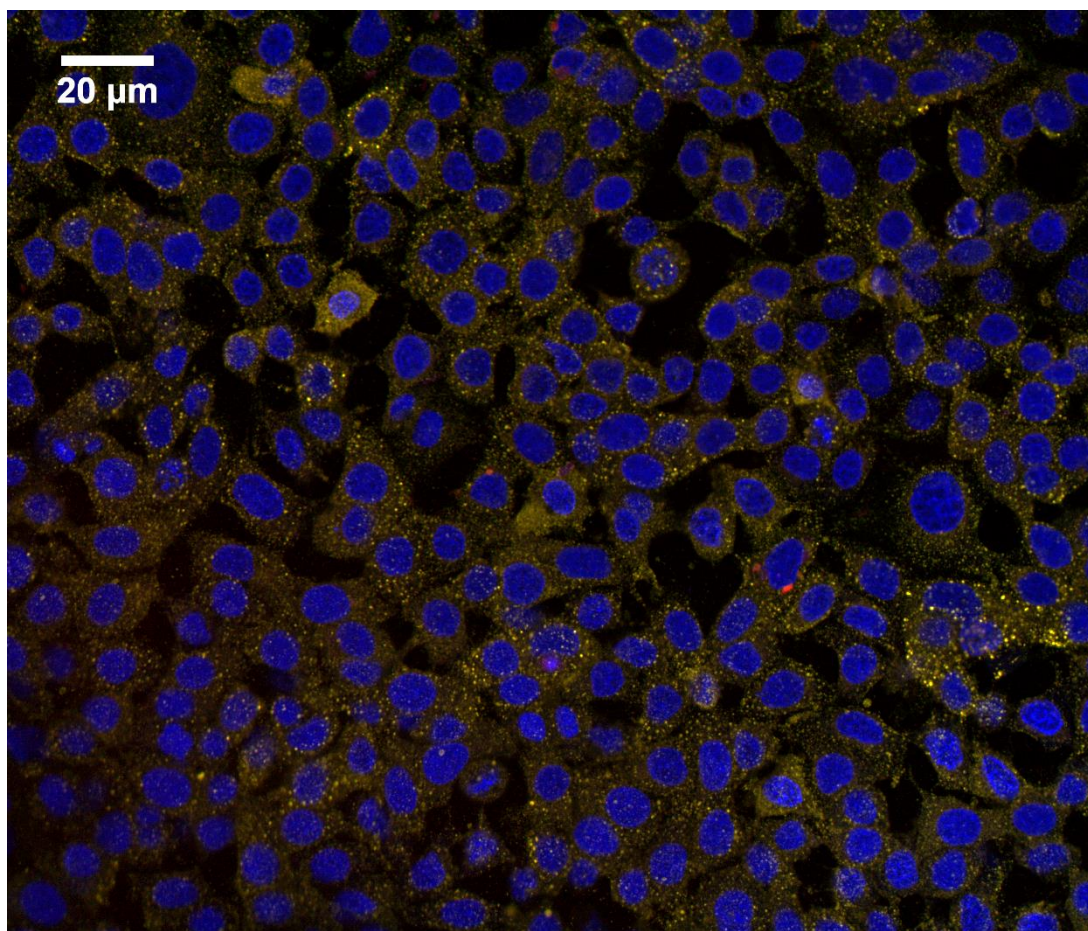
Figure 68. Confocal fluorescence image of fixed MCF-7 cells stained with Hoescht 33342 (blue) cysteamine-capped QDs (red) and Alexa-416-goat-EEA-1 (green). Almost total co-localisation of red and green channels is observed.

5.3.2   TGA-capped QDs

The same experiments were performed for the TGA-capped CdTe/CdS QDs, with largely the same results: bright emission was observed from the QDs within cells, shown in figure 69. However, immunostaining with EEA-1 (figure 69) showed that QDs were completely co-localised with endosomes, suggesting that the QDs are universally within endosomes after 24 hour incubation. This is not an unexpected result, as there is no known reason these QDs would necessarily be capable of endosomal escape.
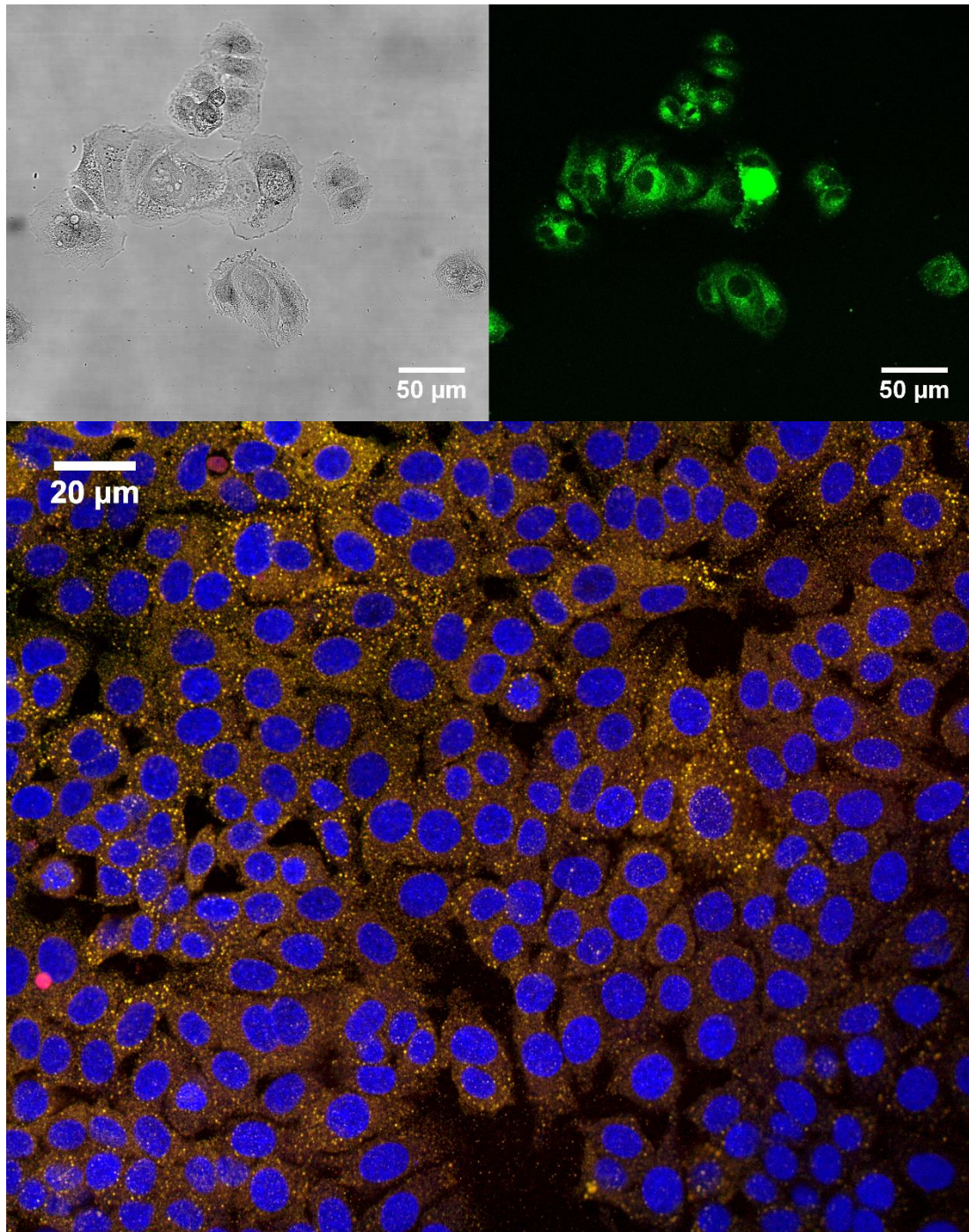
Figure 69. Top: Bright field (left) and confocal fluorescence image (right) of MCF-7 cells incubated with 3 nM TGA-capped CdTe/CdS QDs. Bottom: Confocal fluorescence image of fixed MCF-7 cells stained with Hoescht 33342 (blue) cysteamine-capped QDs (red) and Alexa-416-goat-EEA-1 (green), showing co-localisation of QDs and EEA-1.

5.3.3   Q2NS-Conjugated TGA-QDs

In the previous section, it was established that the TGA-conjugated CdTe/CdS QDs reside within endosomes after being taken up by the MCF-7 cells. The result of this is that sensors based on these QDs are unlikely to be useful in chemical sensing within the cytosol, if taken up by endocytosis. However, they will be useful in sensing of redox biology involved in the endocytic pathways, an area critically important to scientists working in the fields of drug delivery and discovery.[175-177]

A preliminary study was therefore performed to determine whether the endocytic environment possesses sufficient reductive capability to switch on the luminescence of the Q2NS-conjugated QDs, which would confirm their viability as a redox sensor in this context.

Q2NS-conjugated TGA-stabilised CdTe/CdS were synthesised, from the same stock as used in the uptake experiment, with a Q2NS:QD ratio of 20:1 (40Q, using notation from the previous chapter). Emission spectra of these QDs in both oxidised state (as expected from QDs in ambient lab conditions) and reduced state (reduced by addition of sodium ascorbate and sodium dithionite, detailed in section 4.5) are shown in figure 70.
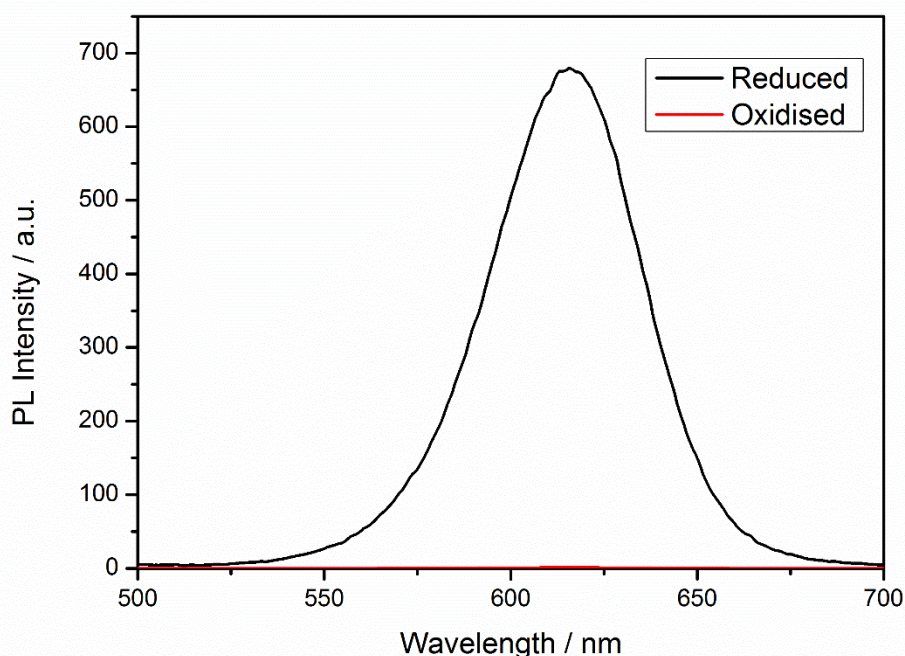
Figure 70. Emission spectra of Q2NS-conjugated (40Q) TGA-stabilised CdTe/CdS QDs, as used in uptake experiments, in oxidised (red) and reduced (black) states.

The resulting QD-Q2NS conjugates exhibit peak PL intensity that is almost completely quenched. Addition of reducing agent, as before, results in recovery of the PL to a large measurable value, in keeping with previously discussed observations.
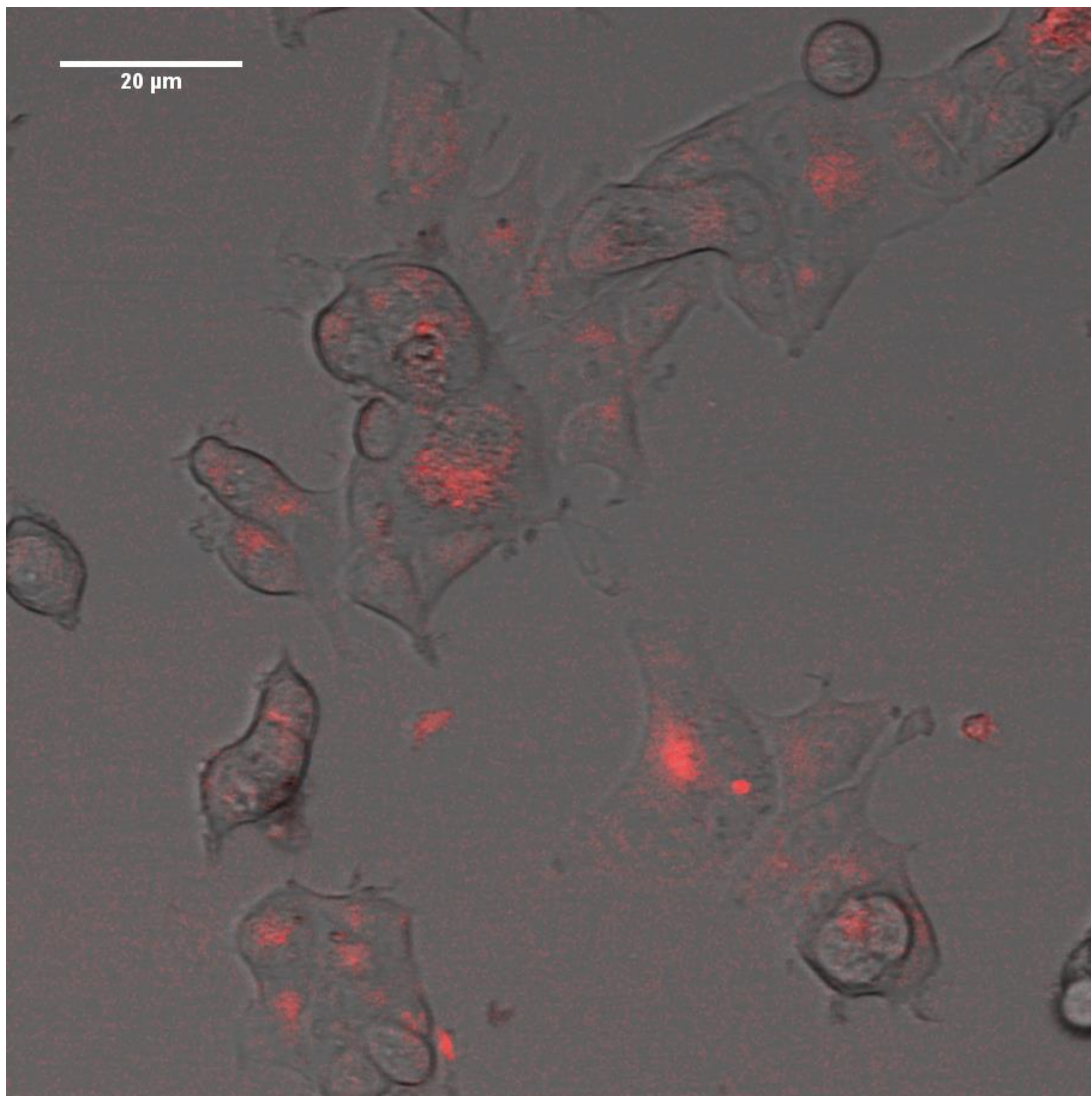
Figure 71. Epifluorescence image of (red) overlaid with bright field optical micrograph (greyscale) of MCF-7 incubated with 3 nM Q2NS-QD conjugates (40Q). Fluorescent signal indicates switch-on of the QDs PL by the reducing conditions within endosomes.

Cells were incubated with the redox-QDs as reported in section 5.3.1. Epifluorescence images of the cells post-incubation show strong red fluorescence, indicating that the redox environment within the endosomes is sufficient to reduce the Q2NS of the QDs, in turn indicating that these Q2NS-QD conjugates are a viable tool for measuring redox during the endocytic pathway.

5.4   Cell Squeezing

In the previous section, the redox-QDs were shown to be reduced within cells, albeit within endosomes (or later vehicles of the endocytic pathway). However, it is desirable to design a sensing strategy that allows measurement of the redox environment within the cytosol. For QD sensors, this means achieving QDs in cells that are not contained within any sort of vesicle, especially as a result of endocytosis.

Cell squeezing was employed to achieve non-specific, non-endocytic delivery of the TGA-capped CdTe/CdS QDs into cells (both with and without the redox sensing functionality imparted by Q2NS) according to procedures detailed in section 2.8.5.
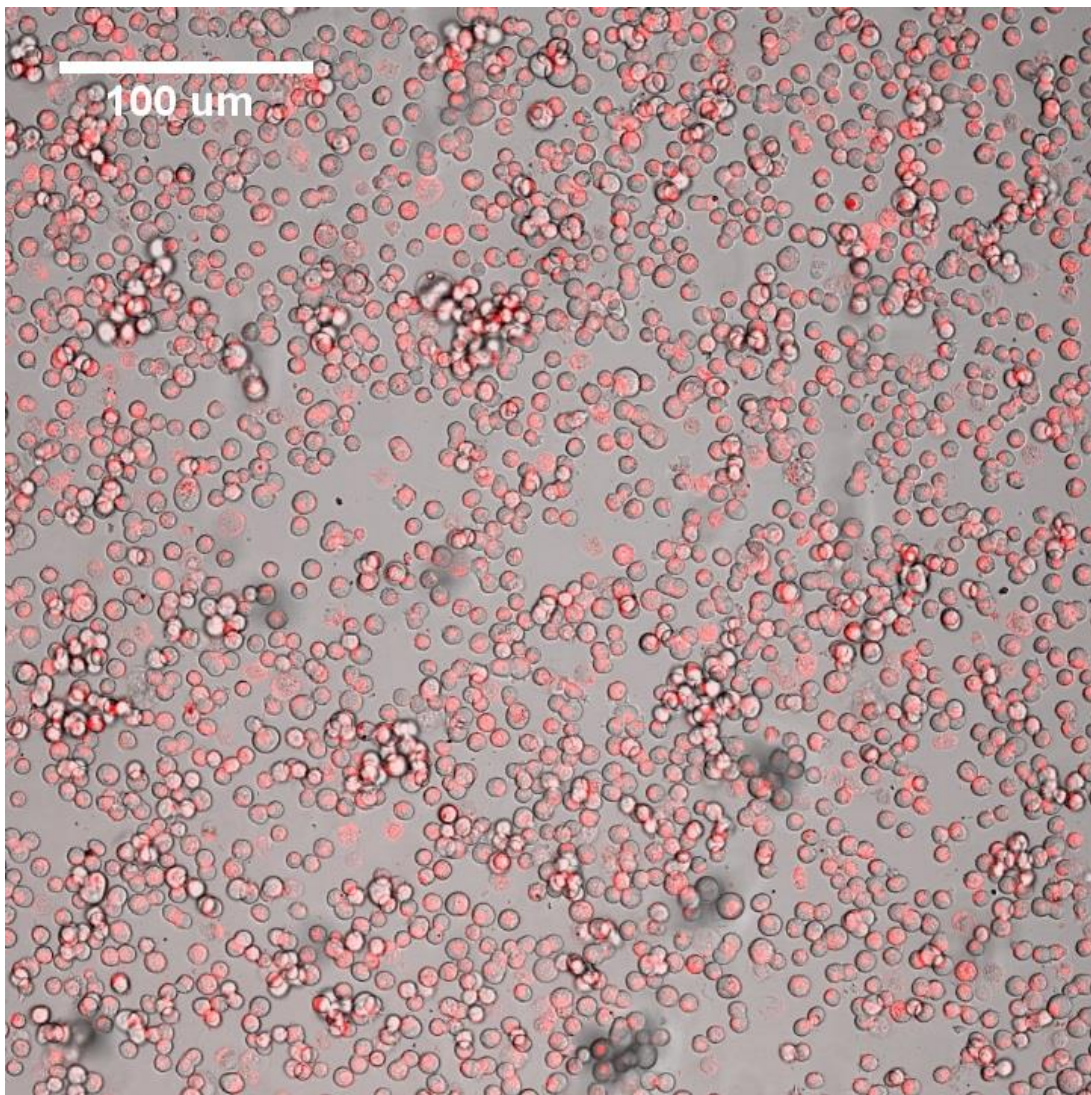
Figure 72. Example low-magnification confocal fluorescence image of MCF-7 cells squeezed with Q2NS-conjugated CdTe/CdS QDs. Red fluorescence indicates presence of reduced QD sensors.

To assess the effectiveness of the cell squeezing technique in achieving delivery of QDs into cells, MCF-7 cells were squeezed in the presence of 100 nM QDs and left for 30 mins. A control sample was processed in parallel, with the squeezing step omitted. Figure 73 shows a scatter plot of measured total PL intensity per cell vs cell radius. The squeezed and control cells are observed in two distinct populations, with the squeezed cells exhibiting a two-fold increase in PL emission per cell. This is concluded to be due to improved uptake of QDs by the cells.
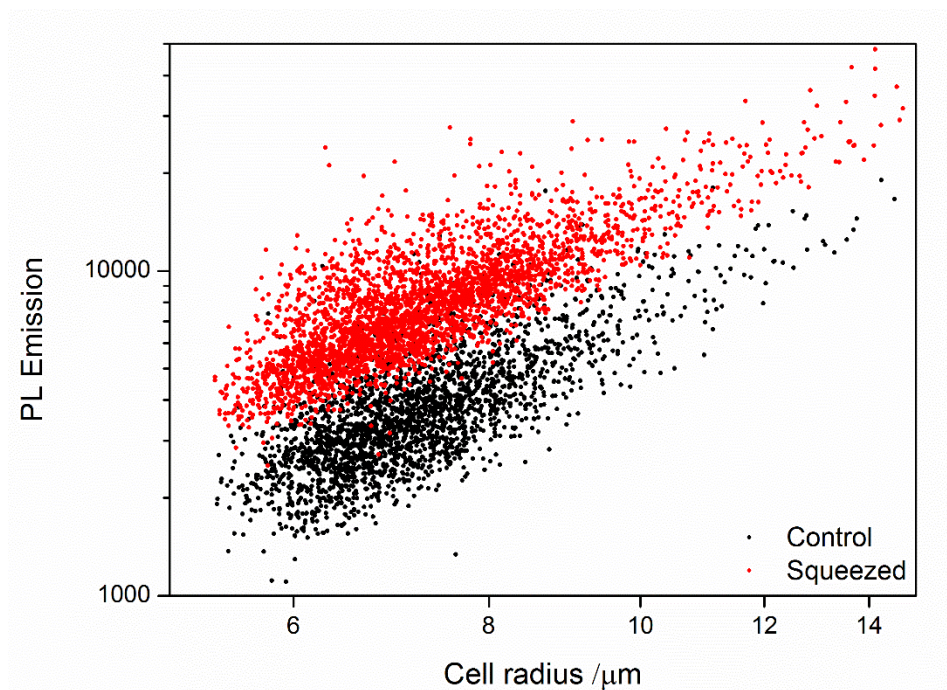
Figure 73. Scatter plot of total PL intensity per cell vs cell radius, as determined by confocal fluorescence microscopy, for cells squeezed with QDs (red) and control (black) where no squeezing was performed.

TEM images (figure 74) of microtomed slices of squeezed MCF-7 cells show QDs dispersed throughout the cytosol of the cell, as well as a small number or QD aggregates within endosomes. This is direct evidence of the success of non-specific uptake of QDs through the transient pores caused by mechanical deformation. It is, however, difficult to quantify the proportion of endocytosed QDs by STEM; the QDs that are in endosomes are typically aggregated and are therefore difficult to individually count.
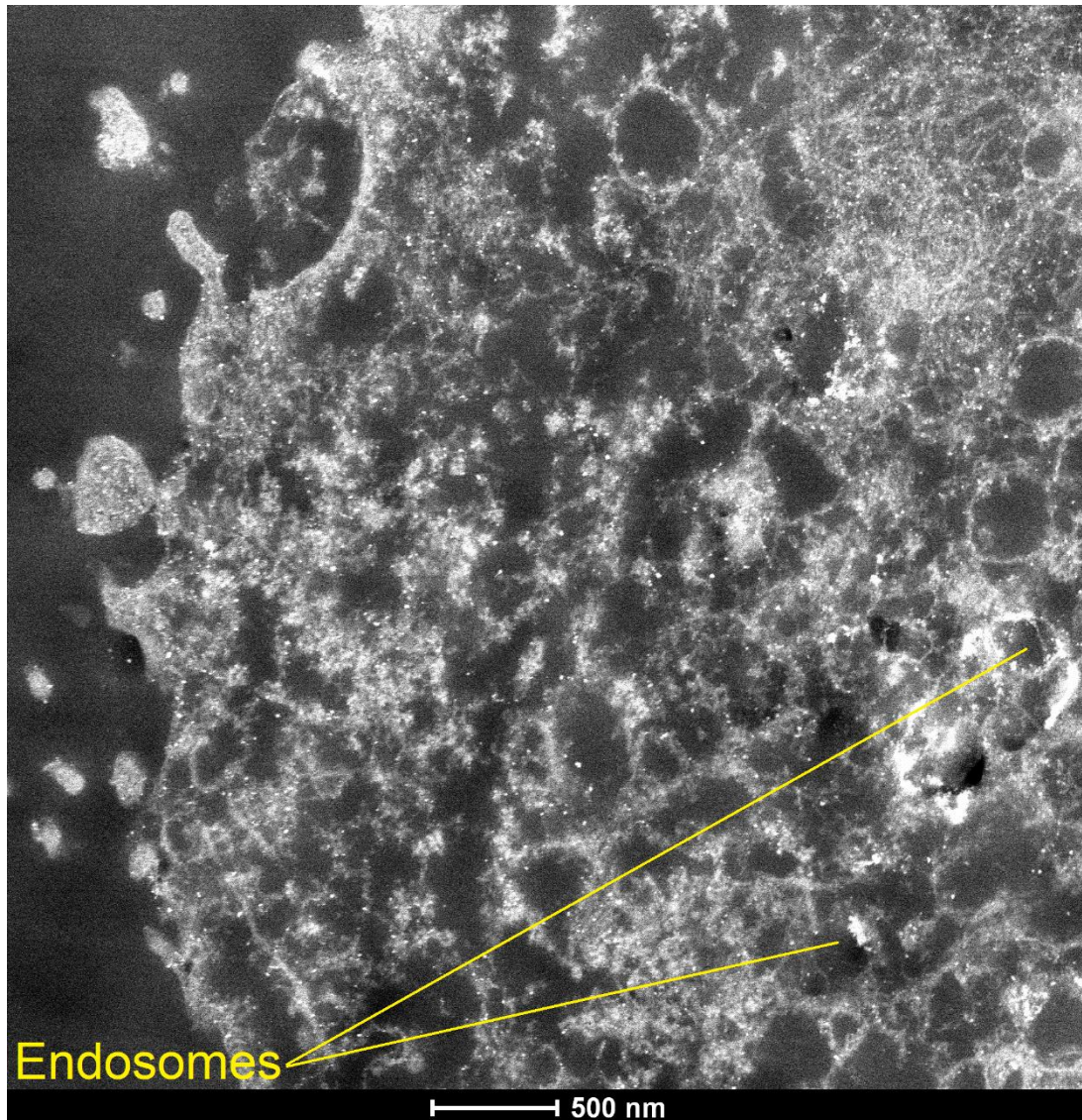
Figure 74. STEM image of slice of fixed MCF-7 cell after squeezing with QDs. QDs are visible as bright spots throughout the cytosol. Some endosomes containing aggregates of QDs are also visible (bottom right).

The improved uptake for the squeezed cells (compared to the control sample) is attributed to non-specific, diffusive uptake of QDs, which is likely to result in the majority of QDs populating the cytosol of the host cell. However, there is still a significant PL signal measured from the control cells, suggesting endocytosis is still taking place, even over the short timescales and relatively low temperatures that the cell squeezing experiments are performed at. Another possible explanation for the significant PL signal from non-squeezed cells is that QDs have become adhered to the cell surface, and have not been removed by washing. The relatively small number of QDs observed in endosomes supports this idea.

In any case, it can be concluded that the cell squeezing achieves a significant number of cytosol-borne QDs per cell. With this in mind, the cell squeezing experiment was performed with the redox-sensing Q2NS-conjugated CdTe/CdS QDs, using the same protocols. Figure 75 shows a scatter plot of PL intensity per cell vs cell radius for cells squeezed with Q2NS-conjugated QDs (red) and control QDs (black).
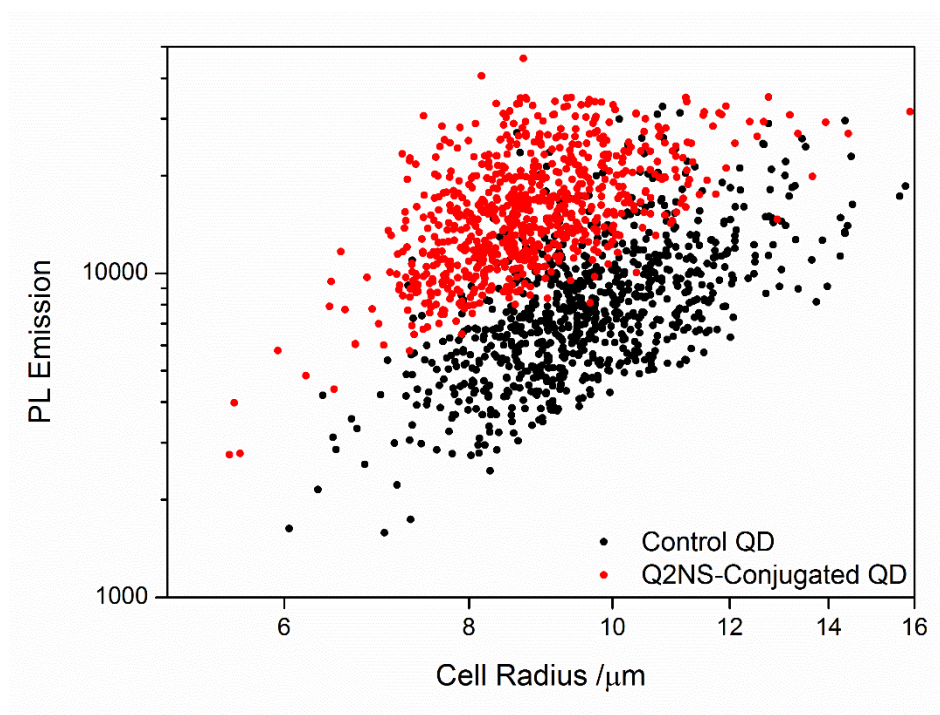
Figure 75. Scatter plot of total PL intensity per cell vs cell radius, for cells squeezed with 100 nM Q2NS-conjugated QDs (red) and control QDs (black).

Two populations are again observed. Surprisingly, the redox-sensitive QDs exhibit greatly-improved PL in relation to their non-redox sensitive counterparts. This is not expected to be a result of higher rates of uptake for the redox-QDs; the relatively small population of Q2NS relative to the other capping agents (TGA) is not expected to make a large effect on the surface or colloidal properties. Instead, the improved PL per cell from the redox-QDs is attributed to the enhancement in fluorescence observed when the capping Q2NS is fully reduced (as thoroughly explored in the previous chapter). Although more studies must be performed in this area, it is therefore likely that the quinones of the redox sensitive QDs are fully reduced within MCF-7 cells. Further study could be performed on cells with a less-reducing cytosolic redox environment, or with QDs conjugated to a ligand with increased reduction potential.
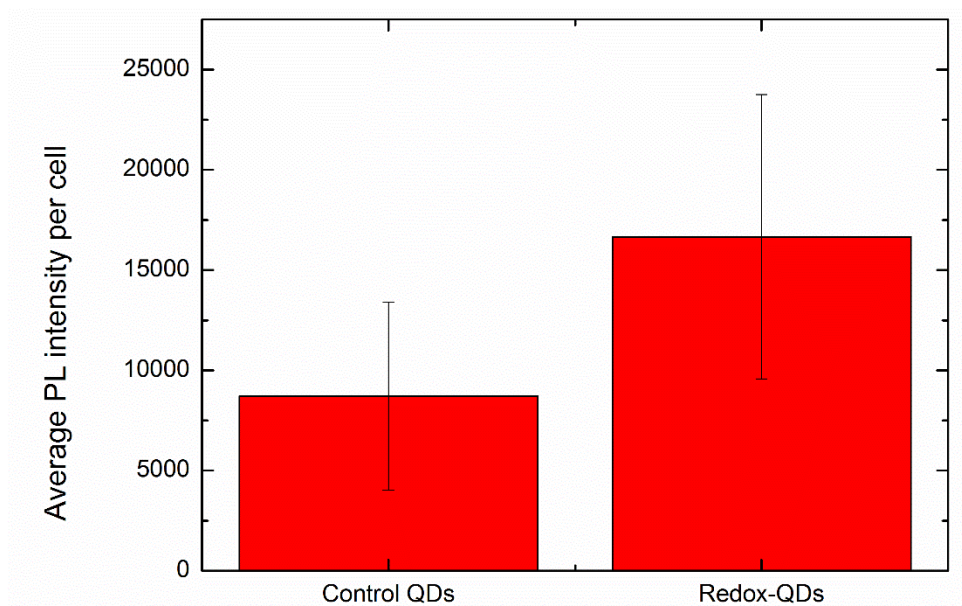
Figure 76. Average PL intensity per cell for cells squeezed with control (left) and redox-sensitive Q2NS-conjugated QDs (left). Error bars represent the standard deviation.

5.5   Cell-penetrating peptides

Cell-penetrating peptides (CPPs) have been applied for transfection or delivery of a broad variety of cargo, from DNA to large proteins.[178-180] The CPP TAT-c is a particularly common example due to its small size and synthetic simplicity, and has been demonstrated to enhance uptake of nanoparticles in literature studies.[181-183] Importantly, the peptide possesses a thiol-containing cysteine residue at its N terminus, which allows for simple functionalisation of QDs or metal nanoparticles.

Here, TAT-c-conjugated QDs were incubated with MCF-7 cells, in order to determine their fate. The mechanism of uptake for small TAT-conjugated nanoparticles is unclear, however free TAT is understood to stimulate and undergo micropinocytosis in most cells (a specific case of endocytosis).[184]

5.5.1   Cysteamine-capped QDs

TAT-conjugated cysteamine-capped CdTe/CdS QDs (10 TAT-c per QD) were prepared using protocols described in section 2.8.4, with the same QDs as described in section 5.3.1. Uptake experiments were performed for these QDs in an identical fashion to those in section 5.3. Confocal images of the live cells after incubation, as well as confocal images of fixed and stained cells are shown in figure 77. TAT-c conjugation was successful only with positively-charged cysteamine-capped QDs; it is thought that the positive charge of TAT-c reduced the surface charge of the TGA-capped QDs, decreasing their colloidal stability.
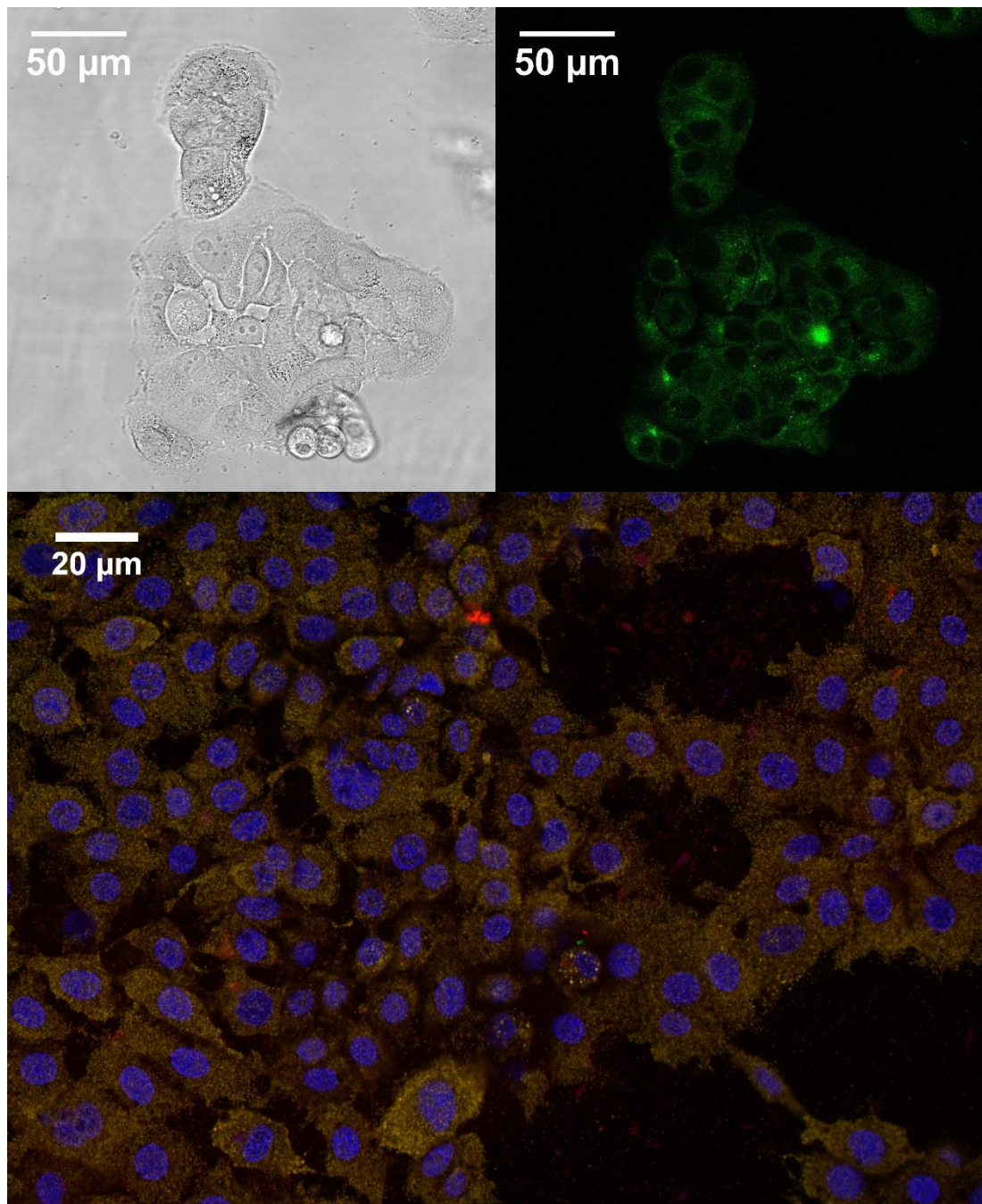
Figure 77. Top: Bright field (left) and confocal fluorescence image (right) of MCF-7 cells incubated with 3 nM TAT-c conjugated, cysteamine -capped CdTe/CdS QDs. Bottom: Confocal fluorescence image of fixed MCF-7 cells stained with Hoescht 33342 (blue) cysteamine-capped QDs (red) and Alexa-416-goat-EEA-1 (green), showing co-localisation of QDs and EEA-1.

The results are strikingly similar to what was observed for the QDs without TAT-c; the QDs exhibit bright PL from within the cells, but on study of confocal micrographs, appear to be

completely co-localised with endosomes. This suggests uptake is almost completely due to endocytosis.

PL intensities for QDs with and without TAT-c were compared in a similar fashion to the squeezing experiments, to determine whether the presence of TAT-c increased uptake for these QDs. An intensity scatter plot is shown in figure 78.
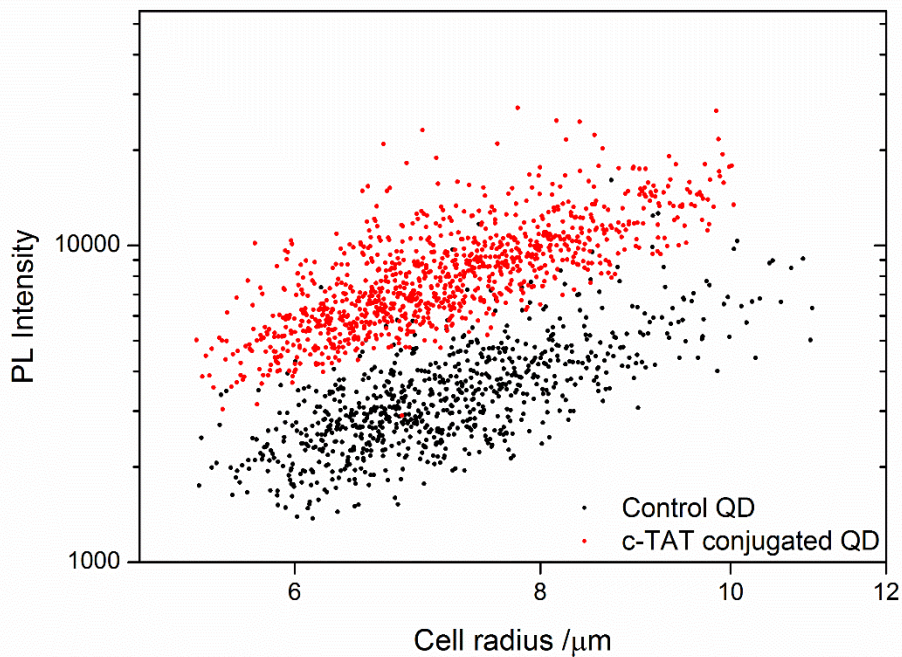
Figure 78. Scatter plot of total PL intensity per cell vs cell radius, as determined by confocal fluorescence microscopy, for cells incubated with control cysteamine-capped CdTe/CdS QDs (black) and with 10:1 TAT-c per QD (red).

As before, two populations are visible; cells incubated with TAT-c-conjugated QDs appear 2.1-fold brighter on average, attributed to an increase in the degree of endocytosis, as stimulated by the TAT-c peptide. This confirms that TAT-c is effective at stimulating uptake of QDs by MCF-7 cells. Results from confocal microscopy of fixed and stained cells suggests this increased uptake is due to an increase in endocytosis by these cells.
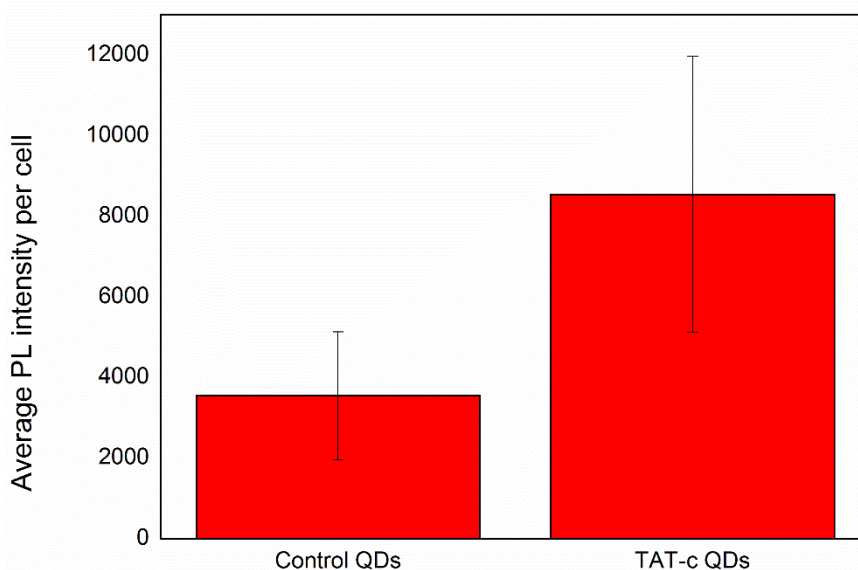
Figure 79. Average PL intensity per cell for cells incubated with control cysteamine-capped CdTe/CdS QDs (left) and with 10:1 TAT-c per QD (right).

5.6   Concluding remarks

The aim of the work in this chapter was to determine whether any one of various techniques would allow non-endocytic delivery of QDs into MCF-7 cells, or endosomal escape, resulting in QDs that are dispersed in the cell cytosol. The literature on this area of study is very thin; a large number, possibly a majority of papers that discuss QD biosensor systems in cells do not report on investigations of where the QD is located within the cell (at least to a satisfactory degree of precision).

It was found that the possible proton-sponge effect that is theorised to allow for endosomal release for amine-rich species was insufficient for the cysteamine-capped QDs. However, these QDs, as well as the negatively-charged, TGA-capped CdTe/CdS QDs, were readily endocytosed by the cells, and seemed to remain in endosomes at least 24 hours after initial incubation. If Q2NS-capped, redox sensitive QDs are incubated with the cells, endocytosis occurs, and the PL of the initially quenched, oxidised QDs recovers. By comparison to experiments discussed in chapter 5, this is interpreted as reduction of the quinones of Q2NS, resulting in a suppression of the PL-quenching electron transfer process, and suggests that these QDs may be useful for understanding changes in redox environment within the endocytic machinery. This may provide a useful tool for scientists who wish to perform long-term longitudinal studies of these processes, particularly for drug delivery and drug discovery applications.[175-177]

The cell-penetrating peptide (CPP) TAT-c was conjugated to cysteamine-capped QDs, and was shown to increase uptake of the QDs into MCF-7 cells by a factor of 2. Free TAT-c is taken up into cells by pinocytosis (or "cell drinking"). Similarly to QDs that had simply been incubated with the cells, all TAT-c-functionalised QDs found within the cells were within endosomes, suggesting TAT-c promotes uptake of QDs into cells by increasing the degree of endocytosis; this is not a surprise considering the understanding of the uptake of free TAT, as well as evidence from studies with gold nanoparticles.[185] It can be concluded that functionalisation with TAT-c is an effective strategy for increasing uptake of QDs into MCF-7 cells, if endocytic uptake is acceptable. If it is required that QDs are free of the endocytic pathway, then strategies for achieving endosomal release must be built in.

Mechanical "squeezing" of MCF-7 cells by application of shear forces in a microfluidic device was also shown to greatly improve uptake in comparison to simple co-incubation. Mechanical deformation of the cell membrane causes the formation of transient pores, which allow the diffusion of colloidal QDs in the surrounding medium into the interior of the cell. Analysis of TEM data shows that QDs are largely well distributed within the cytosol when this method has been applied. When the cells are squeezed in the presence of the redox sensitive, Q2NS-conjugated QDs, PL was seen to recover in a similar fashion to that observed for the redox QDs that are reduced within endosomes. However, the fact that PL recovers to a degree of intensity much greater than that exhibited by the control QDs, suggests that the redox active quinones of Q2NS are highly reduced within the cytosol of MCF-7 cells. For these cells, at least, the molecule Q2NS is therefore unsuitable for cytosolic redox sensing; a sufficient proportion of quinones must be oxidised that PL is slightly, but not completely quenched. In this ideal case, a small shift in redox environment will result in a change in the proportion of oxidised ligands, which will result in a measurable change in PL. It was expected that Q2NS would have similar redox properties to ubiquinone (which exists in an approximately 95% reduced state) due to structural similarities, however CV measurements (discussed in chapter 4) show that there is a considerable difference in redox potential for the QD-bound Q2NS.[186, 187]

Further work must therefore be performed in this area. It is the opinion of the author that a startling number of publications discussing intracellular biosensing with nanoparticles are not sufficiently rigorous in their determination of the fate of the nanoparticles, and therefore what part of the cell is actually subject to sensing. Understanding of nanoparticle uptake by cells is currently good when considering larger particles (20 nm and up) and for small molecules, however it is generally agreed that there is a gap in understanding for small

particles such as QDs.[188-190] This is perhaps a job for the cell biology community, considering the unsatisfactory rigour that has historically been applied by physicists studying such systems.

To design a redox sensor for MCF-7 cells based on the CdTe/CdS QD-acceptor strategy, an acceptor molecule must be chosen with a suitable redox potential. This should simply be a matter of synthesising and trialling a number of different redox active ligands. Quinones and similar molecules are common in biology, have well understood chemical behaviour and can span a wide range of reduction potentials, making them excellent candidates for development of further redox-sensing ligands.[191] Developing a library of redox sensing electron acceptor ligands, capable of efficiently quenching QD luminescence, while possessing a range of redox potentials will be the most practical way of realising QDs as flexible intracellular redox sensors.

6 Conclusions

The previous three chapters concerned development of QDs for application as redox biosensors. This thesis has discussed at length the necessity of thorough understanding of excited state dynamics in these QDs, for the enhancement or refinement of charge or energy transfer processes that are involved in sensing.

The aims of the work discussed in chapters 3, 4 and 5 can be distilled to the following:

- Synthesise and characterise optical properties of a library of candidate QDs for application in redox sensors, mainly based on CdTe and $CuInS_2$ QDs.
- Use STEM-EELS and crystallographic techniques to determine atomic structure, and therefore understand defect-related excited state dynamics in $CuInS_2$ and $CuInS_2ZnS$ QDs with a view to their application as redox sensors.
- Synthesise redox sensitive QDs based on CdTe/CdS QDs and the quinone ligand Q2NS, and characterise their redox-dependent optical properties.
- Perform time-resolved spectroscopy to elucidate excited state dynamics and recombination mechanisms of such sensors.
- Trial various surface capping agents on CdTe/CdS QDs in tandem with immunostaining studies to determine fate after uptake of QDs by MCF-7 cells.
- Determine whether CdTe/CdS-Q2NS redox sensors can be applied as redox sensors within MCF-7 cells, by measuring photoluminescence of internalised QDs.

$CuInS_2$ core and $CuInS_2$/ZnS QDs were the main focus of chapter 3. They are excellent potential candidate QDs for biosensing applications owing to their reduced toxicity in comparison to more common QD types (namely CdX, X=S, Se, Te), combined with excellent quantum yields. However, the defect-tolerant nature of $CuInS_2$ leads to some interesting excitonic properties, which are currently of much debate and discussion in the literature.

Previous work by Kraatz et al concluded that the emissive process in $CuInS_2$ QDs involved a defect state-to-valence band transition involving an In_{Cu} anti-site defect. These defects are predicted to have low formation energy in chalcopyrite $CuInS_2$, particularly when the lattice is copper-poor. This evidence was based on ultrafast TA spectroscopy studies, along with computational estimates of the energy of states associated with these defects, and supported by the circumstantial evidence that Cu-poor $CuInS_2$ QDs exhibited better PLQY. However, the nature of these defects within the lattice of $CuInS_2$ QDs was still unclear.

CuInS$_2$ core and CuInS$_2$/ZnS core/shell QDs were synthesised, and their optical properties (PL and absorbance spectra) were found to be in keeping with QDs discussed in the literature. This is characterised by a wide stokes shift, as well as a broad (>100 nm) photoluminescence, consistent with defect-state related emission. X-ray diffraction experiments also showed that the lattice structure of the core QDs was chalcopyrite CuInS$_2$. HAADF- STEM images of QDS showed the expected tetrahedral shape.

STEM-EELS images of both core CuInS$_2$ and core/shell CuInS$_2$/ZnS QDs, however, showed a high degree of segregation of the cationic elements in the QD structure. This was attributed to the high stability of the $2V_{Cu} + In_{Cu}$ defect cluster. The high degree of heterogeneity between QDs, in terms of the degree of segregation, was therefore concluded to contribute to the broad excitonic features observed in ensembles of CuInS$_2$ QDs. As the local band gap is dependent on composition, energy levels of emissive defects are expected to cover a wide range, relative to the valence band. This is also expected to depend heavily on the location of the defect site within the highly-faceted tetrahedral nanoparticle.

The fact that high PLQY is observed for these QDs, despite the highly defected nature, suggests that they may be excellent candidates for future studies on doping in QDs. However, issues with achieving transfer of the hydrophobic CuInS$_2$ QDs into aqueous environment still present challenges for their application as redox sensors.

In chapter 4, excited state dynamics of CdTe/CdS QDs conjugated to the redox-sensitive quinone ligand Q2NS were explored. This conjugate behaves as a redox sensor, where PL is switched depending on the redox state of the Q2NS ligand; oxidised Q2NS received an electron from the photo-excited QD, and the PL is quenched. When the quinones of Q2NS are reduced, this electron transfer is suppressed, and the PL recovers. Compared to other redox sensors present in the literature, only relatively small amounts of conjugated quinone were required to completely quench PL (around 20 per QD), suggesting a particularly efficient and unique mechanism of electron transfer for these conjugates. Optical and structural properties (as determined by TEM) of these QDs are similar to those of QDs found in the literature.

Transient absorption (TA) studies, in combination with transient PL studies implicated an intermediate hot trap state in the electron transfer to the quinones. This trap state allows efficient transfer to oxidised quinones of Q2NS. Critically, however, electrons that are not transferred from the trap state (in the cases where Q2NS is not present or has been reduced) are later able to cool to the conduction band minimum and undergo radiative recombination

as normal. The surprising efficiency of the trapping process was reinforced by evidence from atomistic semiempirical pseudopotential calculations, which suggest that transfer times as fast as approximately 2 ps are possible if the Q2NS is bound to a cation close to the trap. This high efficiency, along with the previously-understood type-II nature of CdTe/CdS core/shell QDs, (which causes the electron to be associated with the QD shell) suggests that the intermediate trap state is likely to be associated with the surface.

This new understanding of an extremely efficient charge transfer mechanism from QDs is expected to be useful for the development of new redox sensors, where efficient quenching can be achieved with only a small number of acceptor ligands. This diminishes the negative impact of these ligands on the colloidal properties of the QD, and leaves more space for further functionalisation, which could involve targeting to specific organelles such as mitochondria, where many metabolic processes take place. Aside from biosensing, this technology may also be of use in photovoltaics, where increasing charge extraction efficiency from semiconductors is of paramount importance for improving overall device performance.

Critically, the CdTe/CdS QDs discussed in chapter 4 were synthesised via an aqueous route. Aside from the practical and environmental benefits this affords (the latter of which is admittedly largely offset by the grossly environmentally harmful heavy metals involved), the result is that these QDs are readily dispersible in water (or other aqueous solutions). This is critical for their application to biology, which is aqueous by nature. In addition, a wide range of molecules can be used as capping agents. The best results are achieved with small thiols, which regulate growth and provide colloidal stability to the QD. In this work, both positively charged (in solution), amine-terminated and negatively charged carboxylic acid terminated capping ligands were used, to achieve charge mediated colloidal stability in both senses.

In chapter 5, QDs capped with both amine- and carboxylic acid-terminated molecules, as well as QDs conjugated to a cell penetrating peptide, were incubated with MCF-7 cells to determine their fate after expected endocytosis. In addition, it was intended to determine the degree of toxicity the QDs pose to MCF-7 cells; a useful biosensor must have little effect on cell viability.

MCF-7 cells are a human breast cancer cell line, and were chosen as they exhibit a particularly reduced cellular redox environment. The rationale was that the effectiveness of the redox sensors could be determined by demonstrating switch-on of luminescence by the reducing environment within the cell. This was the final objective of the work presented in chapter 5.

Endocytosis describes a number of processes by which cells internalise material from their surroundings, and includes pinocytosis (cell drinking, where liquid from the exterior of the cell is taken up) or phagocytosis (solid material). After materials are endocytosed, they typically spend some time within compartments or vesicles of the endocytic pathway, termed endosomes. This presents a problem for redox biosensors introduced to the cell in this way; the redox environment is greatly different within an endosome compared to the cytosol, and so useful redox sensing will not be achieved unless the sensors can escape the endosomes.

Cysteamine-capped QDs were incubated with the MCF-7 cells, in the hope that the "proton-sponge effect" would allow escape from endosomes by triggering their osmotic lysis. After 24 hours of co-incubation, immunostaining studies revealed absolute co-localisation of QDs with endosomal markers, suggesting that endosomal escape had not been achieved. This was also true for the control QDs, which were capped with TGA, a carboxylic acid-terminated ligand. It was therefore concluded that the proton-sponge effect that is commonly observed for polymeric transfection reagents (which can have a very large number of amine groups) would be difficult to reproduce for QDs, where the number of amine groups is limited by the surface area of the QD.

An experiment where the cells were incubated with cysteamine-capped QDs conjugated with the cell-penetrating-peptide TAT-c was performed. The aim was to assess if this peptide could increase the rate of internalisation of QDs by the MCF-7 cells, and whether this internalisation would happen via endocytosis or some other process. While it was found that the TAT-c-conjugated QDs were internalised by cells approximately twice as efficiently as control QDs, it was again found that the QDs resided within the endosomes of cells 24 hours after initial incubation. Again, this prevents their application as a useful biosensor for measuring cytosolic redox environment.

Although the previous methods for obtaining internalisation of QDs into cells demonstrated only reliable delivery of QDs to endosomes, this is not useless; understanding the redox behaviour of the endocytic process is important to biologists studying internalisation. Q2NS-conjugated, redox sensitive QDs were shown to be reduced after uptake by endocytosis, suggesting that these QDs could be useful candidates for measurement of redox environment within the endosomes.

Finally, cells that were mechanically deformed in the presence of QDs were shown to have taken up QDs both by endocytosis, as well as by diffusion of QDs into the cell cytosol, via

transient pores in the cell membrane that arise as a result of the deformation. When Q2NS-conjugated, redox-sensitive QDs were used, the PL was switched on by the reducing environment of the cytosol. However, this switch-on of luminescence was absolute, suggesting that the Q2NS was completely reduced by the cytosol. Unfortunately this places a limitation on these particular QD-acceptor conjugates for use as redox sensors with MCF-7 cells; an ideal system would have a proportion, but not all, of acceptors in the oxidised, electron-accepting state.

The work with QDs in cells suggests a number of challenges that face the QD and biosensing communities. Firstly, for each type of sensor that is internalised by a cell, the exact microenvironment must be identified. It is the opinion of the author that many of the sensors mentioned in section 1.7 of this thesis likely reside in endosomes, or at least in a variety of microenvironments, and that this is not considered in enough depth by the reporting authors. To overcome this challenge, new strategies must be designed that allow endosomal release, or prevention of endocytic uptake (where it is not desired).

Adaptation of the current redox sensors to different reducing environments is the other challenge, and this is likely to be significantly simpler. Changing the redox-active ligand to another with higher or lower redox potential will allow for only a proportion of an ensemble of sensing ligands to be in either the oxidised (and electron-accepting) or reduced state, affording the greatest possible sensitivity.

7 Future work

7.1 Peptides as "Soft" Ligands for QDs

The role of ligands in the excited state dynamics of colloidal QDs was discussed in section 1.3.4, with particular respect to the passivation or introduction of electron or hole trapping states, which can negatively affect the photoluminescent properties. For QDs applied to biosensing, it was shown that difficulty is often encountered when performing ligand exchanges, in order to impart functionality to the QD or transfer previously hydrophobic QDs into the aqueous phase. Thiols are popular ligands due to their high affinity for materials such as CdSe and CdTe, but, depending on the material, their removal or replacement can introduce new trap states that negatively affect photoluminescence. There is therefore a need to develop strategies for specific binding to QDs that do not involve thiols, and do not necessarily require stripping away of ligands that are passivating surface trap states.

Bacteriophages are viruses which propagate by attacking bacteria. Because of this, they are easy to maintain, and their lack of danger towards humans has turned them into flexible biological tools. Phage display is a technique whereby the genome of phage viruses is modified so that a random sequence of a set number of amino acid residues is presented on the surface of the virus, usually by appendage to one of the coat proteins. A large number ($\sim 10^8$-10^9) of these phage, each with a different sequence, can then be panned against a target of choice, in an attempt to find peptide sequences that effectively bind. This is very useful for biologists who wish to develop antibodies for specific targets, but has been employed in a wide variety of fields by those who require specific binding between objects including small molecules, large proteins or even solid materials.[192, 193]

Phage display has previously been used to find peptides that can bind to gold nanoparticles, as well as act as growth-directing ligands for various nanoparticle morphologies.[194, 195] In addition, peptides have been discovered that bind to specific facets of semiconductor materials, and have been shown to allow for assembly of semiconductor nanocrystals.[196] The surfaces of QDs, however, are highly curved and faceted, and so may warrant discovery of different peptides for efficient binding.

Early work has demonstrated promise; phage display experiments performed in May 2017 identified five candidate peptides which bind efficiently to CdTe/CdS QDs. These peptides are shown in figure 80, which plots their binding efficiency vs control (a sequence of 5 astatine residues), as ascertained by measuring PL emission from QDs immobilised on a

surface by the respective peptide. Further experiments will involve binding assays with truncated versions of the identified peptides, in order to elucidate any specific short sequences that are involved in binding to the CdS surface.

	Sequence
①	GDGNSVLKPGNW
②	TLTSETPWSLNR
③	YPSSLNINASSF
④	SGVYKVAYDWQH
⑤	SHALQGPEGTAT
⑥	AAAAA
R①	WNGPKLVSNGDG
R②	RNLSWPTESTLT
R③	FSSANINLSSPY
R④	HQWDYAVKYVGS
R⑤	TATGEPGQLAHS
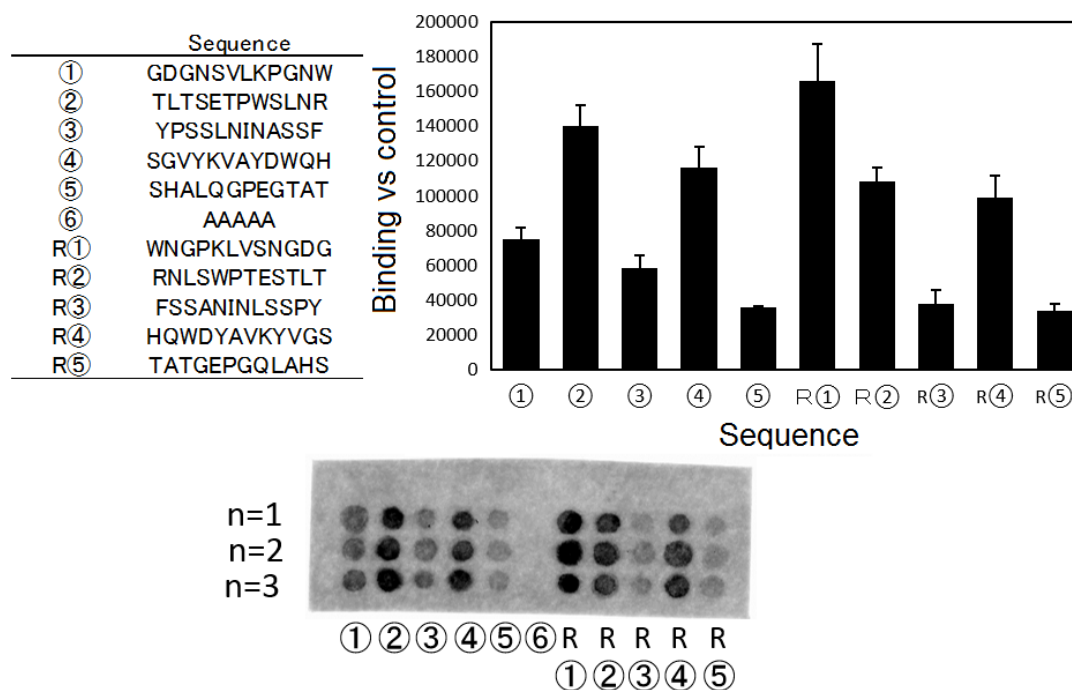
Figure 80. Left - List of discovered peptides that bind to TGA-capped CdTe/CdS QDs. Bottom – negative of fluorescence image of QDs immobilised on surface by discovered peptides. The magnitude of the PL signal is proportional to the number of adsorbed QDs. Right – Intensity of binding as measured by PL experiment, normalised to control.

Importantly, early work shows that binding of free peptides does not reduce PLQY of the QDs, suggesting that PL-damaging problems so often associated with ligand exchange or ligand addition processes will be avoidable by using these peptides as binding groups.

7.2   Single-particle Cathodoluminescence of CuInS$_2$ QDs

Chapter three of this thesis discusses the defect-mediated photoluminescence of CuInS$_2$ QDs, and the resulting broad excitonic features exhibited by ensembles of these QDs. Perhaps the most striking result from this work is the large degree of heterogeneity between particles, with respect to the elemental segregation between them. It is now apparent that the number of radiative centres per particle may vary widely, as well as the energies of the states associated with them (as the energy is dependent on location within the particle as well as local band gap, which depends on composition). To date, we have only been able to perform

large scale ensemble measurements of optical properties (on relatively concentrated QD solutions) and so spectral features associated with individual particles are not resolvable.

Cathodoluminescence, broadly speaking, is the opposite of the photoelectric effect, and describes the situation whereby photons of visible light are emitted from a material or object that is impinged upon by an electron beam. A classic example of cathodoluminescence is the glowing phosphor used to generate an image in the first electron microscopes, but now cathodoluminescence spectrometry is used as a (usually TEM-based) tool to study energy transitions in a wide range of materials. Measurements can be performed in the way as the STEM-EELS experiments described in chapter 3, albeit collecting visible wavelengths rather than x-rays. For QDs, the luminescent transition is expected to be the same for both optical and electronic excitation, and so single-particle cathodoluminescence studies allow interrogation of the emissive transitions for individual particles. [197, 198]

Cathodoluminescence studies of QDs that undergo band-edge emission yield a single, ultra-narrow single-particle emission.[199] The breadth of the emission spectrum of an ensemble of these QDs is therefore explained mostly by the size polydispersity of the ensemble. This may be different for the $CuInS_2$ QDs, which are expected to have a variable number of emissive centres per particle. It may be that individual QDs are capable of emitting at a number of distinct wavelengths, one for each emissive point defect the particle has. With very high-resolution HAADF-STEM systems, it may also be possible to excite individual emissive point defects within the lattice of a single QD in parallel with high-resolution imaging. A STEM-based cathodoluminescence study of these $CuInS_2$ could therefore yield a lot of information about the nature of their defect-related luminescence.

8 References

1. Lodish, H., et al., *Molecular cell biology*. Vol. 3. 1995: WH Freeman New York.
2. Alberts, B., *Molecular biology of the cell*. 2017: Garland science.
3. Rapkine, I., *(1931): Sur les processus chimiques au cours de la division cellulaire.* Annales de physiologie et de physicochimie biologique. **7**: p. 382-418.
4. Sarsour, E.H., et al., *Redox control of the cell cycle in health and disease.* Antioxidants & redox signaling, 2009. **11**(12): p. 2985-3011.
5. Toyokuni, S., et al., *Persistent oxidative stress in cancer.* FEBS letters, 1995. **358**(1): p. 1-3.
6. Heiden, M.G.V. and R.J. DeBerardinis, *Understanding the Intersections between Metabolism and Cancer Biology.* Cell, 2017. **168**(4).
7. Hwang, O., *Role of oxidative stress in Parkinson's disease.* Experimental neurobiology, 2013. **22**(1): p. 11-17.
8. Valko, M., et al., *Free radicals and antioxidants in normal physiological functions and human disease.* The international journal of biochemistry & cell biology, 2007. **39**(1): p. 44-84.
9. Parellada, M., et al., *Plasma antioxidant capacity is reduced in Asperger syndrome.* Journal of Psychiatric Research, 2012. **46**(3): p. 394-401.
10. Joseph, N., et al., *Oxidative stress and ADHD: a meta-analysis.* Journal of attention disorders, 2015. **19**(11): p. 915-924.
11. Sies, H., *Oxidative stress: a concept in redox biology and medicine.* Redox biology, 2015. **4**: p. 180-183.
12. Liberti, M.V. and J.W. Locasale, *The Warburg effect: how does it benefit cancer cells?* Trends in biochemical sciences, 2016. **41**(3): p. 211-218.
13. Auchinvole, C.A.R., et al., *Monitoring Intracellular Redox Potential Changes Using SERS Nanosensors.* Acs Nano, 2012. **6**(1): p. 888-896.
14. Lunt, S.Y. and M.G. Vander Heiden, *Aerobic glycolysis: meeting the metabolic requirements of cell proliferation.* Annual review of cell and developmental biology, 2011. **27**: p. 441-464.
15. West, J.L. and N.J. Halas, *Applications of nanotechnology to biotechnology: Commentary.* Current opinion in biotechnology, 2000. **11**(2): p. 215-217.
16. Sooklal, K., et al., *A Blue-Emitting CdS/Dendrimer Nanocomposite.* Adv Mater, 1998. **10**(14): p. 1083-1087.
17. Mattoussi, H., et al., *Colloidal semiconductor quantum dot conjugates in biosensing*, in *Optical Biosensors*. 2002, Elsevier. p. 537-569.
18. Zheng, K., et al., *Ultrafast photoinduced dynamics in quantum dot-based systems for light harvesting.* Nano Research, 2015. **8**(7): p. 2125-2142.
19. Kongkanand, A., et al., *Quantum dot solar cells. Tuning photoresponse through size and shape control of CdSe-TiO2 architecture.* Journal of the American Chemical Society, 2008. **130**(12): p. 4007-15.
20. Kamat, P.V., *Boosting the efficiency of quantum dot sensitized solar cells through modulation of interfacial charge transfer.* Acc Chem Res, 2012. **45**(11): p. 1906-15.
21. Medintz, I.L., et al., *Quantum dot bioconjugates for imaging, labelling and sensing.* Nature materials, 2005. **4**(6): p. 435-446.
22. Jang, E., et al., *White-light-emitting diodes with quantum dot color converters for display backlights.* Adv Mater, 2010. **22**(28): p. 3076-3080.
23. Jain, F.C. and F. Papadimitrakopoulos, *Full color display structures using pseudomorphic cladded quantum dot nanophosphor thin films*, 2006, Google Patents.

24. Cheon, K.-O., M. LoCascio, and S.M. Yang, *Infrared display with luminescent quantum dots*, US20050006656, 2012.
25. Veldhorst, M., et al., *An addressable quantum dot qubit with fault-tolerant control-fidelity.* Nature nanotechnology, 2014. **9**(12): p. 981.
26. Clapp, A.R., et al., *Quantum dot-based multiplexed fluorescence resonance energy transfer.* Journal of the American Chemical Society, 2005. **127**(51): p. 18212-18221.
27. Algar, W.R., A.J. Tavares, and U.J. Krull, *Beyond labels: A review of the application of quantum dots as integrated components of assays, bioprobes, and biosensors utilizing optical transduction.* Analytica Chimica Acta, 2010. **673**(1): p. 1-25.
28. Freeman, R. and I. Willner, *Optical molecular sensing with semiconductor quantum dots (QDs).* Chem Soc Rev, 2012. **41**(10): p. 4067-85.
29. Hildebrandt, N., et al., *Energy transfer with semiconductor quantum dot bioconjugates: A versatile platform for biosensing, energy harvesting, and other developing applications.* Chemical reviews, 2016. **117**(2): p. 536-711.
30. Kittel, C., *Introduction to Solid State Physics, Seventh Edition*. 2011: Wiley VCH.
31. Qi, W., M. Wang, and Q. Liu, *Shape factor of nonspherical nanoparticles.* Journal of materials science, 2005. **40**(9-10): p. 2737-2739.
32. Vidal, J., et al., *Strong Interplay between Structure and Electronic Properties in CuIn(S, Se)(2): A First-Principles Study.* Physical Review Letters, 2010. **104**(5).
33. Jasieniak, J., M. Califano, and S.E. Watkins, *Size-Dependent Valence and Conduction Band-Edge Energies of Semiconductor Nanocrystals.* Acs Nano, 2011. **5**(7): p. 5888-5902.
34. Califano, M., A. Franceschetti, and A. Zunger, *Temperature dependence of excitonic radiative decay in CdSe quantum dots: The role of surface hole traps.* Nano letters, 2005. **5**(12): p. 2360-2364.
35. Califano, M., A. Zunger, and A. Franceschetti, *Efficient inverse Auger recombination at threshold in CdSe nanocrystals.* Nano letters, 2004. **4**(3): p. 525-531.
36. Gaponenko, S.V., *Introduction to nanophotonics*. 2010: Cambridge University Press.
37. Di Bartolo, B. and O. Forte, *Frontiers Developments in Optics and Spectroscopy*. 1997: Ottavio Forte.
38. Sun, J. and E.M. Goldys, *Linear absorption and molar extinction coefficients in direct semiconductor quantum dots.* The Journal of Physical Chemistry C, 2008. **112**(25): p. 9261-9266.
39. Harvie, A.J., et al., *Observation of compositional domains within individual copper indium sulfide quantum dots.* Nanoscale, 2016. **8**(36): p. 16157-16161.
40. Booth, M., et al., *Determining the concentration of CuInS2 quantum dots from the size-dependent molar extinction coefficient.* Chemistry of Materials, 2012. **24**(11): p. 2064-2070.
41. Smith, C.T., et al., *Energy structure of CdSe/CdTe type II colloidal quantum dots—Do phonon bottlenecks remain for thick shells?* Solar Energy Materials and Solar Cells, 2016. **158**: p. 160-167.
42. Efros, A.L., V. Kharchenko, and M. Rosen, *Breaking the phonon bottleneck in nanometer quantum dots: Role of Auger-like processes.* Solid State Communications, 1995. **93**(4): p. 281-284.
43. Benisty, H., C. Sotomayor-Torres, and C. Weisbuch, *Intrinsic mechanism for the poor luminescence properties of quantum-box systems.* Physical Review B, 1991. **44**(19): p. 10945.
44. Inoshita, T. and H. Sakaki, *Electron relaxation in a quantum dot: Significance of multiphonon processes.* Physical Review B, 1992. **46**(11): p. 7260.
45. Smith, C.T., et al., *Ultrafast Charge Dynamics in Trap-Free and Surface-Trapping Colloidal Quantum Dots.* Advanced science, 2015. **2**(10).

46.   Pandey, A. and P. Guyot-Sionnest, *Slow electron cooling in colloidal quantum dots.* Science, 2008. **322**(5903): p. 929-932.

47.   Hines, M.A. and P. Guyot-Sionnest, *Synthesis and characterization of strongly luminescing ZnS-capped CdSe nanocrystals.* The Journal of Physical Chemistry, 1996. **100**(2): p. 468-471.

48.   Kuno, M., et al., *The band edge luminescence of surface modified CdSe nanocrystallites: Probing the luminescing state.* The Journal of Chemical Physics, 1997. **106**(23): p. 9869-9882.

49.   Kraatz, I.T., et al., *Sub-bandgap emission and intraband defect-related excited-state dynamics in colloidal CuInS2/ZnS quantum dots revealed by femtosecond pump–dump–probe spectroscopy.* The Journal of Physical Chemistry C, 2014. **118**(41): p. 24102-24109.

50.   Mao, B., et al., *Synthesis and photophysical properties of ternary I–III–VI AgInS2 nanocrystals: intrinsic versus surface states.* The Journal of Physical Chemistry C, 2011. **115**(18): p. 8945-8954.

51.   Dabbousi, B.O., et al., *(CdSe) ZnS core– shell quantum dots: synthesis and characterization of a size series of highly luminescent nanocrystallites.* The Journal of Physical Chemistry B, 1997. **101**(46): p. 9463-9475.

52.   Kim, S., et al., *Type-II quantum dots: CdTe/CdSe (core/shell) and CdSe/ZnTe (core/shell) heterostructures.* Journal of the American Chemical Society, 2003. **125**(38): p. 11466-11467.

53.   Kim, S., et al., *Near-infrared fluorescent type II quantum dots for sentinel lymph node mapping.* Nature Biotechnology, 2004. **22**(1): p. 93-97.

54.   Hatami, F., et al., *Radiative recombination in type-II GaSb/GaAs quantum dots.* Applied Physics Letters, 1995. **67**(5): p. 656-658.

55.   Virzbickas, K., et al., *Surfactant-dependent photoluminescence of CdTe/CdS nanocrystals.* Journal of Experimental Nanoscience, 2017. **12**(1): p. 94-103.

56.   Jain, A., et al., *Atomistic Design of CdSe/CdS Core–Shell Quantum Dots with Suppressed Auger Recombination.* Nano letters, 2016. **16**(10): p. 6491-6496.

57.   Kortan, A., et al., *Nucleation and growth of cadmium selendie on zinc sulfide quantum crystallite seeds, and vice versa, in inverse micelle media.* Journal of the American Chemical Society, 1990. **112**(4): p. 1327-1332.

58.   Lo, S.S., et al., *Emergent properties resulting from type-II band alignment in semiconductor nanoheterostructures.* Adv Mater, 2011. **23**(2): p. 180-197.

59.   Peterson, M.D., et al., *The role of ligands in determining the exciton relaxation dynamics in semiconductor quantum dots.* Annual review of physical chemistry, 2014. **65**: p. 317-339.

60.   Wuister, S.F., C. de Mello Donega, and A. Meijerink, *Influence of thiol capping on the exciton luminescence and decay kinetics of CdTe and CdSe quantum dots.* The Journal of Physical Chemistry B, 2004. **108**(45): p. 17393-17397.

61.   Munro, A.M. and D.S. Ginger, *Photoluminescence quenching of single CdSe nanocrystals by ligand adsorption.* Nano letters, 2008. **8**(8): p. 2585-2590.

62.   Fischer, S.A., et al., *Passivating ligand and solvent contributions to the electronic properties of semiconductor nanocrystals.* Nanoscale, 2012. **4**(3): p. 904-914.

63.   Omogo, B., J.F. Aldana, and C.D. Heyes, *Radiative and nonradiative lifetime engineering of quantum dots in multiple solvents by surface atom stoichiometry and ligands.* The Journal of Physical Chemistry C, 2013. **117**(5): p. 2317-2327.

64.   Lakowicz, J.R., *Principles of Fluorescence Spectroscopy, Third Edition*. 2006: Springer.

65.   Harvie, A.J., et al., *Ultrafast Trap-State Mediated Electron Transfer for Quantum Dot Redox Sensing.* The Journal of Physical Chemistry C, 2018.

66. Alivisatos, A.P., *Semiconductor clusters, nanocrystals, and quantum dots.* Science, 1996. **271**(5251): p. 933-937.

67. Abraham, F., *Homogeneous Nucleation Theory; The pretransition Theory of Vapor Condensation (Supplement 1).* 1974: New York, Academic Press.

68. Voorhees, P.W., *The theory of Ostwald ripening.* Journal of Statistical Physics, 1985. **38**(1-2): p. 231-252.

69. Nightingale, A.M., *Improving the ensemble optical properties of InP quantum dots by indium precursor modification.* Journal of Materials Chemistry C, 2016. **4**(36): p. 8454-8458.

70. Murray, C., D.J. Norris, and M.G. Bawendi, *Synthesis and characterization of nearly monodisperse CdE (E= sulfur, selenium, tellurium) semiconductor nanocrystallites.* Journal of the American Chemical Society, 1993. **115**(19): p. 8706-8715.

71. Pong, B.-K., B.L. Trout, and J.-Y. Lee, *Modified ligand-exchange for efficient solubilization of CdSe/ZnS quantum dots in water: A procedure guided by computational studies.* Langmuir, 2008. **24**(10): p. 5270-5276.

72. Dubois, F., et al., *A versatile strategy for quantum dot ligand exchange.* Journal of the American Chemical Society, 2007. **129**(3): p. 482-483.

73. Tamang, S., et al., *Aqueous phase transfer of InP/ZnS nanocrystals conserving fluorescence and high colloidal stability.* Acs Nano, 2011. **5**(12): p. 9392-9402.

74. Booth, M., et al., *Amphipol-encapsulated CuInS 2/ZnS quantum dots with excellent colloidal stability.* RSC Advances, 2013. **3**(43): p. 20559-20566.

75. Nida, D., et al., *Photostability of quantum dots with amphiphilic polymer-based passivation strategies.* Nanotechnology, 2007. **19**(3): p. 035701.

76. Pellegrino, T., et al., *Hydrophobic nanocrystals coated with an amphiphilic polymer shell: a general route to water soluble nanocrystals.* Nano letters, 2004. **4**(4): p. 703-707.

77. Fan, H., et al., *Surfactant-assisted synthesis of water-soluble and biocompatible semiconductor quantum dot micelles.* Nano letters, 2005. **5**(4): p. 645-648.

78. Gaponik, N., et al., *Thiol-capping of CdTe nanocrystals: an alternative to organometallic synthetic routes.* The Journal of Physical Chemistry B, 2002. **106**(29): p. 7177-7185.

79. Wiecinski, P.N., et al., *Toxicity of Oxidatively Degraded Quantum Dots to Developing Zebrafish (Danio rerio).* Environmental Science & Technology, 2013. **47**(16): p. 9132-9139.

80. Chen, N., et al., *The cytotoxicity of cadmium-based quantum dots.* Biomaterials, 2012. **33**(5): p. 1238-1244.

81. Rzigalinski, B.A. and J.S. Strobl, *Cadmium-containing nanoparticles: perspectives on pharmacology and toxicology of quantum dots.* Toxicology and Applied Pharmacology, 2009. **238**(3): p. 280-288.

82. Bottrill, M. and M. Green, *Some aspects of quantum dot toxicity.* Chemical Communications, 2011. **47**(25): p. 7039-7050.

83. Kirchner, C., et al., *Cytotoxicity of colloidal CdSe and CdSe/ZnS nanoparticles.* Nano letters, 2005. **5**(2): p. 331-338.

84. Brunetti, V., et al., *InP/ZnS as a safer alternative to CdSe/ZnS core/shell quantum dots: in vitro and in vivo toxicity assessment.* Nanoscale, 2013. **5**(1): p. 307-317.

85. Pons, T., et al., *Cadmium-free CuInS2/ZnS quantum dots for sentinel lymph node imaging with reduced toxicity.* Acs Nano, 2010. **4**(5): p. 2531-2538.

86. Derfus, A.M., W.C. Chan, and S.N. Bhatia, *Probing the cytotoxicity of semiconductor quantum dots.* Nano letters, 2004. **4**(1): p. 11-18.

87. Summers, H.D., et al., *Quantification of nanoparticle dose and vesicular inheritance in proliferating cells.* Acs Nano, 2013. **7**(7): p. 6129-6137.

88. Delehanty, J.B., H. Mattoussi, and I.L. Medintz, *Delivering quantum dots into cells: strategies, progress and remaining issues.* Analytical and Bioanalytical Chemistry, 2009. **393**(4): p. 1091-1105.

89. Damalakiene, L., et al., *Intracellular distribution of nontargeted quantum dots after natural uptake and microinjection.* International journal of nanomedicine, 2013. **8**: p. 555.

90. Benjaminsen, R.V., et al., *The possible "proton sponge" effect of polyethylenimine (PEI) does not include change in lysosomal pH.* Molecular Therapy, 2013. **21**(1): p. 149-157.

91. Yoon, S., et al., *Direct and sustained intracellular delivery of exogenous molecules using acoustic-transfection with high frequency ultrasound.* Scientific reports, 2016. **6**: p. 20477.

92. Miller, D.L., S.V. Pislaru, and J.F. Greenleaf, *Sonoporation: mechanical DNA delivery by ultrasonic cavitation.* Somatic cell and molecular genetics, 2002. **27**(1): p. 115-134.

93. Zhang, Y. and L.-C. Yu, *Microinjection as a tool of mechanical delivery.* Current opinion in biotechnology, 2008. **19**(5): p. 506-510.

94. Stryer, L., *Fluorescence Energy-Transfer as a Spectroscopic Ruler.* Annual Review of Biochemistry, 1978. **47**: p. 819-846.

95. Medintz, I.L., et al., *Self-assembled nanoscale biosensors based on quantum dot FRET donors.* Nature materials, 2003. **2**(9): p. 630-638.

96. Freeman, R., et al., *Biosensing and Probing of Intracellular Metabolic Pathways by NADH-Sensitive Quantum Dots.* Angewandte Chemie, 2009. **121**(2): p. 315-319.

97. Algar, W.R., et al., *Quantum dots as platforms for charge transfer-based biosensing: challenges and opportunities.* Journal of Materials Chemistry B, 2014. **2**(45): p. 7816-7827.

98. Medintz, I.L., et al., *Quantum-dot/dopamine bioconjugates function as redox coupled assemblies for in vitro and intracellular pH sensing.* Nature materials, 2010. **9**(8): p. 676-684.

99. Clarke, S.J., et al., *Photophysics of dopamine-modified quantum dots and effects on biological systems.* Nat Mater, 2006. **5**(5): p. 409-17.

100. Sandros, M.G., D. Gao, and D.E. Benson, *A modular nanoparticle-based system for reagentless small molecule biosensing.* Journal of the American Chemical Society, 2005. **127**(35): p. 12198-9.

101. Sandros, M.G., V. Shete, and D.E. Benson, *Selective, reversible, reagentless maltose biosensing with core-shell semiconducting nanoparticles.* Analyst, 2006. **131**(2): p. 229-35.

102. Shete, V.S. and D.E. Benson, *Protein design provides lead(II) ion biosensors for imaging molecular fluxes around red blood cells.* Biochemistry, 2009. **48**(2): p. 462-70.

103. Swain, M.D., J. Octain, and D.E. Benson, *Unimolecular, Soluble Semiconductor Nanoparticle-Based Biosensors for Thrombin Using Charge/Electron Transfer.* Bioconjugate Chemistry, 2008. **19**(12): p. 2520-2526.

104. Medintz, I.L., et al., *Interactions between Redox Complexes and Semiconductor Quantum Dots Coupled via a Peptide Bridge.* Journal of the American Chemical Society, 2008. **130**(49): p. 16745-16756.

105. Yiidiz, I., M. Tomasulo, and F.M. Raymo, *A mechanism to signal receptor-substrate interactions with luminescent quantum dots.* Proceedings of the National Academy of Sciences of the United States of America, 2006. **103**(31): p. 11457-11460.

106. Ji, X., et al., *On the pH-dependent quenching of quantum dot photoluminescence by redox active dopamine.* Journal of the American Chemical Society, 2012. **134**(13): p. 6006-6017.

107. Jackson, D.M. and A. Westlind-Danielsson, *Dopamine receptors: molecular biology, biochemistry and behavioural aspects.* Pharmacology & therapeutics, 1994. **64**(2): p. 291-370.

108. Stoof, J. and J. Kebabian, *Two dopamine receptors: biochemistry, physiology and pharmacology.* Life Sciences, 1984. **35**(23): p. 2281-2296.

109. Freeman, R. and I. Willner, *NAD+/NADH-sensitive quantum dots: applications to probe NAD+-dependent enzymes and to sense the RDX explosive.* Nano letters, 2008. **9**(1): p. 322-326.

110. Ernster, L. and G. Dallner, *Biochemical, Physiological and Medical Aspects of Ubiquinone Function.* Biochimica Et Biophysica Acta-Molecular Basis of Disease, 1995. **1271**(1): p. 195-204.

111. Qin, L.X., et al., *Coenzyme Q functionalized CdTe/ZnS quantum dots for reactive oxygen species (ROS) imaging.* Chemistry, 2011. **17**(19): p. 5262-71.

112. Ma, W., et al., *Ubiquinone-quantum dot bioconjugates for in vitro and intracellular complex I sensing.* Scientific reports, 2013. **3**: p. 1537.

113. Booth, M., *Synthesis and characterisation of CuInS2 quantum dots*, 2014, University of Leeds.

114. Gu, Z., et al., *One-pot synthesis of highly luminescent CdTe/CdS core/shell nanocrystals in aqueous phase.* Nanotechnology, 2008. **19**(13): p. 135604.

115. Zhang, S. and Y. Zhao, *Rapid release of entrapped contents from multi-functionalizable, surface cross-linked micelles upon different stimulation.* Journal of the American Chemical Society, 2010. **132**(31): p. 10642-10644.

116. Huisgen, R., *Centenary lecture-1, 3-dipolar cycloadditions*, 1961, ROYAL SOC CHEMISTRY THOMAS GRAHAM HOUSE, SCIENCE PARK, MILTON RD, CAMBRIDGE CB4 0WF, CAMBS, ENGLAND.

117. Page, R.C., et al., *Near-Unity Quantum Yields from Chloride Treated CdTe Colloidal Quantum Dots.* Small, 2015. **11**(13): p. 1548-1554.

118. Yu, W.W., et al., *Experimental determination of the extinction coefficient of CdTe, CdSe, and CdS nanocrystals.* Chemistry of Materials, 2003. **15**(14): p. 2854-2860.

119. Monshi, A., M.R. Foroughi, and M.R. Monshi, *Modified Scherrer equation to estimate more accurately nano-crystallite size using XRD.* World Journal of Nano Science and Engineering, 2012. **2**(3): p. 154-160.

120. Hofer, F., et al. *Fundamentals of electron energy-loss spectroscopy*. in *IOP Conference Series: Materials Science and Engineering*. 2016. IOP Publishing.

121. Munetaka Ishiyama, Y.M., Masanobu Shiga, Kazumi Sasamoto *Water-soluble tetrazolium salt compounds*, 1996, Dojindo Laboratories Co., Ltd. : Japan.

122. Xiong, X.-B., H. Uludağ, and A. Lavasanifar, *Virus-mimetic polymeric micelles for targeted siRNA delivery.* Biomaterials, 2010. **31**(22): p. 5886-5893.

123. Bultmann, H., J. Teuton, and C.R. Brandt, *Addition of a C-terminal cysteine improves the anti-herpes simplex virus activity of a peptide containing the human immunodeficiency virus type 1 TAT protein transduction domain.* Antimicrob Agents Chemother, 2007. **51**(5): p. 1596-1607.

124. Sharei, A., et al., *Cell squeezing as a robust, microfluidic intracellular delivery platform.* Journal of visualized experiments: JoVE, 2013(81).

125. Wilson, T., *Confocal microscopy.* Academic Press: London, etc, 1990. **426**: p. 1-64.

126. Masters, B.R., *Handbook of biological confocal microscopy.* Journal of biomedical optics, 2008. **13**(2): p. 029902.

127.   Trasatti, S., *The absolute electrode potential: an explanatory note (Recommendations 1986).* Pure and Applied Chemistry, 1986. **58**(7): p. 955-966.

128.   Hunter, R.J., *Foundations of colloid science*. 2001: Oxford university press.

129.   Matijevic, E. and R.J. Good, *Surface and colloid science*. Vol. 12. 2012: Springer Science & Business Media.

130.   Smoluchowski, M., *Contribution à la théorie de l'endosmose électrique et de quelques phénomènes corrélatifs.* Pisma Mariana Smoluchowskiego, 1924. **1**(1): p. 403-420.

131.   Li, L., et al., *Highly luminescent CuInS2/ZnS core/shell nanocrystals: cadmium-free quantum dots for in vivo imaging.* Chemistry of Materials, 2009. **21**(12): p. 2422-2429.

132.   Kolny-Olesiak, J. and H. Weller, *Synthesis and application of colloidal CuInS2 semiconductor nanocrystals.* ACS applied materials & interfaces, 2013. **5**(23): p. 12221-12237.

133.   Aldakov, D., A. Lefrançois, and P. Reiss, *Ternary and quaternary metal chalcogenide nanocrystals: synthesis, properties and applications.* Journal of Materials Chemistry C, 2013. **1**(24): p. 3756-3776.

134.   Smith, A.M., M.C. Mancini, and S. Nie, *Bioimaging: second window for in vivo imaging.* Nature nanotechnology, 2009. **4**(11): p. 710.

135.   Bae, W.K., et al., *R/G/B/natural white light thin colloidal quantum dot-based light-emitting devices.* Adv Mater, 2014. **26**(37): p. 6387-93.

136.   Park, G.-C., et al., *Photovoltaic characteristics of CuInS2CdS solar cell by electron beam evaporation.* Solar Energy Materials and Solar Cells, 1997. **49**(1-4): p. 365-374.

137.   Omata, T., et al., *Electronic transition responsible for size-dependent photoluminescence of colloidal CuInS 2 quantum dots.* Journal of Materials Chemistry C, 2014. **2**(33): p. 6867-6872.

138.   Nam, D.-E., W.-S. Song, and H. Yang, *Noninjection, one-pot synthesis of Cu-deficient CuInS2/ZnS core/shell quantum dots and their fluorescent properties.* Journal of Colloid and Interface Science, 2011. **361**(2): p. 491-496.

139.   Ekimov, A., et al., *Spectra and decay kinetics of radiative recombination in CdS microcrystals.* Journal of Luminescence, 1990. **46**(2): p. 83-95.

140.   Goossens, A. and J. Hofhuis, *Spray-deposited CuInS2 solar cells.* Nanotechnology, 2008. **19**(42): p. 424018.

141.   Hofhuis, J., J. Schoonman, and A. Goossens, *Elucidation of the excited-state dynamics in CuInS2 thin films.* The Journal of Physical Chemistry C, 2008. **112**(38): p. 15052-15059.

142.   Castro, S.L., et al., *Synthesis and characterization of colloidal CuInS2 nanoparticles from a molecular single-source precursor.* The Journal of Physical Chemistry B, 2004. **108**(33): p. 12429-12435.

143.   Krustok, J., et al., *Origin of the deep center photoluminescence in CuGaSe 2 and CuInS 2 crystals.* Journal of Applied Physics, 1999. **86**(1): p. 364-369.

144.   Li, J., et al., *Origin of the doping bottleneck in semiconductor quantum dots: A first-principles study.* Physical Review B, 2008. **77**(11): p. 113304.

145.   Park, J. and S.-W. Kim, *CuInS 2/ZnS core/shell quantum dots by cation exchange and their blue-shifted photoluminescence.* Journal of Materials Chemistry, 2011. **21**(11): p. 3745-3750.

146.   Uehara, M., et al., *Synthesis of Cu In S 2 fluorescent nanocrystals and enhancement of fluorescence by controlling crystal defect.* The Journal of Chemical Physics, 2008. **129**(13): p. 134709.

147.   Chen, B., et al., *Highly Emissive and Color-Tunable CuInS2-Based Colloidal Semiconductor Nanocrystals: Off-Stoichiometry Effects and Improved*

Electroluminescence Performance. Advanced Functional Materials, 2012. **22**(10): p. 2081-2088.

148. Huang, D. and C. Persson, *Stability of the bandgap in Cu-poor CuInSe2.* Journal of Physics: Condensed Matter, 2012. **24**(45): p. 455503.

149. Massé, G., *Concerning lattice defects and defect levels in CuInSe2 and the I-III-VI2 compounds.* Journal of Applied Physics, 1990. **68**(5): p. 2206-2210.

150. Han, S., et al., *Synthesis of copper indium sulfide nanoparticles by solvothermal method.* Materials Letters, 2009. **63**(13-14): p. 1192-1194.

151. Sombuthawee, C., S. Bonsall, and F. Hummel, *Phase equilibria in the systems ZnS:MnS, ZnS:CuInS2, and MnS:CuInS2.* Journal of Solid State Chemistry, 1978. **25**(4): p. 391-399.

152. Schön, J. and E. Bucher, *Characterization of intrinsic defect levels in CuInS2.* physica status solidi (a), 1999. **171**(2): p. 511-519.

153. Nanu, M., et al., *Deep-level transient spectroscopy of TiO 2⁄ CuInS 2 heterojunctions.* Applied Physics Letters, 2005. **87**(24): p. 242103.

154. Zhang, S., et al., *Defect physics of the CuInSe 2 chalcopyrite semiconductor.* Physical Review B, 1998. **57**(16): p. 9642.

155. Hou, X. and K.-L. Choy, *Synthesis and characteristics of CuInS2 films for photovoltaic application.* Thin Solid Films, 2005. **480**: p. 13-18.

156. Binsma, J., L. Giling, and J. Bloem, *Luminescence of CuInS2: I. The broad band emission and its dependence on the defect chemistry.* Journal of Luminescence, 1982. **27**(1): p. 35-53.

157. Xu, Y. and M.A. Schoonen, *The absolute energy positions of conduction and valence bands of selected semiconducting minerals.* American Mineralogist, 2000. **85**(3-4): p. 543-556.

158. Mocatta, D., et al., *Heavily doped semiconductor nanocrystal quantum dots.* Science, 2011. **332**(6025): p. 77-81.

159. Zhu, H., et al., *Auger-assisted electron transfer from photoexcited semiconductor quantum dots.* Nano Lett, 2014. **14**(3): p. 1263-9.

160. Rabouw, F.T. and C. de Mello Donega, *Excited-State Dynamics in Colloidal Semiconductor Nanocrystals.* Top Curr Chem (Cham), 2016. **374**(5): p. 58.

161. Rawalekar, S., et al., *Surface-state-mediated charge-transfer dynamics in CdTe/CdSe core-shell quantum dots.* Chemphyschem, 2011. **12**(9): p. 1729-35.

162. Rawalekar, S., et al., *Ultrafast Charge Carrier Relaxation and Charge Transfer Dynamics of CdTe/CdS Core– Shell Quantum Dots as Studied by Femtosecond Transient Absorption Spectroscopy.* The Journal of Physical Chemistry C, 2009. **114**(3): p. 1460-1466.

163. Groeneveld, E., et al., *Size dependence of the exciton transitions in colloidal CdTe quantum dots.* The Journal of Physical Chemistry C, 2012. **116**(43): p. 23160-23167.

164. Masumoto, Y. and K. Sonobe, *Size-dependent energy levels of CdTe quantum dots.* Physical Review B, 1997. **56**(15): p. 9734.

165. Tyrrell, E. and J. Smith, *Effective mass modeling of excitons in type-II quantum dot heterostructures.* Physical Review B, 2011. **84**(16): p. 165328.

166. Borchert, H., et al., *Relations between the photoluminescence efficiency of CdTe nanocrystals and their surface properties revealed by synchrotron XPS.* Journal of Physical Chemistry B, 2003. **107**(36): p. 9662-9668.

167. Klimov, V.I., *Nanocrystal quantum dots*. 2010: CRC Press.

168. Mahler, B., et al., *Towards non-blinking colloidal quantum dots.* Nature materials, 2008. **7**(8): p. 659.

169. MacColl, A., *Reduction potentials of conjugated systems.* Nature, 1949. **163**: p. 178-179.

170. Méndez-Hernández, D.D., et al., *Simple and accurate correlation of experimental redox potentials and DFT-calculated HOMO/LUMO energies of polycyclic aromatic hydrocarbons.* Journal of molecular modeling, 2013. **19**(7): p. 2845-2848.

171. Kucur, E., et al., *Determination of quantum confinement in CdSe nanocrystals by cyclic voltammetry.* The Journal of Chemical Physics, 2003. **119**(4): p. 2333-2337.

172. Wang, L.W. and A. Zunger, *Pseudopotential calculations of nanoscale CdSe quantum dots.* Physical Review B, 1996. **53**(15): p. 9579-9582.

173. Sun, N., et al., *Potential Indexing of the Invasiveness of Breast Cancer Cells by Mitochondrial Redox Ratios*, in *Oxygen Transport to Tissue XXXVIII*. 2016, Springer. p. 121-127.

174. Nel, A., et al., *Toxic potential of materials at the nanolevel.* Science, 2006. **311**(5761): p. 622-627.

175. Yang, J., et al., *Evaluation of disulfide reduction during receptor-mediated endocytosis by using FRET imaging.* Proceedings of the National Academy of Sciences, 2006. **103**(37): p. 13872-13877.

176. Dembla, M., et al., *ArfGAP3 is a component of the photoreceptor synaptic ribbon complex and forms an NAD (H)-regulated, redox-sensitive complex with RIBEYE that is important for endocytosis.* Journal of Neuroscience, 2014. **34**(15): p. 5245-5260.

177. Luo, Z., et al., *Mesoporous Silica Nanoparticles End-Capped with Collagen: Redox-Responsive Nanoreservoirs for Targeted Drug Delivery.* Angewandte Chemie International Edition, 2011. **50**(3): p. 640-643.

178. Fonseca, S.B., M.P. Pereira, and S.O. Kelley, *Recent advances in the use of cell-penetrating peptides for medical and biological applications.* Advanced drug delivery reviews, 2009. **61**(11): p. 953-964.

179. Lindgren, M., et al., *Cell-penetrating peptides.* Trends in pharmacological sciences, 2000. **21**(3): p. 99-103.

180. Zorko, M. and Ü. Langel, *Cell-penetrating peptides: mechanism and kinetics of cargo delivery.* Advanced drug delivery reviews, 2005. **57**(4): p. 529-545.

181. de la Fuente, J.M. and C.C. Berry, *Tat peptide as an efficient molecule to translocate gold nanoparticles into the cell nucleus.* Bioconjugate Chemistry, 2005. **16**(5): p. 1176-1180.

182. Lewin, M., et al., *Tat peptide-derivatized magnetic nanoparticles allow in vivo tracking and recovery of progenitor cells.* Nature Biotechnology, 2000. **18**(4): p. 410.

183. Pan, L., et al., *Nuclear-targeted drug delivery of TAT peptide-conjugated monodisperse mesoporous silica nanoparticles.* Journal of the American Chemical Society, 2012. **134**(13): p. 5722-5725.

184. Frankel, A.D. and C.O. Pabo, *Cellular uptake of the tat protein from human immunodeficiency virus.* Cell, 1988. **55**(6): p. 1189-1193.

185. Cesbron, Y., et al., *TAT and HA2 facilitate cellular uptake of gold nanoparticles but do not lead to cytosolic localisation.* Plos One, 2015. **10**(4): p. e0121683.

186. Gulaboski, R., V. Markovski, and Z. Jihe, *Redox chemistry of coenzyme Q—a short overview of the voltammetric features.* Journal of Solid State Electrochemistry, 2016. **20**(12): p. 3229-3238.

187. Yamamoto, Y. and S. Yamashita, *Plasma ratio of ubiquinol and ubiquinone as a marker of oxidative stress.* Molecular aspects of medicine, 1997. **18**: p. 79-84.

188. Iversen, T.-G., T. Skotland, and K. Sandvig, *Endocytosis and intracellular transport of nanoparticles: present knowledge and need for future studies.* Nano Today, 2011. **6**(2): p. 176-185.

189. Oh, N. and J.-H. Park, *Endocytosis and exocytosis of nanoparticles in mammalian cells.* International journal of nanomedicine, 2014. **9**(Suppl 1): p. 51.

190. Verma, A. and F. Stellacci, *Effect of surface properties on nanoparticle–cell interactions.* Small, 2010. **6**(1): p. 12-21.
191. Vanysek, P., *Electrochemical series.* CRC handbook of chemistry and physics, 1998. **87**.
192. Smith, G.P. and V.A. Petrenko, *Phage display.* Chemical reviews, 1997. **97**(2): p. 391-410.
193. Winter, G., et al., *Making antibodies by phage display technology.* Annual review of immunology, 1994. **12**(1): p. 433-455.
194. Slocik, J.M., M.O. Stone, and R.R. Naik, *Synthesis of gold nanoparticles using multifunctional peptides.* Small, 2005. **1**(11): p. 1048-1052.
195. Nonoyama, T., et al., *Ordered nanopattern arrangement of gold nanoparticles on β-sheet peptide templates through nucleobase pairing.* Acs Nano, 2011. **5**(8): p. 6174-6183.
196. Whaley, S.R., et al., *Selection of peptides with semiconductor binding specificity for directed nanocrystal assembly.* Nature, 2000. **405**(6787): p. 665.
197. Rodriguez-Viejo, J., et al., *Cathodoluminescence and photoluminescence of highly luminescent CdSe/ZnS quantum dot composites.* Applied Physics Letters, 1997. **70**(16): p. 2132-2134.
198. Fukui, T., et al., *GaAs tetrahedral quantum dot structures fabricated using selective area metalorganic chemical vapor deposition.* Applied Physics Letters, 1991. **58**(18): p. 2018-2020.
199. Grundmann, M., et al., *Ultranarrow luminescence lines from single quantum dots.* Physical Review Letters, 1995. **74**(20): p. 4043.
200. Makarov, N.S., et al., *Spectral and dynamical properties of single excitons, biexcitons, and trions in cesium–lead-halide perovskite quantum dots.* Nano letters, 2016. **16**(4): p. 2349-2362.
201. de Mello Donega, C. and R. Koole, *Size dependence of the spontaneous emission rate and absorption cross section of CdSe and CdTe quantum dots.* The Journal of Physical Chemistry C, 2009. **113**(16): p. 6511-6520.
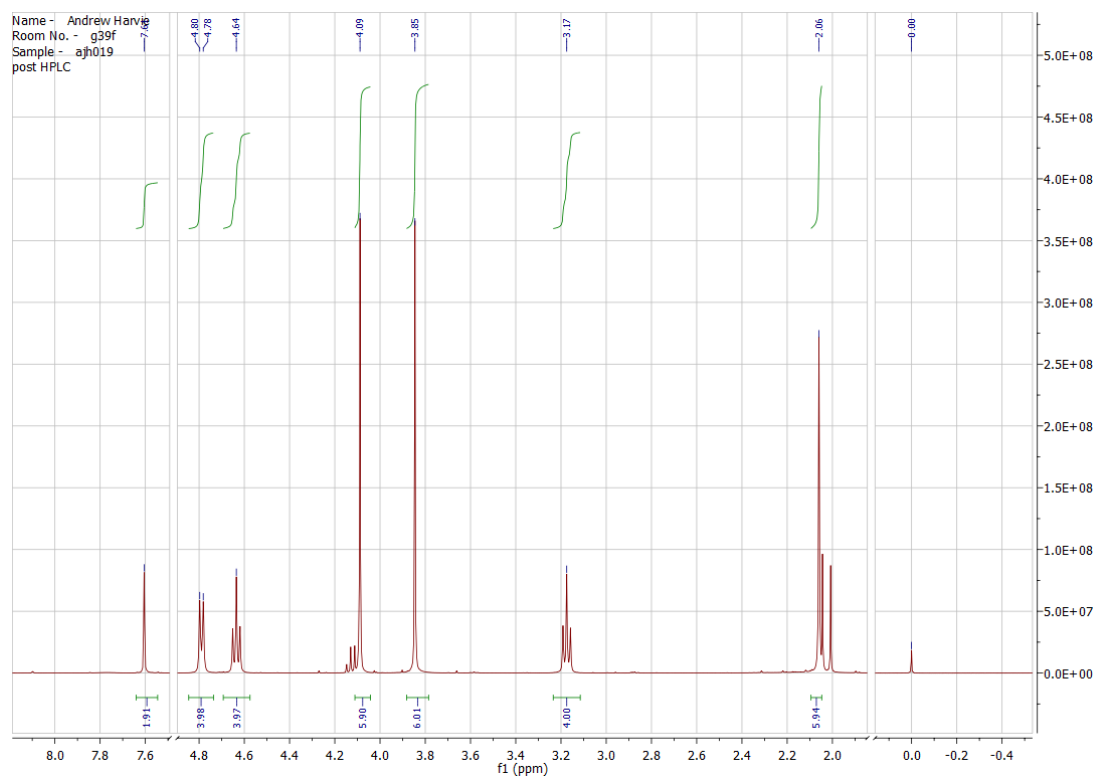
9   Appendix

9.1   NMR Spectra of Synthesised Compounds
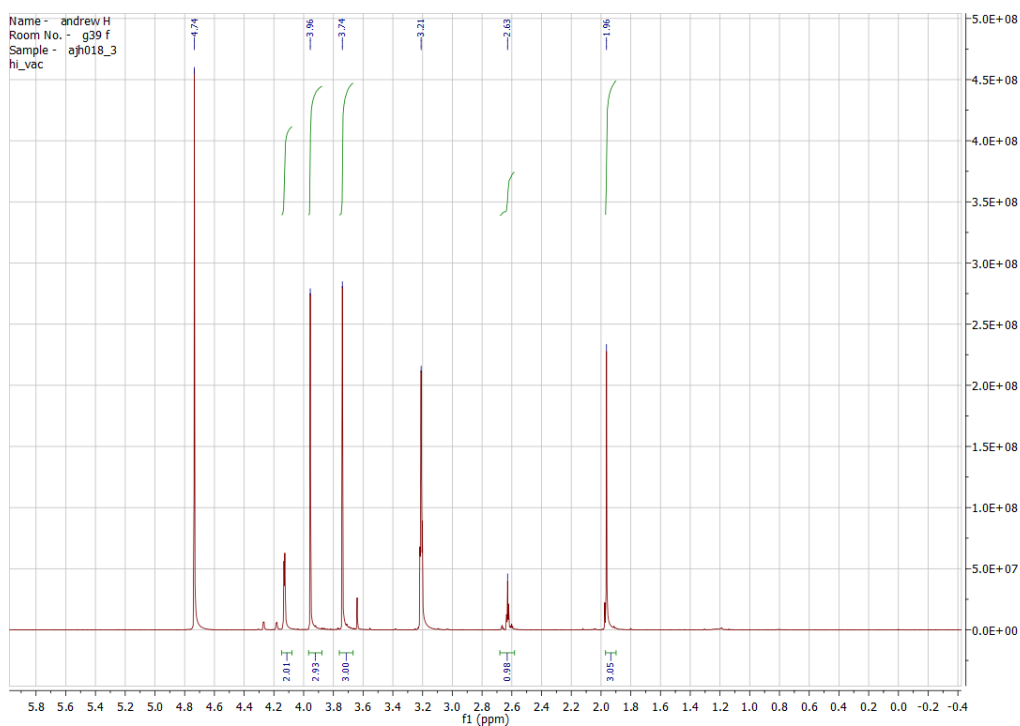
Proton NMR Spectrum of alkyne-terminated quinone 2,3-Dimethoxy-5-methyl-6-(2-propyn-1-ylamino)-2,5-cyclohexadiene-1,4-dione (400 MHz, MeOD)
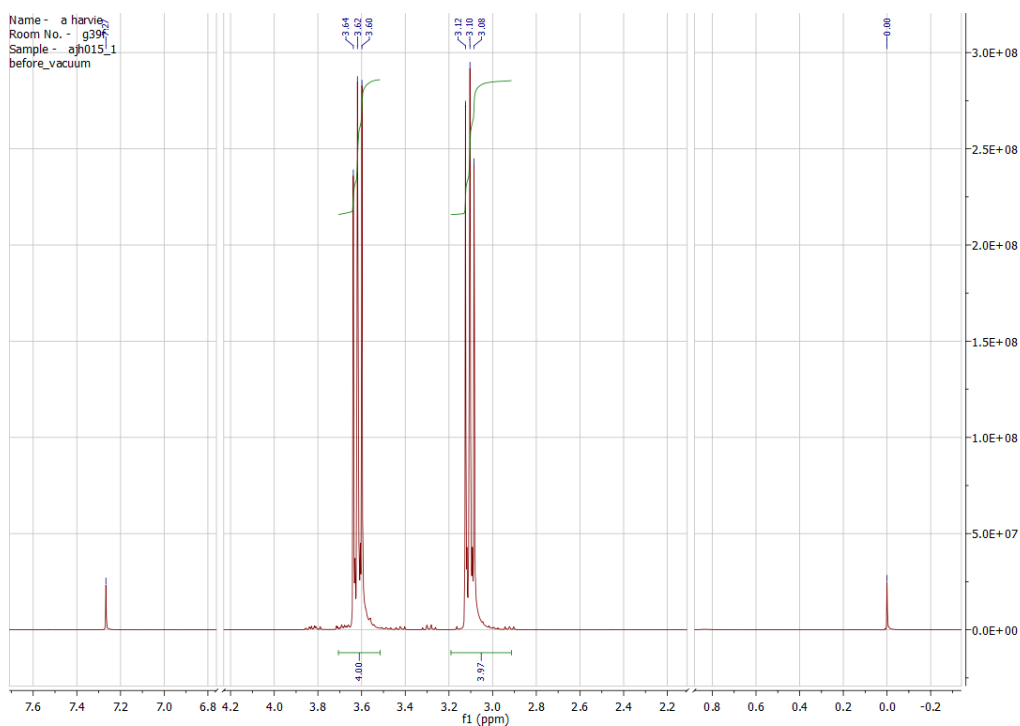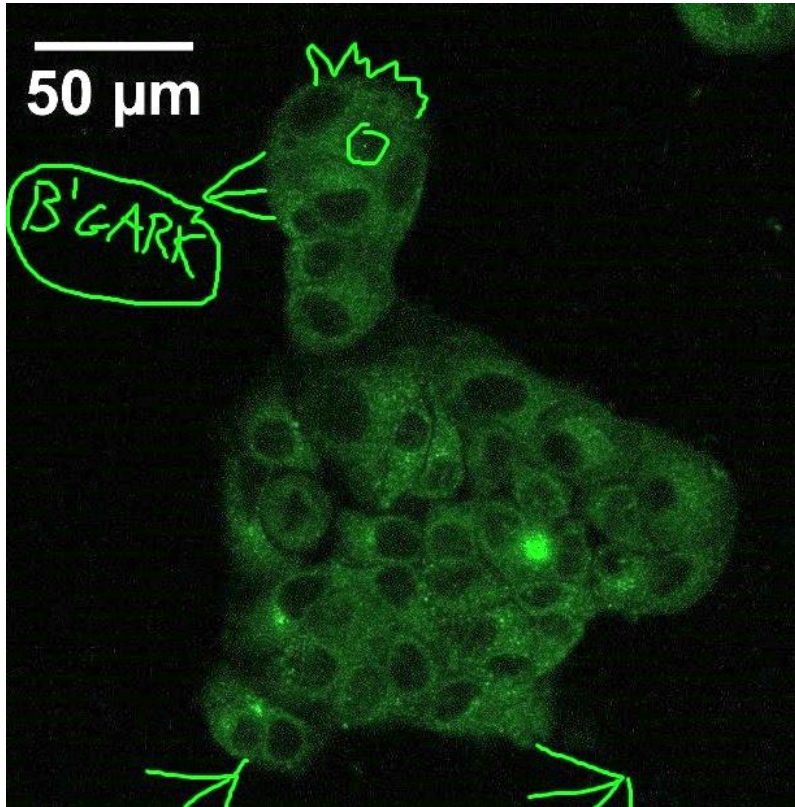

Proton NMR spectrum of bis-bromoethyl disulphide (400 MHz, CDCl$_3$)

Proton NMR spectrum of Q2NS (400 MHz, CDCl$_3$)

9.2   Biexciton Formation Probabilities for TA Experiments

The table shows calculated values of pump fluences per pulse (J), with average number of created excitons, $\langle N \rangle = \sigma J$, and biexciton formation probability, $P(N) = \langle N \rangle^N e^{-\langle N \rangle}/N!$,[200] where $N = 2$ for TA experiments for samples 40Q and 0Q. Biexciton formation probability is consistently less than 5×10^{-5} per QD, per pulse, which means Auger effects can be ignored. Values are calculated according to the model of de Mello Donega et al,[201] assuming a zinc blende CdTe QD of diameter 3.1 nm.

Sample	Pump Wavelength (nm)	J (photons/cm²*pulse)	Absorption cross section at pump wavelength (cm²)	number of excitons created per QD per excitation <N>	Biexciton formation probability P(2)
0Q Oxidised	420	$5.38\pm0.10\times10^{12}$	$1.02\pm0.02\times10^{-15}$	$5.48\pm0.15\times10^{-03}$	$1.49\pm0.08\times10^{-05}$
	450	$5.77\pm0.12\times10^{12}$	$7.48\pm0.15\times10^{-16}$	$8.63\pm0.24\times10^{-03}$	$3.69\pm0.20\times10^{-05}$
	480	$6.15\pm0.12\times10^{12}$	$6.75\pm0.14\times10^{-16}$	$8.30\pm0.23\times10^{-03}$	$3.41\pm0.20\times10^{-05}$
0Q Reduced	420	$5.38\pm0.11\times10^{12}$	$9.51\pm0.19\times10^{-16}$	$5.11\pm0.14\times10^{-03}$	$1.30\pm0.07\times10^{-05}$
	450	$5.77\pm0.12\times10^{12}$	$6.90\pm0.14\times10^{-16}$	$3.98\pm0.11\times10^{-03}$	$7.89\pm0.44\times10^{-06}$
	480	$6.15\pm0.12\times10^{12}$	$5.84\pm0.12\times10^{-16}$	$3.59\pm0.10\times10^{-03}$	$6.42\pm0.36\times10^{-06}$
40Q Oxidised	420	$5.38\pm0.11\times10^{12}$	$1.01\pm0.20\times10^{-15}$	$5.46\pm0.15\times10^{-03}$	$1.48\pm0.08\times10^{-05}$
	450	$5.77\pm0.12\times10^{12}$	$8.10\pm0.16\times10^{-16}$	$4.67\pm0.13\times10^{-03}$	$1.08\pm0.06\times10^{-05}$
	480	$6.15\pm0.12\times10^{12}$	$8.31\pm0.17\times10^{-16}$	$5.11\pm0.14\times10^{-03}$	$1.29\pm0.07\times10^{-05}$
40Q Reduced	420	$5.38\pm0.11\times10^{12}$	$9.44\pm0.19\times10^{-16}$	$5.08\pm0.14\times10^{-03}$	$1.28\pm0.07\times10^{-05}$
	450	$5.77\pm0.12\times10^{12}$	$6.66\pm0.13\times10^{-16}$	$3.85\pm0.11\times10^{-03}$	$7.36\pm0.40\times10^{-06}$
	480	$6.15\pm0.12\times10^{12}$	$6.01\pm0.12\times10^{-16}$	$3.70\pm0.10\times10^{-03}$	$6.81\pm0.40\times10^{-06}$

Chicken